Bifurcation Elimination in Rotor Gas Bearing Systems Applying Numerical Continuation with Embedded Design Optimization Scheme

by

Panagiotis V. Papafragkos

A Thesis submitted to the

National Technical University of Athens

School of Mechanical Engineering

Dept. of Mechanical Design and Automatic Control

for the Degree of

Dipl. Mechanical Engineer (MSc)

to be defended publicly on

Thesis committee: Assist. Prof. Athanasios Chasalevris NTUA, Supervisor

Prof. Ioannis Antoniadis NTUA

Prof. Vasilios Spitas NTUA

Athens, February 2022

CONTENTS

ABSTRACT

This thesis investigates the quality of bifurcations presented in a dynamic system consisting of a balanced or unbalanced elastic Jeffcott rotor mounted on gas-foil bearings, and assesses the stability of limit cycle motions for specific values of operating parameters and key design properties of the system, like rotor stiffness, foil stiffness and damping. The study aims to the design optimization of gas bearings in order to eliminate bifurcations, as they may compromise the operability of rotating systems, or increase noise level. This work applies the pseudo arc length continuation in combination with collocation method for the evaluation of limit cycles (periodic motions) as the bifurcation parameter changes (this being operating parameter or design property) of the non-autonomous system.

The energy flow among the components of the system is evaluated for various design sets of bump foil properties, rotor stiffness and unbalance magnitude. The project presents a methodology to retain the dissipating work at positive values during the periodic limit cycle motions caused by unbalance. An optimization technique is embedded in the pseudo arc length continuation of limit cycles, those evaluated (when exist) utilizing an orthogonal collocation method. The optimization scheme considers the bump foil stiffness and damping as the variables for which bifurcations do not appear in a certain speed range. It is found that secondary Hopf (Neimark-Sacker) bifurcations, which trigger large limit cycle motions, do not exist in the unbalanced rotors when bump foil properties follow the optimization pattern. Period doubling (flip) bifurcations are possible to occur, without driving the rotor in high response amplitude. Different design sets of rotor stiffness and unbalance magnitude are investigated for the efficiency of the method to eliminate bifurcations. Aiming to adjustable gas bearings as a future technology, the quality of the optimization pattern allows real time optimization, and in this way gas foil properties may shift values during operation, eliminating bifurcations and allowing operation in higher speed margins. The present study is considered as precursor for smart gas bearing applications under development.

ACKNOWLEDGEMENTS

Throughout my Master Thesis, I have received a great deal of support and assistance. I was very lucky because I worked with a great team, which did this Master Thesis a pleasant experience for me and helped me achieve my goals.

For this reason, I would like to express my special appreciation and gratitude to my thesis supervisor, Prof. Athanasios Chasalevris, for the guidance, the support, and the trust that he showed me, which have been my motivation for my continuous effort and improvement. He gave me the opportunity to work at a higher level and his door office was always open whenever I ran into a trouble spot or had a question about my research. This thesis would never been so great without his contribution.

I am also grateful to my colleagues, Ioannis Gavalas and Ioannis Raptopoulos. Their research work helped me a lot, so I would like to thank them too. Morever, I feel obligated to thank Prof. Antoniadis and Prof. Spitas for participating in the evaluation of this thesis.

Getting through my Master Thesis required more than academic support. None of these would happen without the support of my family. Their unfailing support and continuous encouragement throughout these years of study gave me courage to continue pursuing my dreams. So, I would like to express my appreciation, my love and gratitude to them because this accomplishment would not have been possible without them.

Last but not least, I would like to thank my friends. They stood by me and supported me when I was having a hard time. They offered their encouragement through phone calls and meetings and, of course, made this journey more joyable with all the good experiences that we shared together.

Panagiotis V. Papafragkos

Athens, February 2022

NOMENCLATURE AND ABBREVIATIONS

Hellenic letters

$\bar{\alpha}_f$: dimensionless compliance of the bump foil per area, $\bar{\alpha}_f = 2p_0\left(l_0/t_b\right)^3\left(1-\nu^2\right)s_0/\left(c_r E\right)$

$a, \bar{a}$: dimensioned and dimensionless angular acceleration $\bar{a} = 36\mu^2 R^4 a/\left(p_0{}^2 c_r{}^4\right)$

η : loss factor in the bump foil structure

μ : dynamic viscosity of gas

ν : Poisson's ratio of the bump foil material

τ : dimensionless time $\tau = p_0 c_r{}^2 t/\left(6\mu R^2\right)$

φ_r : journal's angle of rotation

φ_0 : angle of foil fixation point

$\Omega, \bar{\Omega}$: angular velocity of the rotor, dimensionless $\bar{\Omega} = 6\mu R^2\Omega/\left(p_0 c_r^2\right)$

Latin Letters

c_r : bearing clearance

D : bearing diameter $D = 2R$

e_u, ε : absolute and relative unbalance eccentricity $\varepsilon = e_u/c_r$

E : Young's modulus of the bump foil material

$F_{B,X}, F_{B,Y}$: resulting gas forces in x and y directions

$F_{U,X}, F_{U,Y}$: unbalance force components in x and y directions

$h, \bar{h}$: absolute and relative gas film thickness $\bar{h} = h/c_r$

$k_f, \bar{k}_f$: foil stiffness coefficient per area. $k_f = p_0/\left(\bar{\alpha}_f c_r\right)\left[N/m^3\right]$, $\bar{k}_f = 1/\bar{\alpha}_f$

$k_s, \bar{k}_s$: absolute and relative shaft lateral stiffness $k_s = \bar{k}_s m_d p_0{}^2 c_r{}^4/\left(36\mu^2 R^4\right)$

L : length of the bearing

L_s : length of the rotor (bearing span)

l_0 : bump half-length

m_j : journal mass

m_d : disc mass

p_0 : ambient pressure

$p, \bar{p}$: absolute and relative gas pressure $\bar{p} = p/p_0$

$q, \bar{q}$: absolute and relative foil deflection, $\bar{q} = q/c_r$

R_s : radius of the rotor

t_b : bump foil thickness

W_{cf} : work produced by the foil damping forces

W_f : work produced by the forces acting from the gas to the top foil

W_g : work produced by the gas forces $F_{B,X}$ and $F_{B,Y}$

W_{kf} : work produced by the foil spring forces

$x_j, y_j, \bar{x}_j, \bar{y}_j$: absolute and relative journal displacement in x and y direction, $\bar{x}_j = x_j/c_r, \bar{y}_j = y_j/c_r$

$x_d, y_d, \bar{x}_d, \bar{y}_d$: absolute and relative disc displacement in x and y direction, $\bar{x}_d = x_d/c_r, \bar{y}_d = y_d/c_r$

$x, \bar{x}$: absolute and relative spatial coordinate in x direction, $\bar{x} = x/R$

$z, \bar{z}$: spatial coordinate in z direction, $\bar{z} = z/L$

Abbreviations:

AI:	Artificial Intelligence	FFT:	Fast Fourier Transform	ODE:	Ordinary Diff. Equation
AH:	Andronov-Hopf bifurcation	GFB:	Gas Foil Bearing	PD:	Period Doubling bif.
DoF:	Degree of Freedom	LPC:	Limit Point of Cycles	SN:	Saddle Node bifurcation
FDM:	Finite Difference Method	NS:	Neimark-Sacker bif.	STFT:	Short Time Fourier Tr.

1. INTRODUCTION

1.1. Gas Foil Bearings Development

Gas foil bearings (GFBs) are an upcoming and promising oil-free technology in modern high-speed rotating machinery [1]. Relying on a thin gas film building up an aerodynamic, load-carrying lubrication wedge, such bearings are self-acting and do not require any external pressurization. Most notably, due to the absence of solid-to-solid contact between the airborne rotor journal and the bearing sleeve, excessively low wear and power loss can be achieved [2].

During the last few decades, the potential of GFBs has been widely confirmed by a great number of successful applications in air cycle machines of commercial aircraft [3]. Lately, in particular as a result of insurmountable speed, temperature, and weight limitations of conventional rolling-element bearings, novel concepts of oil-free turbochargers [4] and oil-free rotorcraft propulsion engines [5] are gaining more and more interest.

Foil air bearings are similar to conventional oil-lubricated bearings in size, shape, and in that the fluid film pressure is developed via the hydrodynamic effect. Unlike conventional bearings, foil air bearings use air as their working fluid and the bearing surface is compliant rather than rigid [6]. This compliant inner or top foil surface is supported by a spring pack or bump foil layer which allows the bearing to accommodate shaft misalignment, thermal and centrifugal distortion, the presence of wear debris and also allows the designer to tailor the operational foil shape to enhance film pressure and hence bearing load capacity [7].

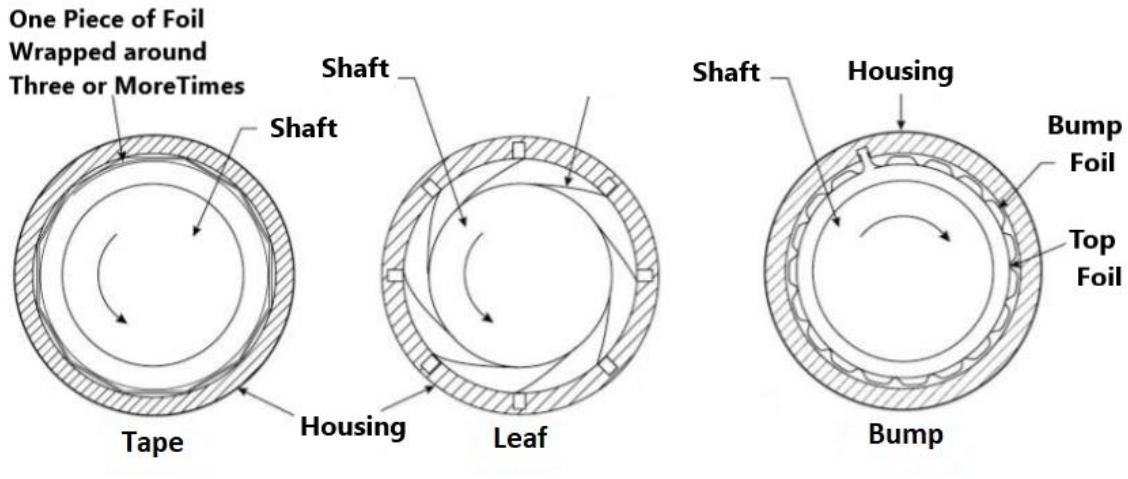

Fig. 1.1.1: Schematic example of typical Generation I foil bearings with axially and circumferentially uniform elastic support elements: a) tape-type foil bearings b) leaf-type foil bearing and c) bump-type foil bearing [8]

[1] T. Leister, C. Baum, W. Seemann (2017) On the Importance of Frictional Energy Dissipation in the Prevention of Undesirable Self-Excited Vibrations in Gas Foil Bearing Rotor Systems. TECHNISCHE MECHANIK, 37, 2-5, (2017), 280 – 290

[2] Heshmat, H.; Walowit, J. A.; Pinkus, O. (1983) Analysis of gas-lubricated foil journal bearings. Journal of Lubrication Technology, 105, 4, 647–655.

[3] Howard, S. A.; Bruckner, R. J.; DellaCorte, C.; Radil, K. C. (2007) Gas foil bearing technology advancements for closed Brayton cycle turbines. Tech. Rep. NASA TM-214470, National Aeronautics and Space Administration, United States of America.

[4] Howard, S. A. (1999) Rotordynamics and design methods of an oil-free turbocharger. Tech. Rep. NASA CR-208689, National Aeronautics and Space Administration, United States of America.

[5] Howard, S. A.; Bruckner, R. J.; Radil, K. C. (2010) Advancements toward oil-free rotorcraft propulsion. Tech. Rep. NASA TM-216094, National Aeronautics and Space Administration, United States of America.

[6] DellaCorte C., Zaldana, A., and Radil, K. (2004) A Systems Approach to the Solid Lubrication of Foil Air Bearings for Oil-Free Turbomachinery. STLE/ASME Joint International Tribology Conference, FL Oct. 2003

[7] Gross, W. A. (1962) Gas Film Lubrication, John Wiley and Sons, Inc.

[8] H. Ming Chen, Roy Howarth, Bernard Geren, Jay C. Theilacker, William M. Soyars, (2001), "Application of foil bearings to helium turbocompressor", Proceedings of the 30th turbomachinery symposioum.

Fig. 1.1.1 schematically shows some gas foil bearing designs. In multiple overleaf and tape GFBs, the compliance to bending from staggered structural foils and the dry-friction at the contact lines define their operational characteristics [9]. In corrugated bump GFBs, bump-strip layers supporting a top foil render a tunable bearing stiffness with nonlinear elastic deformation characteristics. In this type of bearing, dry-friction effects arising between the bumps and top foil and the bumps and the bearing inner surface provide the energy dissipation or damping characteristics [10,11].

Since foil bearings do not use oil as their working fluid they can and are routinely used over an extremely wide temperature range, from cryogenic to over 650°C, not possible with oil lubrication. Foil air bearings, however, do require solid lubrication to prevent wear and reduce friction at very low speeds encountered during start-up and shut-down prior to the development of the hydrodynamic gas film and also during momentary bearing overloads such as high speed rubs [12]. Traditionally, this solid lubrication is provided by applying a thin polymer film or coating to the foil surface, see Fig. 1.1.2.

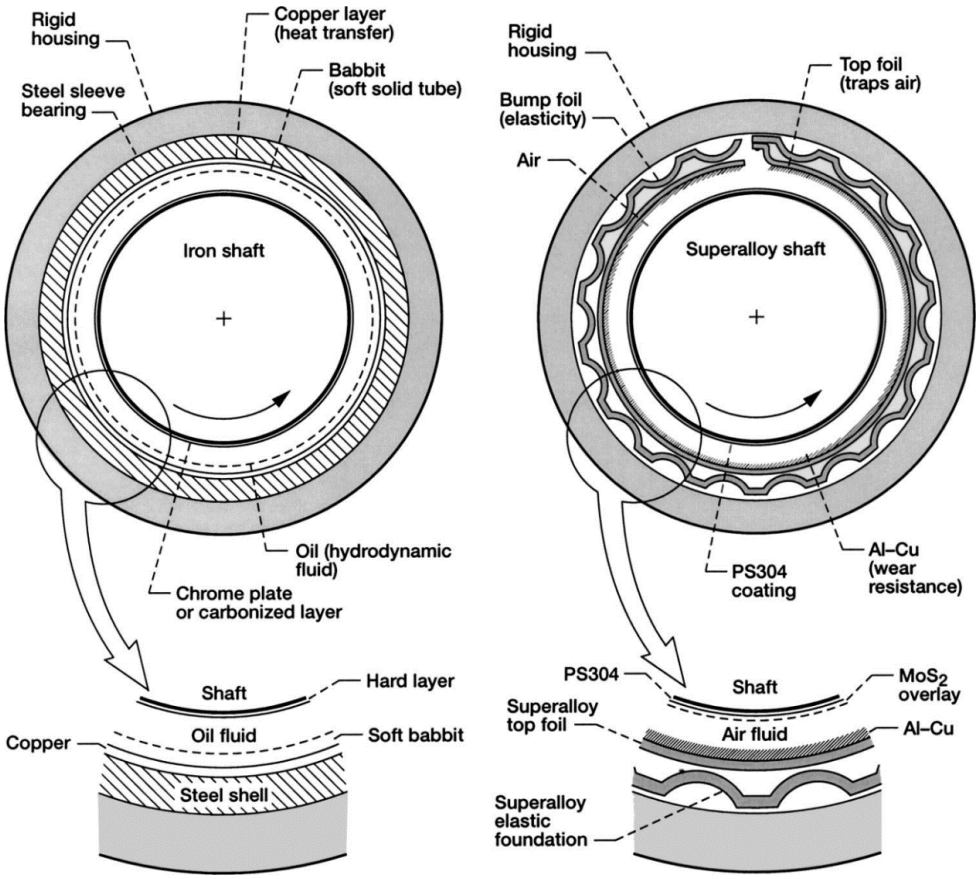

Fig. 1.1.2: Schematic representation of systems approach to bearing lubrication a) conventional oil lubricated bearing, and b) multilevel solid/gas lubricated foil air bearing [6]

[9] Heshmat, C. A., Heshmat, H., (1995), "An Analysis of Gas-Lubricated, Multileaf Foil Journal Bearings with Backing Springs," J. Tribol., 117, pp. 437-443.

[10] Braun, M. J., Choy, F. K., Dzodzo, M., and Hsu, J., (1996), "Two-Dimensional Dynamic Simulation of a Continuous Foil Bearing", Tribol. Intl., 29(1), pp. 61-68.

[11] Heshmat, H., Shapiro, W., and Gray,S., (1982), "Development of Foil Journal Bearings for High Load Capacity and High Speed Whirl Stability", ASME J. Lubr. Technol., 104, pp. 149–156.

[12] DellaCorte, C., and Wood, J. C. (1994), "High Temperature Solid Lubricant Materials for Heavy Duty and Advanced Heat Engines", NASA TM-106570.

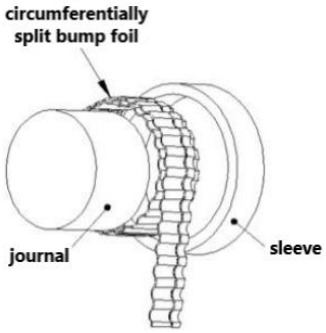

Fig 1.1.3 Generation II foil air bearing. [17]

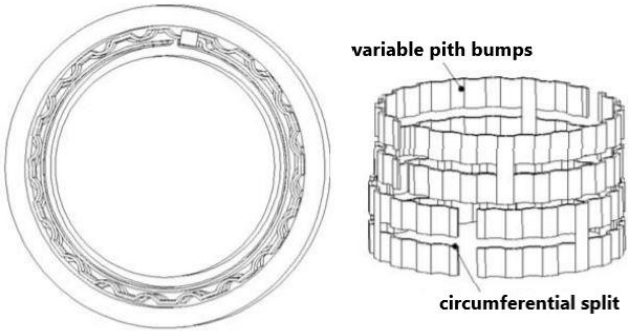

Fig 1.1.4 Generation III foil air bearing [17]

Blok and Van Rossum published the first paper on foil bearings in 1953 [13]. Although they coined the term ‘‘foil bearing’’, their work actually concerned an oil lubricated shaft running against an acetate film or ‘‘foil’’. The concept of a flexible bearing surface and its implications to and potential for improved capabilities was quickly adapted by other technologists and papers on air lubricated foil bearings began to appear in the open literature in the following decade [14,15]. Foil bearing load capacity is expressed in relation to a bearing's load capacity coefficient, D. This coefficient, defined fully in [16], is an empirically established performance parameter which relates bearing size and speed to the load that a bearing can support. Mathematically, it is defined as follows [6, 17]:

$$W = D \times (L \times d) \times (d \times \text{krpm})$$

where,

W is the maximum steady load that can be supported, N
D is the bearing load capacity coefficient, $N / mm^3 \cdot krpm$
L is the bearing axial length, mm
d is the shaft diameter, mm
$krpm$ is the shaft rotational speed in thousands of revolutions per minute.

These first generation designs are characterized by having a uniform simple elastic foundation with uniform stiffness properties. Generation I foil bearings, see Fig. 1.1.1c, exhibit load capacities approximately equal to rigid gas bearings of similar size and they used in air cycle machines. Second generation foil bearings, see Fig. 1.1.3, have a more complex elastic foundation in which the stiffness is tailored in one direction, for example axially, to accommodate some environmental phenomena such as shaft misalignment or leakage of hydrodynamic fluid from the foil edges. These Generation II foil bearings exhibit load capacities approximately twice that of Generation I bearings and they have been used successfully in turbocompressors and small microturbines. Third Generation bearings, see Fig. 1.1.4, with very complex elastic foundations, have stiffness that is tailored in two directions, often axial and radial. This level of design flexibility enables accommodation of edge effects and the ability to optimize bearing stiffness for

[13] Blok H., and van Rossum J. J., (1953) “The Foil Bearing-A New Departure in Hydrodynamic Lubrication”, ASLE J. Lubr. Eng., 9, pp. 316–330.

[14] Ma, J. T. S., 1965, ‘‘An Investigation of Self-Acting Foil Bearings,’’ASME J. Basic Eng., 87, pp. 837–846.

[15] Barnett, M. A., and Silver, A. (1970) ‘‘Application of Air Bearings to High Speed Turbomachinery’’, SAE Paper 700720.

[16] DellaCorte, C., and Valco, M. J. (2000) “Load Capacity Estimation of Foil Air Journal Bearings for Oil-Free Turbomachinery Applications”, STLE Tribol. Trans., 43, pp. 795–801.

[17] Krzysztof Nalepa, Paweł Pietkiewicz , Grzegorz Żywica, (2009),“Development of the foil bearing Technology”, Technical Siences, Abbrev.: Techn. Sc., No 12, Y 2009

varying loads. Generation III foil bearings have been shown to have load capacities three to four times greater than primitive Generation I bearings and they will be used in aircraft engine applications, see Fig 1.1.5. [18]

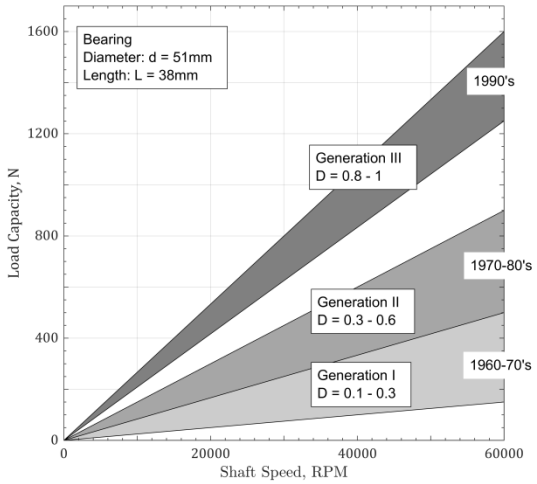

Fig. 1.1.5: Bearing Load Capacity, Gen. I, II, III [11]

Foil bearings have been successfully used in high-speed turbomachines, and they present a remarkable reliability. For aircraft turbo-compressors, the mean-time-between failure is typically over 60000 h [19,20]. The operational mechanism of foil bearings is similar to that of fluid-film bearings. At the start-up stage, the rotor journal and the bearing bore are contacting each other directly. Once the rotational speed crosses the lift off speed, the rotor will be suspended by the generated pressure fluid film. As the stiffness of the foils is much smaller than that of the fluid film, the foil bearings can adapt to various working conditions through foil deformations. Specially, the range between the second and third critical speeds of the foil bearing-rotor system is very large, which means that the foil bearings can suspend the rotor at a very high speed stably. Owing to these advantages, foil bearings are identified as a potential alternative for REBs. If properly designed and operated, foil bearings would incur very slight wear and have a long service life [21].

1.2. Gas Foil Bearings and Rotor Dynamics

The bump type foil bearing is simple in construction and more efficient compared to the other types of foil bearing. It is superior to conventional gas bearing and has higher load capacity, lower power loss, good stability, and endurance to high temperature, misalignment and foreign particles in the gas [2]. Because of these good dynamic characteristics, an important amount of research work on bump type foil bearing dynamics has been carried out in the past three. First, Heshmat et al. [2] developed a so-called simple elastic foundation model for foil journal bearing and compliant thrust bearing, in which the bump foil was built as separated springs. The structural stiffness was assumed to be linear, equally distributed and independent of loads. And the static

[18] Christopher DellaCorte, Kevin C. Radil, Robert J. Bruckner, S. Adam Howard, (2007), "Design, Fabrication and Performance of Open Source Generation I and II Compliant Hydrodynamic Gas Foil Bearings", NASA/TM—2007-214691

[19] Y. Hou, Z. H Zhu, C. Z. Chen (2004) Comparative test on two kinds of new compliant foil bearing for small cryogenic turbo-expander. *Cryogenics*, 44: 69-72.

[20] Z. Y. Guo, K. Feng, T. Y. Liu (2018) et al. Nonlinear dynamic analysis of rigid rotor supported by gas foil bearings: effects of gas film and foil structure on subsynchronous vibration. Mechanical Systems and Signal Processing, 107: 549-566.

[21] H Heshmat H. (1991) A feasibility study on the use of foil bearings in cryogenic turbopumps. 27th AIAA/SAE/ASME/ASEE Joint Conference, California, USA, June 24-26: AIAA-91-2103.

Reynolds equation was solved to obtain the pressure distribution. This model has been widely adopted in many other works due to simplicity, but it predicts low structural stiffness because the interactions between the bumps are neglected. Later, Ku and Heshmat [22] presented a more elaborate structural deflection model, which incorporated the interaction forces between bumps, Coulomb friction at the contact surfaces and geometric parameters of the foils, using shell theory to calculate the stiffness of an entire bump strip. In addition, synchronous stiffness and damping coefficients of the foil structure were predicted. Peng and Carpino [23,24] presented linear stiffness and damping coefficients of bump foil bearing considering elastic effect of bump foil and foil bearing dynamic coefficients using finite element method. Iordanoff [25] proposed another formulation for the static stiffness of the bump considering the friction at contact surfaces, and the local bump compliance of the welded and free bumps were calculated separately using different boundary conditions.

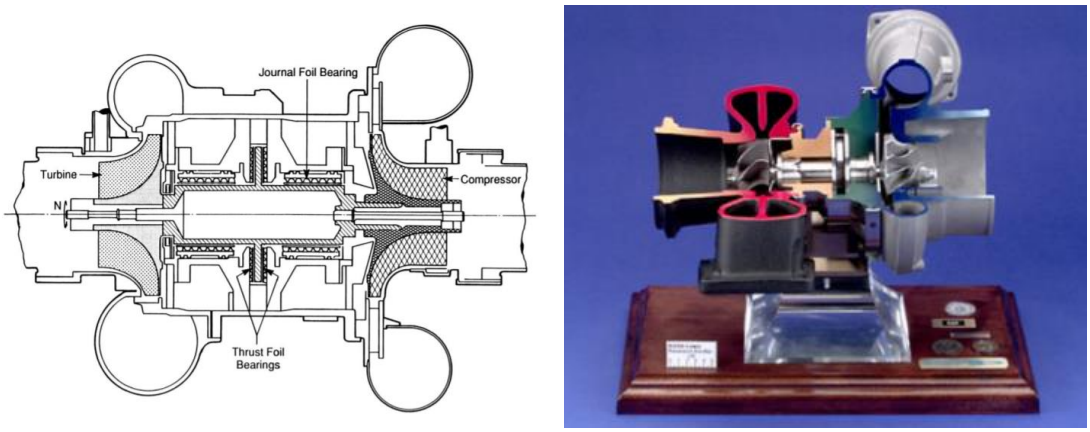

Fig. 1.2.1: Application of Compliant GFBs in Aircraft Air-Cycle Machines [26]

FSan Andres and Kim [27] developed a numerical model in which both 1D and 2D finite element (FE) structural models were introduced to calculate the local deflection of the top foil. They also obtained bearing characteristics for heavily loaded foil bearing and validated with test results and they presented frequency dependent dynamic coefficients [28]. Moreover, they presented nonlinear response of rotor supported by gas foil bearing. The nonlinear nature of stiffness characteristics of foil bearing is modelled using experimental data. They have shown that the linear force coefficients are not reliable to represent the dynamic behavior of rotor supported on gas foil bearing [29]. Kim [30] conducted a parametric study on the static and dynamic characteristics of bump type foil bearings with different top foil geometries (circular and three

[22] C. P. Ku, H. Heshmat (1992) Compliant foil bearing structural stiffness analysis: part1-theoretical model including strip and variable bump foil geometry, Journal of Tribology 114 (2): 394–400.

[23] Peng, J.-P.; Carpino, M. (1993) Calculation of stiffness and damping coefficients for elastically supported gas foil bearings. Journal of Tribology, 115, 1, 20–27.

[24] J. P. Peng, M. Carpino (1997) Finite element approach to the prediction of foil bearing rotor dynamic coefficients, Journal of Tribology 119 (1): 85–90.

[25] I. Iordanoff (1997) Analysis of an aerodynamic compliant foil thrust bearing: method for a rapid design. Journal of Tribology 121 (4) 1996 816-822

[26] H. Heshmat., P. Hermel, (1993), Compliant Foil Bearings Technology and Their Application to HighSpeed Turbomachinery, Journal of Tribology 25: 559-575

[27] L. San Andres, T. H. Kim (2007), Improvements to the analysis of gas foil bearings: Integration of top foil 1D and 2D structural models. In: ASME turbo expo 2007: Power for land, sea, and air, pp. 779789. New York: ASME.

[28] T. H. Kim, L. San Andres (2008), Heavily loaded gas foil bearings: a model anchored to test data, Journal Engineering for Gas Turbines and Power 130 (1) 012504–012508.

[29] L. San Andres, T. H. Kim (2008), Forced nonlinear response of gas foil bearing supported rotors, Tribol. Intern. 41 704–715.

[30] D. Kim (2007) Parametric studies on static and dynamic performance of air foil bearings with different top foil geometries and bump stiffness distributions, Journal of Tribology 129 (2) 354–364.

pad configurations) and bump stiffness distributions. He presented a mathematical model of the bump foil bearing with equivalent viscous damping. The comparison of the static and dynamic performance of the bearing with linear perturbation based dynamic coefficients and a time domain orbit simulation is carried out. He found that there is a significant difference in the estimated onset speeds of instability from the set of approaches.

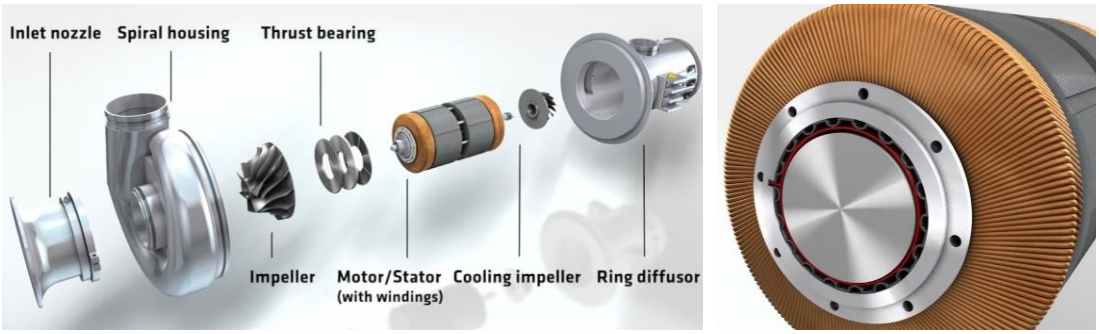

Fig. 1.2.2: Construction of a Turbo Blower using GFBs; taken from AERZEN

Le Lez et al. [31] developed a new structural model for bump-type foil bearings using an analytical method considering the interaction between bumps. The elasticity of the bump and friction forces was also considered. They have also studied the nonlinear behavior of the foil bearing with stability and unbalance responses [32]. Carpino and Talmage [33,34] presented a fully coupled FE formulation considering the membrane and bending effects of the top foil, bump foil deflections and Coulomb friction between contact surfaces. Lee et al. [35] presented a FE model for the foil structure with consideration of the hysteretic behavior of friction. Unlike the previous models that assumed the direction of friction to be opposed to the horizontal displacement, this model related the direction of friction to the path of displacement. Various deflections of the foil structure are obtained for the same load in different loading/unloading cases. The effect of friction and the energy dissipation properties were investigated. Feng and Kaneko [36] proposed a link-spring model for the bump foil and the top foil was treated as a shell. Each bump was simplified to two rigid links and a horizontal spring. These two links are connected by a joint at the summit and by the spring at the bottom. The stiffness of bump foil, interactions between bumps, friction and deflection of top foil were taken into account. Significant work has been conducted in solving the compressible Reynolds equation numerically. Lez et al. [37], as well as Kim [38] and Zhang et al. [39], used the Finite Difference Method (FDM) to substitute the time derivatives dp/dt and dh/dt included in Reynolds equation by backward-difference

[31] S. Le Lez, M. Arghir, J. Frene (2007) A new bump-type foil bearing structure analytical model, Journal of Engineering for Gas Turbines and Power 129 (4) 1047–1057.

[32] S. Le Lez, M. Arghir, J. Frene (2009) Nonlinear numerical prediction of gas foil bearing stability and unbalanced response, Journal of Engineering for Gas Turbines and Power 131:012503–012512.

[33] Carpino M. and Talmage G. (2006), "Prediction of rotor dynamic coefficients in gas lubricated foil journal bearings with corrugated sub-foils", Tribol. Trans, 49: 400–409.

[34] Carpino M. and Talmage G. (2003), "A fully coupled finite element formulation for elastically supported foil journal bearings", Tribol Trans, 46: 560–565.

[35] Lee Y-B, Park D-J, Kim C-H, et al. Operating characteristics of the bump foil journal bearings with top foil bending phenomenon and correlation among bump foils. Tribol Int 2008; 41: 221–233

[36] K. Feng, S. Kaneko (2010) Analytical model of bump-type foil bearings using a link spring structure and a finite element shell model, Journal of Tribology 132 (2) 1–11.

[37] S. LeLez, M. Arghir, J. Frêne (2009) Nonlinear numerical prediction of gas foil bearing stability and unbalanced response, Journal of Engineering for Gas Turbines and Power 131:012503.

[38] D. Kim (2007) Parametric studies on static and dynamic performance of air foil bearings with different top foil geometries and bump stiffness distributions, Journal of Tribology 129: 354–364.

[39] J. Zhang, W. Kang, Y. Liu (2009) Numerical method and bifurcation analysis of Jeffcott rotor system supported in gas journal bearings, Journal of Computational and Nonlinear Dynamics 4 011007.

approximations. Later, Bonello and Pham [40,41], and Larsen and Santos [42] introduced a state variable $\psi = p \cdot h$ in order to solve the Reynolds equation and simultaneously acquire results for other state variables, at the same time step. In parallel, FDM and Galerkin reduction method were used in order to perform the spatial discretization. Baum et al. [43] presented a slightly different approach by using the FDM method and Galerkin reduction method without inserting the state variable ψ. Instead, they used backward-differences approximations for the spatial differentiation of the pressure and fluid film variables and solved the Reynolds equation for the time derivative dp/dt.

Nevertheless, it is far from enough to just perform the linear analysis of GFB-rotor systems. Due to the nonlinear hydrodynamic film, experiments and simulations of the rotors supported on the bump-type GFBs show significant subsynchronous vibrations and frequency-locking behaviors [44,44,45]. Similar subsynchronous vibration phenomena were also widely observed in rotor systems supported by other types of gas bearings [46,47]. The first study to attempt to explain the nonlinear vibrations was presented by San Andrés and Kim [28] using a reduced numerical model that neglected the gas film under the assumption of a very stiff gas film. They suggested the cause of the subsynchronous vibrations as a forced nonlinearity under high unbalanced levels rather than typical hydrodynamic bearing instability. Inspired by the work of Andrés and Kim [28], Hoffmann et al. [43] investigated the effect of the nonlinear fluid film forces on the subsynchronous vibrations and found that the system may be self-excited by the gas film forces with a frequency related to the system's natural frequency. Their results also indicated that the speed range of the subsynchronous vibrations, which characterize stable Hopf bifurcation behavior, decreases and finally disappears with the increase in the static load. A coincident conclusion could be drawn from the simulation results of Gu et al. [45] in which no subsynchronous vibrations existed before the film failure. A more systematic investigation was conducted by Hoffmann and Liebich [46] experimentally and numerically. The two causes of subsynchronous vibrations were studied individually, and one of the findings was that a higher unbalanced value would result in a lower onset speed of subsynchronous vibrations.

Except for the subsynchronous vibrations, another noteworthy nonlinear topic is the existence of stable and unstable periodic solutions. On the one hand, Pham and Bonello [40] noticed that there was no stable limit cycle in a GFB-rotor system with the most commonly used parameters, while a stable limit cycle was obtained with a very stiff foil structure and a small bearing clearance. Bonello and Pham [39] gave a specific explanation that attributed this to the compliance of the foil structure, in view of the fact that limit cycles have been numerically obtained in rotors supported by rigid gas bearings in [47,48]. On the other hand, an unstable limit cycle was found

[40] P. Bonello, H. M. Pham (2014) The efficient computation of the nonlinear dynamic response of a foil–air bearing rotor system, Journal of Sound and Vibration 333:3459–3478.

[41] H. M. Pham, P. Bonello (2013) Efficient techniques for the computation of the nonlinear dynamics of a foil–air bearing rotor system, ASME TurboExpo2013: Turbine Technical Conference and Exposition, p.7.

[42] J. S. Larsen, I. F. Santos (2014) Efficient solution of the non-linear Reynolds equation for compressible fluid using the finite element method, Journal of the Brazilian Society of Mechanical Sciences and Engineering 1–13.

[43] Baum C., Hetzler H., Schröders S., Leister T., Seemann W. (2020) A computationally efficient nonlinear foil air bearing model for fully coupled, transient rotor dynamic investigations. Tribol. Int. doi: https://doi.org/10.1016/j.triboint.2020.106434

[44] Heshmat, H (1994).: Advancements in the performance of aerodynamic foil journal bearings: High speed and load capability. J. Tribol. 116(2), 287–294

[45] Gu, Y., Ma, Y., Ren, G.: Stability and vibration characteristics of a rotor-gas foil bearings system with high static low dynamic stiffness supports. J. Sound Vib. 397, 152–170 (2017)

[46] Hoffmann, R., Pronobis, T., Liebich, R.: Non-linear stability analysis of a modified gas foil bearing structure, In: Proceedings of the 9th IFToMM International Conference on Rotor Dynamics, Springer, pp. 1259–1276 (2015)

[47] Wang, C.-C., Chen, C.-K.: Bifurcation analysis of selfacting gas journal bearings. J. Trib. 123(4), 755–767 (2001)

[48] Zhang, J., Kang, W., Liu, Y.: Numerical method and bifurcation analysis of Jeffcott rotor system supported in gas journal bearings, J. Comput. Nonlinear Dynam. 4(1)

by Yang et al. [49] in rigid gas bearings, which results in a shock instability phenomenon; in other words, the nonlinear stability of the system is determined by the amplitude of the disturbance.

In fact, the disagreements about the existence of subsynchronous vibrations and stable or unstable periodic solutions come from different Hopf bifurcation behaviors (i.e., supercritical Hopf bifurcation and subcritical Hopf bifurcation) [50]. The investigations of different Hopf bifurcation behaviors are very common in oil journal bearings. Although most of them were based on analytical formulas for an infinitely long or an infinitely short journal bearing, the investigation carried out by Chasalevris [51] greatly highlighted the significance of the prediction of the Hopf bifurcation behaviors and the actual available speed range in oil journal bearing-rotor systems.

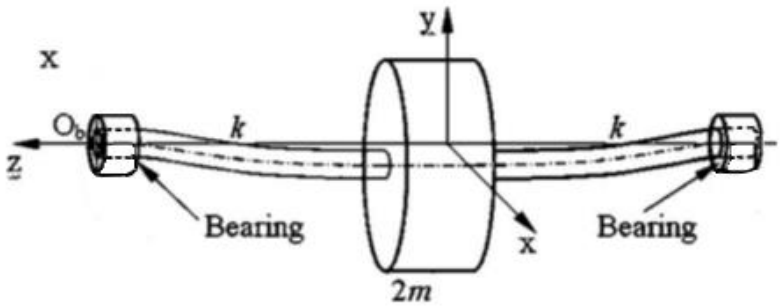

Fig. 1.2.3: The configuration of the GFBs-Jeffcott Rotor system [52]

In this Master Thesis, a rather simplistic model for bump foil properties of linearized stiffness and damping coefficients is utilized, taken directly from literature, and the first two design parameters are introduced as foil compliance and foil loss factor. The rotor model follows the Jeffcott rotor model and the third design parameter of shaft stiffness is introduced in the modelling, see Fig.1.2.3. The nonlinear dynamic characteristics of the system are investigated evaluating its time domain response for several sets of the key design properties of the system, like rotor stiffness, foil stiffness and damping and a study is performed on the quality of stability and of feasible motions experiencing bifurcations. The study of the work portions dissipated in the damping sources of gas and bump foil presents a correlation of the energy flow to the respective bifurcation developed, in another approach than Leister et al. [1] followed so as to achieve the reduction of undesired self-excited vibrations which affect instantly the stability of the system. A real system consisting of a high-speed centrifugal compressor rotor on gas foil bearings is also included in the simulations.

1.3. Quality of motion and stability

Regarding the rotating speed, which is the bifurcation parameter, and the design properties, which are the foil and shaft properties, the system may develop four types of motions. In the autonomous system there are two types of motion, the asymptotically stable motion and the unstable motion around a fixed-point equilibrium. If the system is non-autonomous (unbalanced system), there are also two types of motion, the orbital asymptotically stable and the unstable motion around a limit cycle. In this project, we study mostly the non-autonomous system, which is characterized like that due to the presence of the unbalance forces. In general, periodic, quasi-periodic and chaotic motions are expected to be generated by the system studied.

[49] Yang, P., Zhu, K.Q., Wang, X.L.: On the nonlinear stability of selfacting gas journal bearings. Tribol. Int. 42(1), 71–76 (2009)
[50] Seydel, R.: Practical Bifurcation and Stability Analysis, vol. 5. Springer Science & Business Media, Berlin (2009)
[51] Chasalevris, A.: Stability and Hopf bifurcations in rotor-bearing-foundation systems of turbines and generators. Tribol. Int. 145, 106154 (2020)
[52] Zhang, J., Kang, W., and Liu, Y. (2008). "Numerical Method and Bifurcation Analysis of Jeffcott Rotor System Supported in Gas Journal Bearings." ASME. *J. Comput. Nonlinear Dynam*. 4(1): 011007

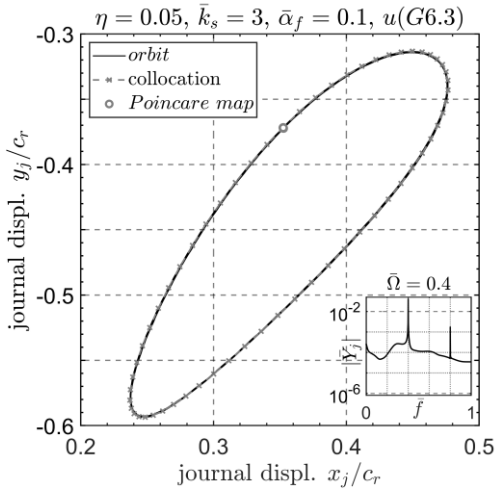

Fig. 1.3.1: Periodic solution with $T = 2 \cdot \pi / \omega$

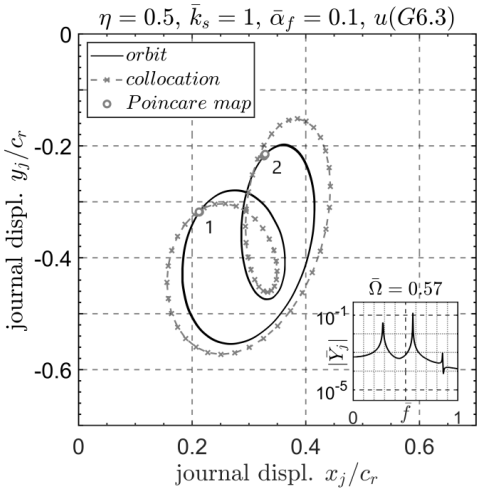

Fig. 1.3.2: Periodic solution with $T = 4 \cdot \pi / \omega$

A periodic solution is called a limit cycle if there are no other periodic solutions sufficiently close to it. In other words, a limit cycle is an isolated periodic solution and corresponds to an isolated closed orbit in the state space.

When a Floquet multiplier leaves the unit circle through -1, a period-doubling bifurcation takes place and the branch of stable periodic solutions that exists before the bifurcation continues as an unstable branch of periodic solutions after the bifurcation, a branch of stable period-doubled solutions is created if the bifurcation is supercritical, while a branch of unstable period-doubled solutions is destroyed if the bifurcation is subcritical [53].

In Fig. 1.3.1, we show a periodic orbit of a continuous-time system and its intersection with a one-sided Poincare section. The scenario after this periodic orbit undergoes a period-doubling bifurcation is depicted in Figure 1.3.2. The period-doubled orbit intersects the Poincare section two times, once at the point labeled 1 and another time at the point labeled 2. During the course of evolution on the period-doubled orbit, we successively flip between points 1 and 2 on the Poincare section. Therefore, a period-doubling bifurcation is also called a flip bifurcation. After k successive period-doubling bifurcations, we would have 2k points on the corresponding Poincare section.

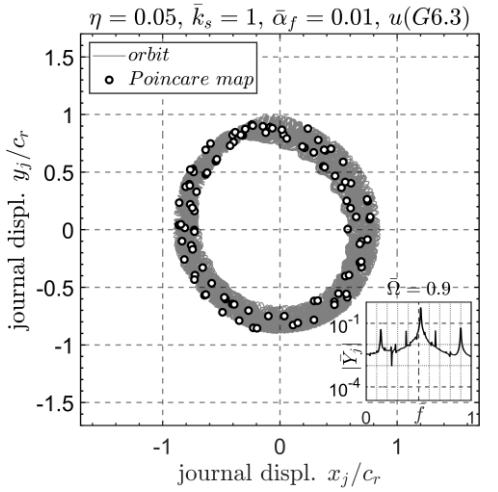

Fig. 1.3.3: Quasiperiodic solution

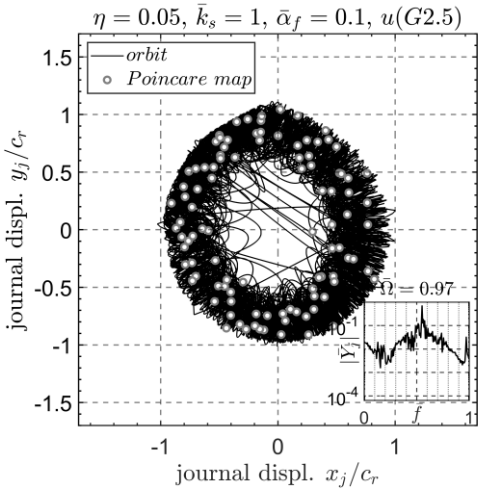

Fig. 1.3.4: Chaotic solution

[53] A. Nayfeh, B. Balachandran, (1995), "Applied nonlinear dynamics : analytical, computational, and experimental methods"

A quasiperiodic solution, see Fig. 1.3.3, is a dynamic solution characterized by two or more incommensurate frequencies. It is also called a k-period quasiperiodic solution if it is characterized by k incommensurate frequencies. Although the waveform of a quasiperiodic signal may look complex because of the presence of many sinusoids in it, calculating its spectrum would reveal its simplicity. In principle, one can use the spectrum to distinguish a quasiperiodic function from a periodic function in that the spikes in the spectrum of a quasiperiodic function are not spaced at integer multiples of a particular frequency. However, in practice, due to the difficulty of determining whether the ratio of two measured values is rational or irrational, a spectrum that appears to be that of a quasiperiodic function may be that of a periodic function with a very long period.[53]

Chaotic solutions, see Fig. 1.3.4, are also bounded like equilibrium, periodic, and quasiperiodic solutions. There is no precise definition for a chaotic solution because it cannot be represented through standard mathematical functions. However, a chaotic solution is an aperiodic solution, which is endowed with some special identifiable characteristics. From a practical point of view, chaos can be defined as a bounded steady-state behaviour that is not an equilibrium solution or a periodic solution or a quasiperiodic solution. The attractor associated with a chaotic motion in state space is not a simple geometrical object like a finite number of points, a closed curve, or a torus. In fact, it is not even a smooth surface; that is, it is not a manifold. Chaotic attractors are complicated geometrical objects that possess fractal dimensions. In contrast with the spectra of periodic and quasiperiodic attractors, which consist of a number of sharp spikes, the spectrum of a chaotic signal has a continuous broadband character. In addition to the broadband component, the spectrum of a chaotic signal often contains spikes that indicate the predominant frequencies of the signal. A chaotic motion is the superposition of a very large number of unstable periodic motions. Thus, a chaotic system may dwell for a brief time on a motion that is very nearly periodic and then may change to another periodic motion with a period that is k times that of the preceding motion. This constant evolution from one periodic motion to another produces a long-time impression of randomness while showing short term glimpses of order. Chaotic systems are also characterized by sensitivity to initial conditions; that is, tiny differences in the input can be quickly amplified to create overwhelming differences in the output. This is the so-called butterfly effect.[53]

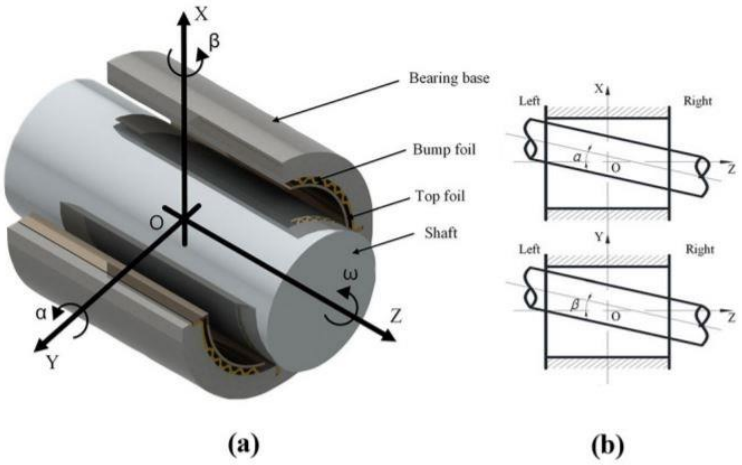

Fig. 1.3.4: Schematics of the geometry of misaligned gas foil bearing (a) The journal foil bearing (b) the misalignment condition [54]

[54] Li, H., Geng, H. and Lin, H. (2021), "Thermo-elastohydrodynamic analysis of the inhomogeneous foil bearing with misalignment", Industrial Lubrication and Tribology, Vol. 73 No. 6, pp. 891-896.

1.4. Design Optimization

Most of the considered rotating machinery is supposed to reach and to maintain a stable operating point after completing the run-up. However, as a result of the highly nonlinear bearing forces induced by the pressurized fluid, the existing equilibrium points of GFB rotor systems tend to become unstable for higher rotational speeds [1]. Subsequently, undesirable self-excited vibrations with comparatively large amplitudes may occur [55,56,57]. For this reason, an optimization scheme is applied in order to define such values for bump foil properties (stiffness and damping) that bifurcations become eliminated.

In the literature, few articles are reported showing the use of few optimization techniques for different types of bearings and most of the relevant literatures among those are summarized here. Choi and Yoon [58] optimized design variables for double row angular contact ball bearings of an automobile wheel-bearing unit using genetic algorithm (GA). Chakraborty et al. [59] presented an optimization problem on ball bearings. The design was established with five design variables, eight inequality constraints and the dynamic capacity as objective function. The problem was solved for the longest fatigue life by genetic algorithms; however, certain conditions like assembly angle was kept constant for all pairs of solutions. Rao and Tiwari [60] attempted a parametric study on the design variables specified by Chakraborty et al. [55] and applied bounds to the five constant variables involved in the constraints. The maximization of fatigue life is taken as objective function, and the genetic algorithm was used. Gupta et al. [61] applied Non-dominated Sorting Genetic Algorithm-II (NSGA-II) to optimize the ball bearing for three objective functions, i.e. the static capacity, dynamic capacity and elasto-hydrodynamic minimum film thickness, separately and pair-wise and parametric study was carried out. Ganesan and Mohankumar [62] shown application potential of NSGA-II to different domain of research. [67]

Kumar et al. [63] applied Genetic Algorithm (GA) to a constrained nonlinear design problem of cylindrical roller bearings (CRB) and chosen four design variables for optimization. In another study, Kumar et al. [64] applied GA for design optimization of CRB with the logarithmic profile crowning. NSGA-II on design optimization of high-speed angular contact ball bearing by considering two objective functions; spin frictional power loss and rating life on 7007AC bearing used by Wei and Chengzu [65]. Subsequently, Kumar et al. [59] attempted for design optimization

---

[55] Bonello, P.; Pham, H. M. (2014) The efficient computation of the nonlinear dynamic response of a foil-air bearing rotor system. Journal of Sound and Vibration, 333, 15, 3459–3478.

[56] Hoffmann, R.; Pronobis, T.; Liebich, R. (2014) Non-linear stability analysis of a modified gas foil bearing structure. In: Proceedings of the 9th IFToMM International Conference on Rotor Dynamics, Milan, Italy.

[57] Baum, C.; Hetzler, H.; Seemann, W. (2015) On the stability of balanced rigid rotors in air foil bearings. In: Proceedings of the SIRM 2015, Magdeburg, Germany(2015a).

[58] Choi, D.H.; Yoon, K.C.: A design method of an automotive wheel-bearing unit with discrete design variables using genetic algorithms. J. Tribol. 123, 181–187 (2001)

[59] Chakraborty, I.; Kumar, V.; Nair, S.B.; Tiwari, R.: Rolling element bearing design through genetic algorithms. Eng. Optim. 35(6), 649–659 (2003)

[60] Rao, B.R.; Tiwari, R.: Optimum design of rolling element bearings using genetic algorithms. Mech. Mach. Theory 42, 233–250 (2007)

[61] Gupta, S.; Tiwari, R.; Nair, S.B.: Multi-objective design optimization of rolling bearings using genetic algorithm. Mech. Mach. Theory 42, 1418–1443 (2007)

[62] Ganesan, H.; Mohankumar, G.: Optimization of machining techniques in CNC turning centre using genetic algorithm. Arab. J. Sci. Eng. 38, 1529–1538 (2013)

[63]Kumar, K.S.; Tiwari, R.; Reddy, R.S.: “Development of an optimum design methodology of cylindrical roller bearings using genetic algorithms. Int. J. Comput. Methods Eng. Sci. Mech. 9(6), 321–341 (2008)

[64] Kumar, K.S.; Tiwari, R.; Prasad, P.V.V.N.: An Optimum design of crowned cylindrical roller bearings using genetic algorithms. J. Mech. Des. 131(5), 051011 (2009)

[65] Wei, Y., Chengzu, R.: Optimal design of high speed angular contact ball bearing using a multi-objective evolution algorithm. In: Paper presented at the International Conference on Computing. Control and Industrial Engineering. IEEE, Wuhan, June 5–6 (2010)

on a tapered roller bearing. Waghole and Tiwari [66] successfully formulated nonlinear problem of needle roller bearing and optimized by using hybrid method which involved artificial bee colony algorithm (ABC) algorithm, differential search algorithm and grid search method. In another study, Tiwari and Waghole [67] presented the SOO of SRBs by considering the maximization of dynamic capacity as objective function, eight design parameters and twenty constraints. Using the artificial bee colony algorithm (ABCA), differential search algorithm (DSA), grid search method (GSM) and hybrid method (HM), the optimization problem was solved. The hybrid method gave the optimum solution. The constraint violation study and the sensitivity analysis were also carried out. [67]

It is observed from the above literature that relatively no work is done on the design optimization of the GFBs. Many deterministic optimization techniques can be applied for the nonlinear optimization problem of bearings, however the problem arises when numbers of design variables are more. With continuous research in the field of optimization techniques, nature-inspired heuristic optimization methods provide a better solution instead of classical optimization method. There are many nature-inspired well known and recently developed optimization algorithms such as Genetic Algorithm (GA), Artificial Bee Colony (ABC), artificial neural network (ANN), particle swarm optimization (PSO), Harmony Search (HS), water cycle algorithm (WCA), mine blast algorithm (MBA), etc. and many of those proved their suitability to many engineering optimization problems. However, some of these advanced optimization techniques have some limitations due to algorithm specific parameters. [68]

In the present work, an attempt has been made to implement Generalized Pattern Search (GPS) algorithm for optimization of the bump foil stiffness and damping of the gas foil bearing to minimize the inverse of dissipated energy in the gas film. The GPS algorithm were defined and analyzed by Torczon [69], for derivative-free unconstrained optimization on continuously differentiable functions using positive spanning directions. Lewis and Torczon [70] introduced the idea of using positive spanning directions with GPS. In [71], they showed that if the objective is continuously differentiable and if the set of directions that define the local search is chosen properly with respect to the boundary of the feasible region, then the GPS framework and convergence theory extend to bound constrained optimization. In [72], they show the same results for problems with a finite number of linear constraints. Both these extensions use the appealing "barrier" strategy of declaring any infeasible point to be unacceptable as a next iterate.

[66] Waghole, V.; Tiwari, R.: Optimization of needle roller bearing design using novel hybrid methods. Mech. Mach. Theory 72, 71–85 (2014)

[67] Tiwari, R.; Waghole, V.: Optimization of spherical roller bearing design using artificial bee colony algorithm and grid search method. Int. J. Comput. Methods Eng. Sci. Mech. 16(4), 221–233 (2015)

[68] Dandagwhal, R.D., Kalyankar, V.D. Design Optimization of Rolling Element Bearings Using Advanced Optimization Technique. *Arab J Sci Eng* 44, 7407–7422 (2019).

[69] Torczon V. (1997), "On the Convergence of Pattern Search Algorithms," SIAM Journal on Optimization Vol.7 No.1, 1–25.

[70] Lewis R.M., Torczon V. (1996), "Rank ordering and positive basis in pattern search algorithms," ICASE NASA Langley Research Center TR 96-71.

[71] Lewis R.M., Torczon V. (1999), "Pattern search algorithms for bound constrained minimization," SIAM Journal on Optimization, Vol.9, 1082-1099.

[72] Lewis R.M., Torczon V. (2000), "Pattern search methods for linearly constrained minimization," SIAM Journal on Optimization, Vol.10 No.3, 917–941.

2. MODELLING AND FORMULATION OF THE NONLINEAR DYNAMIC SYSTEM

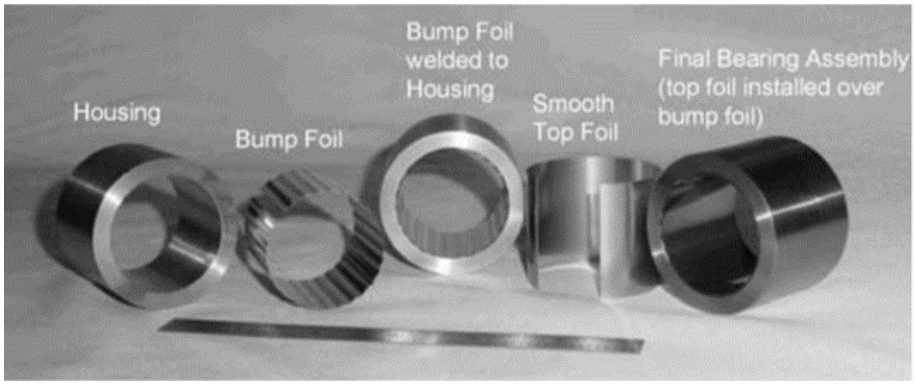

Fig. 2.1 Parts of the gas foil bearings at various stages of manufacturing process [10]

Gas foil bearings are compliant-surface hydrodynamic bearings that use ambient air as the lubricating fluid. A hydrodynamic pressure builds up within the small gap or film between the rotating shaft and the smooth top foil. Fig. 2.2 shows the configuration of a bump type GFB [73]. In Fig. 2.1 all the parts of which GFB consists. These parts are; the rigid part (housing), a thin top foil and a series of corrugated bump-strip supports. The leading edge of the thin foil is free, and the foil trailing edge is welded to the bearing housing. Beneath the top foil, a bump structure is laid on the inner surface of the bearing. The top foil of smooth surface is supported by a series of bumps acting as springs, thus making the bearing compliant. The bump strip provides a tunable structural stiffness [74]. Damping arises due to material hysteresis and dry-friction between the bumps and top foil, and between the bumps and the bearing inner surface [75].

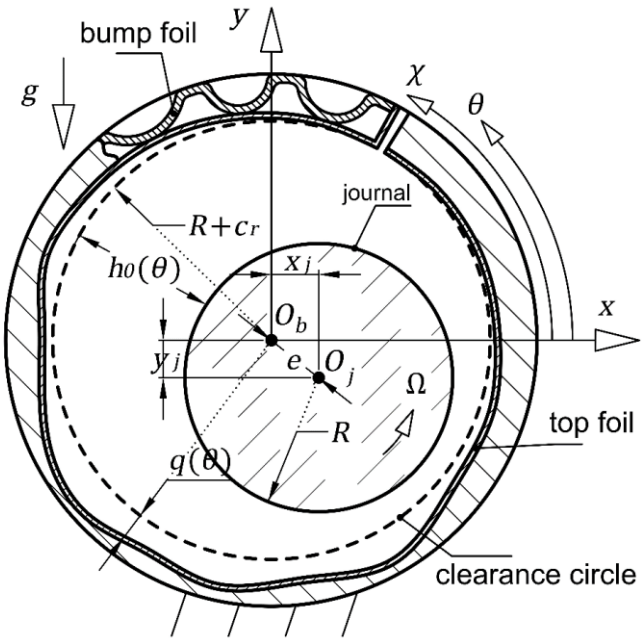

Fig. 2.2 Representation of a gas foil bearing cross section, key geometry and operating parameters

[73] DellaCorte, C., and Valco, M. J., 2000, "Load Capacity Estimation of Foil Air Journal Bearings for Oil-Free Turbomachinery Applications," NASA/TM—2000- 209782.
[74] Heshmat, H., Walowit, J. A., and Pinkus, O., 1983, "Analysis of Gas-Lubricated Foil Journal Bearings," J. Lubr. Tech., 105, pp. 647-655
[75] San Andrés, L., 1995, "Turbulent Flow Foil Bearings for Cryogenic Applications," J. Tribol., 117, pp. 185-195

Also, the journal's and bearing's rotational axes are considered parallel and their geometrical centers are denoted by $O_j(x_j, y_j)$ and $O_d(x_d, y_d)$ respectively. Their nominal radiuses are defined as R, $R+c_r$, where c_r is the nominal radial clearance.

The distance between O_j and O_b is the eccentricity $e=\sqrt{x_j^2+y_j^2}$. Coordinate θ is measured from the horizontal positive semi-axis of the bearing, as shown in Fig.2.2. The top foil deformation in radial direction is denoted by $q(\theta,t)$, considered positive when it is developed to the outer side of the bearing. The deflection of the foil is provoked by the pressure distribution $\boldsymbol{p}$ of the compressible gas flowing in the gap between journal and top foil and the bearing forces F_B induced by the latter. The pressure $p(x,z,t)$ is dependent on time τ in dynamic problem (whirling motion of the journal) and the spatial coordinates; the circumferential $x=R\cdot\theta$ and the axial one z. The location of foil starting and ending angle is denoted by the angular coordinate χ and in this project $\chi=\pi/2$ in which the foil is considered without any deformation q.

2.1. Elastoaerodynamic lubrication problem and resulting gas forces

The assumptions introduced in the lubrication problem are quite common: a) isothermal gas film, b) laminar flow, c) no-slip boundary conditions, d) continuum flow, e) negligible fluid inertia, f) ideal isothermal gas law $(p/\rho=\text{constant})$, g) negligible entrance and exit effects, and h) negligible curvature $(R\approx R+c_r)$. In general, solving the dimensional (DM) form of a problem can be computationally expensive. Thus, a dimensionless (DL) expression of the equations of the model can be a decisive factor in order to enhance time and memory efficiency, and additionally generic approach for the model and the results. The following transformations take place in order to define the dimensionless equations describing the problem. The Reynolds equation for compressible gas flow is given in Eq. (1), and it is an implicit function of time and of journal and foil kinematics.

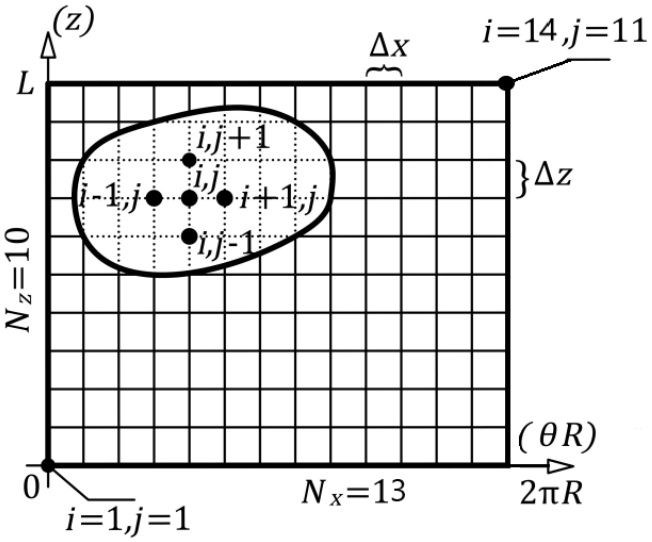

Fig.2.1.1 Finite difference grid $N_x \times N_z$ used for the evaluation of pressure distribution.

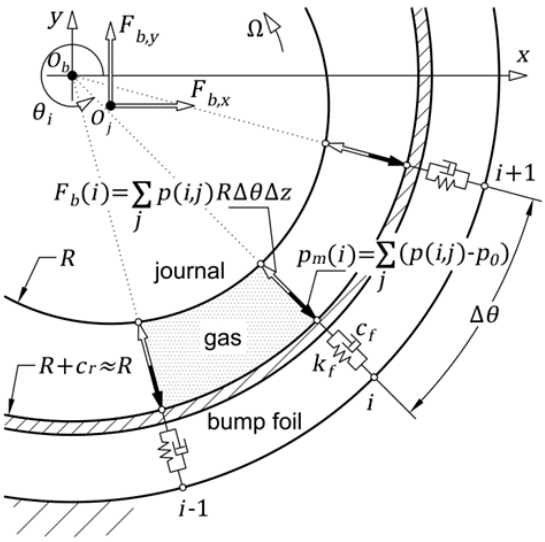

Fig.2.1.2 Modelling of gas pressures and forces acting on the rotating journal and the compliant foil structure.

$$\frac{\partial}{\partial \bar{x}}\left(\bar{p}\bar{h}^3\frac{\partial \bar{p}}{\partial \bar{x}}\right)+\kappa^2\frac{\partial}{\partial \bar{z}}\left(\bar{p}\bar{h}^3\frac{\partial \bar{p}}{\partial \bar{z}}\right)=\bar{\Omega}\frac{\partial}{\partial \bar{x}}\left(\bar{p}\bar{h}\right)+2\frac{\partial}{\partial \tau}\left(\bar{p}\bar{h}\right) \quad (1)$$

The dimensionless parameters of gas pressure $\bar{p}$, gas film thickness $\bar{h}$, spatial coordinates (circumferential and axial respectively) θ and $\bar{z}$, time τ, rotating speed $\bar{\Omega}$, and ratio $\kappa = R/L_b$ are included in the elastoaerodynamic lubrication problem of Eq. (1).

Analytical solution for Eq.(1) cannot be defined, so we made an approach to evaluate the pressure distribution with the Finite Difference Method **(**FDM). The pressure domain is converted into a grid of $i=1,\ldots,N_X+1$ and $j=1,\ldots,N_Z+1$ points, where i and j are the indexes in the circumferential and axial direction, see Fig. 2.2.1 and Fig. 2.2.2.

Concluding remarks on the current study should highlight that the geometry of a specific bearing type and the relative properties of foundation with respect to the rotor, have major influence in the type of bifurcation of rotor-bearing-foundation systems. The turbine and generator rotors may have the potential to render subcritical bifurcations. At this case, instability occurs at rotating speeds lower than the threshold speed of instability.

The Reynolds equation is first rewritten defining the first time derivative of the pressure in Eq. (2a) and after some math in Eq. (2b). Then the discrete Reynolds equation is defined in the grid points expressing the partial derivatives with finite differences.

$$\frac{\partial}{\partial \tau}\left(\bar{p}\bar{h}\right)=\frac{1}{2}\frac{\partial}{\partial \bar{x}}\left(\bar{p}\bar{h}^3\frac{\partial \bar{p}}{\partial \bar{x}}\right)+\frac{\kappa^2}{2}\frac{\partial}{\partial \bar{z}}\left(\bar{p}\bar{h}^3\frac{\partial \bar{p}}{\partial \bar{z}}\right)-\frac{\bar{\Omega}}{2}\frac{\partial}{\partial \bar{x}}\left(\bar{p}\bar{h}\right) \quad (2a)$$

$$\dot{\bar{p}}=\frac{1}{2\bar{h}}\frac{\partial}{\partial \bar{x}}\left(\bar{p}\bar{h}^3\frac{\partial \bar{p}}{\partial \bar{x}}\right)+\frac{\kappa^2}{2\bar{h}}\frac{\partial}{\partial \bar{z}}\left(\bar{p}\bar{h}^3\frac{\partial \bar{p}}{\partial \bar{z}}\right)-\frac{\bar{\Omega}}{2\bar{h}}\frac{\partial}{\partial \bar{x}}\left(\bar{p}\bar{h}\right)-\frac{\bar{p}\dot{\bar{h}}}{\bar{h}} \quad (2b)$$

The gas film thickness as shown in Fig.2.1 is defined in Eq. (3) for the continuous and the discrete pressure domain (finite difference grid) where $\bar{q}=\bar{q}(\theta)$ is the foil deformation in radial direction.

$$\bar{h}=1-\bar{x}_j\cos\theta-\bar{y}_j\sin\theta+\bar{q}, \qquad \bar{h}_i=1-\bar{x}_j\cos\theta_i-\bar{y}_j\sin\theta_i+\bar{q}_i \quad (3)$$

Boundary and initial conditions of the problem are defined in continue. Ambient pressure is assumed at the starting and ending angle of the foil (periodic boundary condition) in Eq. (4) (in the continuous and the discrete pressure domain):

$$\bar{p}(\tau,\theta_0,\bar{z})=\bar{p}(\tau,\theta_0+2\pi,\bar{z})=1, \quad \bar{p}_{1,j}=\bar{p}_{N_X+1,j}=1 \quad (4)$$

Taking into account the symmetry of the problem, instead of assuming the gas pressure equal to the ambient p_o at the axial ends, $\bar{p}(\bar{z}=0)=\bar{p}(\bar{z}=1)=1$, the boundary condition can be written in Eq. (5) (for the continuous and the discrete pressure domain). In this way the lubrication problem is solved in the half domain, reducing the evaluation cost severely.

$$\left.\frac{\partial \bar{p}}{\partial \bar{z}}\right|_{\bar{z}=1/2}=0, \qquad \frac{\bar{p}_{i,N_Z/2}-\bar{p}_{i,N_Z/2-1}}{\Delta\bar{z}}=0 \quad (5)$$

Last, the initial conditions for the dimensionless form of the problem are defined in Eq. (6) (in the continuous and the discrete pressure domain).

$$\bar{p}\left(\tau=0,\theta,\bar{z}\right)=1,\ \overset{\langle t_0\rangle}{\bar{p}}_{i,j}=1 \text{ and } \bar{q}\left(\tau=0,\theta\right)=0,\quad \overset{\langle t_0\rangle}{\bar{q}}_{i}=0 \tag{6}$$

The nonlinear gas forces, after evaluating pressure $\bar{p}$ (as $\bar{p}_{i,j}$), can be determined in Eq. (7) where $\Delta\bar{x}=2\pi/N_X$ and $\Delta\bar{z}=1/N_Z$.

$$\bar{F}_{B,X}=-\int_0^{2\pi}\int_0^1\left(\bar{p}-1\right)\cos\theta d\bar{z}d\theta=-\sum_{i=2}^{N_X}\sum_{j=2}^{N_Z}\left(\left(\bar{p}_{i,j}-1\right)\cos\theta_i\Delta\bar{x}\Delta\bar{z}\right) \tag{7a}$$

$$\bar{F}_{B,Y}=-\int_0^{2\pi}\int_0^1\left(\bar{p}-1\right)\sin\theta d\bar{z}d\theta=-\sum_{i=2}^{N_X}\sum_{j=2}^{N_Z}\left(\left(\bar{p}_{i,j}-1\right)\sin\theta_i\Delta\bar{x}\Delta\bar{z}\right) \tag{7b}$$

In this way the aerodynamic problem renders $N_X\cdot N_Z$ ODEs of 1st order with respect to the time derivative of the point pressure in Eq. (8)

$$\dot{\bar{\mathbf{p}}}=\left\{\dot{\bar{p}}_{i,j}\right\}=\mathbf{f}_B\left(\bar{\mathbf{p}},\bar{\mathbf{x}},\dot{\bar{\mathbf{x}}},\bar{\mathbf{q}},\dot{\bar{\mathbf{q}}}\right) \tag{8}$$

The vectors $\bar{\mathbf{x}}$ and $\bar{\mathbf{q}}$ may be perceived as $\bar{\mathbf{x}}=\left\{x_j \quad y_j \quad x_d \quad y_d\right\}^{\mathrm{T}}$ representing the journal motion (coupled to the disc motion through the rotor's equations of motion) and $\bar{\mathbf{q}}=\left\{\bar{q}_1 \quad \bar{q}_1 \quad \dots \quad \bar{q}_{N_X}\right\}^{\mathrm{T}}$ representing the foil motion (coupled to the journal motion through the Reynolds equation due to the gas film thickness function).

It is important to mention that it's quite common in GFBs for sub-ambient pressures to arise. These sub-ambient pressures can cause the top foil to separate from the bumps into a position in which the pressure on both sides of the pad is equalized. Heshmat et al. [76-77] introduced a set of boundary conditions accounting for this separation effect. More specifically, a simple Gümbel [78] boundary condition is imposed, meaning that sub-ambient pressures are discarded when integrating the pressure in Eq. (7) to obtain the bearing force components $\bar{F}_{B,X}$, $\bar{F}_{B,Y}$ essentially leaving the sub-ambient regions ineffective. In terms of numerical calculations, the assumption made by Heshmat [2-3] can be simply explained as following: in case fluid pressure p is lower than the ambient p_0, then the former should be considered equal to p_0 and the foil deformation at these points will be zero $\left(\bar{q}_i=0 \text{ for } \bar{p}_i<1\right)$.

The simplified model for the bump foil structure is depicted at Fig. 2.1.3. The structure consists of N_X-2 linear massless elements of stiffness $\bar{k}_f$ (compliance $\bar{a}_f=1/\bar{k}_f$) and damping $\bar{c}_f$. The springs and dampers mount the corresponding N_X-1 top foil stripes of area $\Delta x\cdot L_b$ (or dimensionless area $\Delta\bar{x}\cdot 1$), see Fig.2.1.2. The top foil of the bearing is not covering a complete

[76] H. Heshmat, J.A. Walowit, O. Pinkus (1983) Analysis of gas lubricated compliant thrust bearings, Journal of Lubrication Technology 105: 638–646.

[77] H. Heshmat, J.A. Walowit, O. Pinkus (1983) Analysis of gas-lubricated foil journal bearings, Journal of Lubrication Technology 10: 647–655.

[78] B.J. Hamrock (1994) Fundamentals of Fluid Film Lubrication, McGraw-Hill Series in Mechanical Engineering, McGraw-Hill Inc., NewYork.

cylinder; a single gap can be found at $\theta = \theta_0$, see Fig.2.2, where foil is clamped to the bearing housing. Therefore, the moving top foil stripes are $N_X - 1$, see Fig.2.1.2.

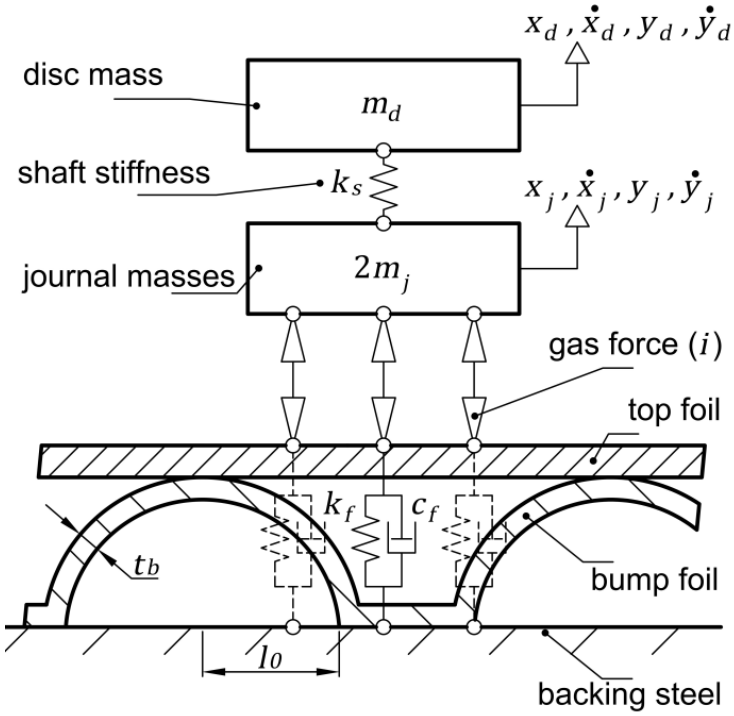

Fig. 2.1.3 Representation of the simulation model; Bump foil structure is modeled by springs and dampers

The top foil stripes are assumed to remain parallel to the bearing surface during their motion, therefore no axial coordinate is required for the top foil motion. The geometry of the foil structure and its properties, shown in Fig.2.2 and Fig.2.1.2, render the dimensionless compliance $\bar{\alpha}_f = 2p_0 (l_0 / t_b)^3 (1-\nu^2) s_0 / (c_r E)$ [79]. The motion of each of the top foil stripe is excited by the mean gas pressure $\bar{p}_{m,i}$ acting on the top of it, creating the gas force $\bar{F}_B(i)$, see Figs. 2.1.2 and Fig.2.1.3. The mean gas pressure $\bar{p}_{m,i}$ is defined in Eq. (9) (in the continuous and discrete pressure domain), for dimensioned and dimensionless form.

$$p_m(\theta) = \frac{1}{L_b}\int_0^{L_b} p(\theta)dz, \quad p_{m,i} = \frac{1}{L_b}\sum_{j=2}^{N_Z}\left(p_{i,j}\Delta z\right), \qquad \bar{p}_{m,i} = \frac{1}{1}\sum_{j=2}^{N_Z}\left(\bar{p}_{i,j}\Delta\bar{z}\right) = \frac{1}{N_Z}\sum_{j=2}^{N_Z}\left(\bar{p}_{i,j}\right) \tag{9}$$

The foil stiffness and damping coefficient are given as $\bar{k}_f = 1/\bar{\alpha}_f$ and $\bar{c}_f = \eta\bar{k}_f$ for foil motion synchronous to the excitation. The $N_X - 1$ ODEs that describe the top foil radial displacement $\bar{q}_i$ of the stripe i are defined in Eq. (10).

$$\bar{c}_f\dot{\bar{q}}_i + \bar{k}_f\bar{q}_i = \bar{p}_{m,i}, \qquad i = 2,3,...,N_X \tag{10}$$

The ODEs in Eq. (10) may be written as in Eq. (11) to be used in continue.

$$\dot{\bar{\mathbf{q}}} = \left\{\dot{\bar{q}}_i\right\} = \mathbf{f}_F\left(\bar{\mathbf{q}}, \bar{\mathbf{p}}, \bar{\mathbf{x}}, \dot{\bar{\mathbf{x}}}\right) \tag{11}$$

[79] Bhore S.P., Darpe A.K. (2013) Nonlinear dynamics of flexible rotor supported on the gas foil journal bearings. J. of Sound and Vib. 332:5135-5150

2.2. Model of the flexible rotor

The equations of motion for the Jeffcott rotor shown in Fig. 2.2.1 are defined in Eqs. (12) for the journal and the disc, in the two main directions.

$$\ddot{\bar{x}}_j = \frac{m_d}{2m_j}\bar{k}_s\left(\bar{x}_d - \bar{x}_j\right) + \xi \cdot \bar{F}_{B,X}\,, \qquad \ddot{\bar{y}}_j = \frac{m_d}{2m_j}\bar{k}_s\left(\bar{y}_d - \bar{y}_j\right) + \xi \cdot \bar{F}_{B,Y} - \sigma \tag{12a}$$

$$\ddot{\bar{x}}_d = -\bar{k}_s\left(\bar{x}_d - \bar{x}_j\right) + \bar{F}_{U,X}\,, \qquad \ddot{\bar{y}}_d = -\bar{k}_s\left(\bar{y}_d - \bar{y}_j\right) + \bar{F}_{U,Y} - \sigma \tag{12b}$$

The ODEs in Eqs. (12) may be written as in Eq. (13) in the state space representation to be used in continue.

$$\dot{\bar{\mathbf{x}}} = \mathbf{f}_R\left(\bar{\mathbf{p}}, \bar{\mathbf{x}}, \dot{\bar{\mathbf{x}}}, \bar{\mathbf{q}}, \dot{\bar{\mathbf{q}}}\right) \tag{13}$$

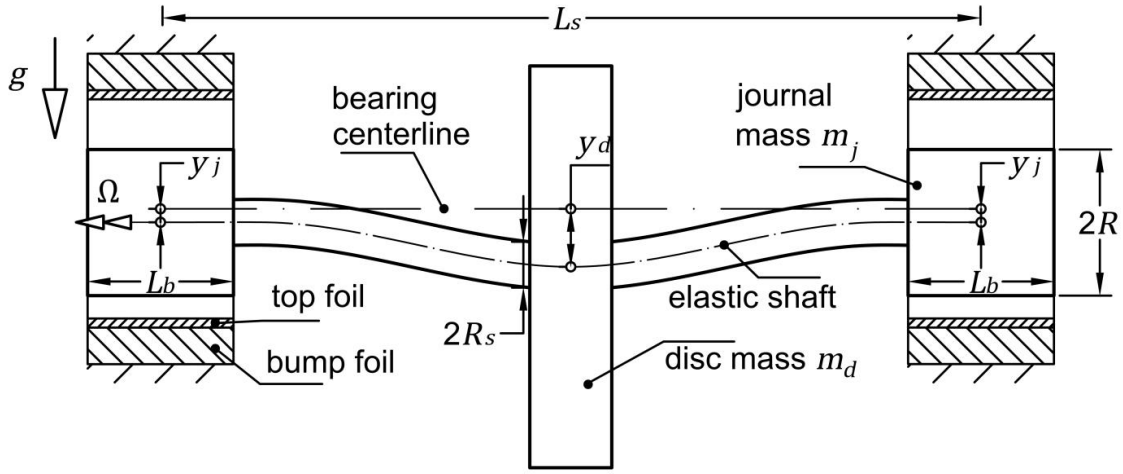

Fig. 2.2.1. Representation of a Jeffcott (Laval) rotor of length L_s and radious R_s with a mass m_d at its center, mounted on two GFBs of equal radius $R_b = R + c_r \approx R$ and length L_b, carrying two masses m_j at its ends.

In Eqs. (12) $\bar{k}_s$ is the dimensionless shaft stiffness coefficient, ξ and σ are dimensionless parameters defined in Eq. (14).

$$\xi = \frac{36\mu^2 L R^5}{m_j p_0 c_r^{\,5}}, \qquad \sigma = \frac{36\mu^2 R^2 g}{p_0^{\,2} c_r^{\,5}} \tag{14}$$

In addition, in Eq. (12), $\bar{F}_{U,X}$, $\bar{F}_{U,Y}$ are the dimensionless unbalance forces defined in Eq. (15a) for constant rotating speed $\bar{\Omega}$, and in Eq. (15b) for linearly varying rotating speed $\bar{\Omega} = \bar{a} \cdot \tau$ with constant acceleration $\bar{a}$.

$$\bar{F}_{U,X} = \varepsilon \cdot \bar{\Omega}^2 \cos\bar{\varphi}_r\,, \qquad \bar{F}_{U,Y} = \varepsilon \cdot \bar{\Omega}^2 \sin\bar{\varphi}_r\,, \qquad \bar{\varphi}_r = \bar{\Omega}\tau \tag{15a}$$

$$\bar{F}_{U,X} = \varepsilon\left(\bar{\Omega}^2 \cos\bar{\varphi}_r + \bar{a}\sin\bar{\varphi}_r\right), \qquad \bar{F}_{U,Y} = \varepsilon\left(\bar{\Omega}^2 \sin\bar{\varphi}_r - \bar{a}\cos\bar{\varphi}_r\right), \qquad \bar{\varphi}_r = \bar{a}\tau^2/2 \tag{15b}$$

Dimensionless unbalance eccentricity $\varepsilon = e_u / c_r$ follows in this paper the ISO unbalance grades (G-grades) for low, medium, and high unbalance as G1, G2.5 and G6.3 correspondingly. The unbalance located in the disc is of magnitude $u = \left(m_d + 2m_j\right)e_u$ at each case, and the corresponding

eccentricity e_u is given in Eq. (16), where the service speed of the system is selected at $\Omega_r = 2500\,\text{rad/s}$.

$$e_u[\text{mm}] = \frac{G}{\Omega_r[\text{rad/s}]}, \qquad G = 1,\ 2.5,\ 6.3 \tag{16}$$

For instance, the notation $u(G2.5)$ used in continue refers to the unbalance eccentricity of $e_u(G = 2.5) = 9.55 \cdot 10^{-6}[\text{m}]$.

2.3. Composition and solution of the dynamic system

The Eqs. (8), (11), and (13) compose a coupled ODE system which is separately defined by the discretized Reynolds equation in the $\mathbf{f}_B$ equations, the foil motion in $\mathbf{f}_F$ equations, and the rotor motion in $\mathbf{f}_R$ equations. The coupled nonlinear ODE system can be defined in Eq. (17) expressing a non-autonomous dynamic system which will be studied with respect to the bifurcation parameter $\bar{\Omega}$. The ODE system is characterized as non-autonomous due to the explicit time presence in the equations of unbalance forces, see Eq. (15). The state vector $\bar{\mathbf{s}}$ and the respective functions $\mathbf{f}$ are defined in Eq. (18).

$$\dot{\bar{\mathbf{s}}} = \mathbf{f}\left(\bar{\mathbf{s}}, \bar{\Omega}, \tau\right) \tag{17}$$

$$\bar{\mathbf{s}} = \left\{\bar{\mathbf{p}} \quad \bar{\mathbf{q}} \quad \bar{\mathbf{x}}\right\}^{\mathrm{T}},\ \mathbf{f} = \left\{\mathbf{f}_B \quad \mathbf{f}_F \quad \mathbf{f}_R\right\}^{\mathrm{T}} \tag{18}$$

The total number of equations in Eq. (17) (size of vector function $\mathbf{f}$) is $N = (N_X \cdot N_Z) + (N_X - 1) + 8$ with the first term coming from the pressure equations, the second term coming from the foil equations, and the third term from the rotor equations in state space.

The ODE system in Eq. (17) renders the time response of the physical system when time integration is applied. The system is characterized as stiff and special algorithms may be applied for time integration [80]. Furthermore, the Reynolds equation can be reduced in size applying an order reduction method [43], improving the computational cost. The time integration can handle both cases of unbalance equations, for constant rotating speed or for run-up, see Eq. (15).

An orthogonal collocation method [81] is applied for the computation of limit cycle motions produced by the ODE system in Eq. (17) at a constant $\bar{\Omega}$; Eqs. (15a) apply for unbalance forces. Numerical continuation of limit cycles has been programmed by the authors according to pseudo arc length continuation method [82,83,84,85] with embedded collocation scheme [82]. The

[80] Shampine, L. F. and M. W. Reichelt, (1997), "The MATLAB ODE Suite," SIAM Journal on Scientific Computing, Vol. 18, pp. 1–22.
[81] Doedel, E.J.: Lecture Notes on Numerical Analysis of Nonlinear Equations, Department of Computer Science, Concordia University, Montreal, Canada
[82] Doedel, E.J., Keller, H.B., Kernevez, J.P. (1991): Numerical analysis and control of bifurcation problems (II): Bifurcation in infinite dimensions. International Journal of Bifurcation and Chaos 1(3), 745-772.
[83] Ascher, U.M., Mattheij, R.M.M, Russell, R.D., (1995): Numerical Solution of Boundary Value Problems for Ordinary Differential Equations. SIAM Classics in Applied Mathematics ser. 13 1st ed..
[84] Meijer H., Dercole, F., Olderman, B., (2009): Numerical bifurcation analysis. Encyclopedia of Complexity and Systems Science, R. A. Meyers Ed., Springer New York, 6329-6352.
[85] Allgower, E. L., Georg, K., (2003): Introduction to Numerical Continuation Methods. Society for Industrial and Applied Mathematics.

formulation of the method is defined also in the following section. As the collocation method cannot handle non-autonomous ODE systems, Eq. (17) has to be converted to autonomous. This is achieved by coupling the ODE system of Eq. (17) with a two DoF oscillator, see Eq. (19), whose unique solution is a harmonic motion of frequency $\bar{\Omega}$, see Eq. (20) [82].

$$\dot{\bar{s}}_{N+1} = f_{N+1} = \bar{s}_{N+1} + \bar{\Omega} \cdot \bar{s}_{N+2} - \bar{s}_{N+1} \cdot \left(\bar{s}_{N+1}^2 + \bar{s}_{N+2}^2 \right) \tag{19a}$$

$$\dot{\bar{s}}_{N+2} = f_{N+2} = -\bar{\Omega} \cdot \bar{s}_{N+1} + \bar{s}_{N+2} - \bar{s}_{N+2} \cdot \left(\bar{s}_{N+1}^2 + \bar{s}_{N+2}^2 \right) \tag{19b}$$

$$\bar{s}_{N+1} = \cos\left(\bar{\Omega} \tau \right), \quad \bar{s}_{N+2} = \sin\left(\bar{\Omega} \tau \right) \tag{20}$$

The final autonomous ODE system is of size $N+2$ and is defined in Eq. (21) with the unbalance forces are defined for constant rotating speed, as in Eq. (22).

$$\dot{\tilde{\bar{\mathbf{s}}}} = \tilde{\mathbf{f}} \left(\tilde{\bar{\mathbf{s}}}, \bar{\Omega} \right) \tag{21a}$$

$$\tilde{\bar{\mathbf{s}}} = \left\{ \bar{\mathbf{s}}^{\mathrm{T}} \quad \bar{s}_{N+1} \quad \bar{s}_{N+2} \right\}^{\mathrm{T}}, \quad \tilde{\mathbf{f}} = \left\{ \mathbf{f}^{\mathrm{T}} \quad f_{N+1} \quad f_{N+2} \right\}^{\mathrm{T}} \tag{21b}$$

$$\bar{F}_{U,X} = \varepsilon \cdot \bar{\Omega}^2 \bar{s}_{N+1}, \bar{F}_{U,Y} = \varepsilon \cdot \bar{\Omega}^2 \bar{s}_{N+2} \tag{22}$$

3. APPLICATION OF NUMERICAL CONTINUATION

3.1. Time Integration

In an initial value problem, the ODE is solved by starting from an initial state. Using the initial condition, y_0 , as well as a period of time over which the answer is to be obtained, (t_0, t_f) , the solution is obtained iteratively. At each step the solver applies a particular algorithm to the results of previous steps. At the first such step, the initial condition provides the necessary information that allows the integration to proceed. The final result is that the ODE solver returns a vector of time steps $t = [t_0, t_1, t_2, ..., t_f]$ as well as the corresponding solution at each $y = [y_0, y_1, y_2, ..., y_f]$. [86]

For some ODE problems, the step size taken by the solver is forced down to an unreasonably small level in comparison to the interval of integration, even in a region where the solution curve is smooth. These step sizes can be so small that traversing a short time interval might require millions of evaluations. This can lead to the solver failing the integration, but even if it succeeds it will take a very long time to do so. Equations that cause this behavior in ODE solvers are said to be stiff. Solvers that are designed for stiff ODEs, known as stiff solvers, typically do more work per step. The pay-off is that they are able to take much larger steps, and have improved numerical stability compared to the non-stiff solvers. [87]

Our system can be very stiff, depending on the shaft properties and bump foil properties, so we use a stiff solver. The solver that we chose is ode15s, which is a variable-step, variable-order (VSVO) solver based on the numerical differentiation formulas (NDFs) of orders 1 to 5. Optionally, it can use the backward differentiation formulas (BDFs, also known as Gear's method) that are usually less efficient. Also, it has the best accuracy compared with the other stiff solvers, like ode23s, ode23t and ode23tb [80,88].

3.2. Numerical Continuation and Collocation

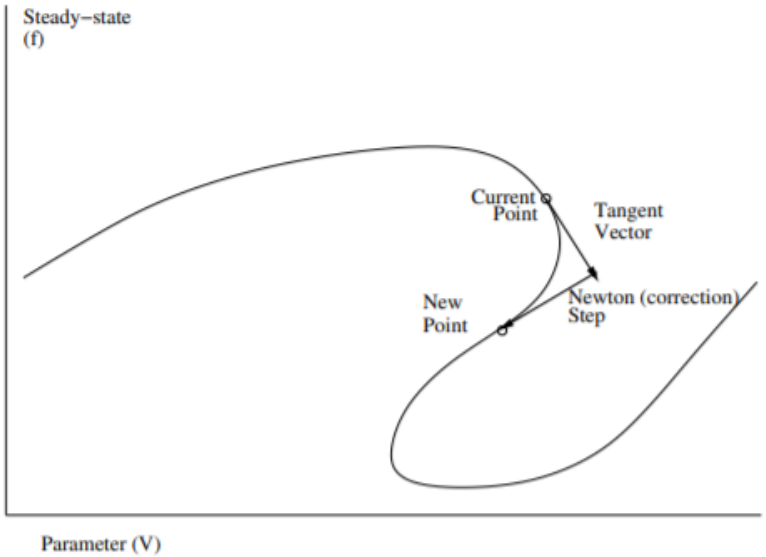

Fig. 1.1.1: Example of One Step of Pseudo-Arc Length Continuation [89]

[86] The MathWorks, Inc., “Choose an ODE solver”, https://www.mathworks.com/help/matlab/math/choose-an-ode-solver.html
[87] The MathWorks, Inc., “Solve stiff ODEs”, https://www.mathworks.com/help/matlab/math/solve-stiff-odes.html
[88] Shampine, L. F., M. W. Reichelt, and J.A. Kierzenka, (1999), “Solving Index-1 DAEs in MATLAB and Simulink”, SIAM Review, Vol. 41, pp. 538–552.
[89] Matthew S. Lasater, Carl Tim Kelley, Andrew G. Salinger, Dwight L. Woolard, and Peiji Zhao, (2004), "Enhancement of numerical computations of the Wigner-Poisson equations for application to the simulation of THz-frequency RTD oscillators", Proc. SPIE 5584, Chemical and Biological Standoff Detection II

Pseudo-arclength continuation is a well-established method for constructing a numerical curve comprising solutions of a system of nonlinear equations. In many complicated high-dimensional systems, the corrector steps within pseudo-arclength continuation are extremely costly to compute; as a result, the step-length of the preceding prediction step must be adapted carefully to avoid prohibitively many failed steps. [90]

The authors programmed the collocation method embedded to a pseudo arc length continuation method for the evaluation of limit cycles as the bifurcation parameter (rotating speed Ω) changes at discrete values. The methodology is similar to this presented in [81]. The problem is to find the solution branches $\boldsymbol{x}(\boldsymbol{\xi_0}, t, \Omega)$ for the following Boundary Value Problem:

$$\dot{\boldsymbol{x}} = \boldsymbol{f}(\boldsymbol{x}, \Omega), \qquad \boldsymbol{x}(\boldsymbol{\xi_0}, 0, \Omega) = \boldsymbol{x}(\boldsymbol{\xi_0}, T, \Omega) \tag{23-24}$$

The ODE system in Eq. (23) in identical to the ODE system in Eq. (21a) and Ω is the continuation parameter (bifurcation parameter) expressing the rotating speed of the shaft, $\boldsymbol{\xi_0}$ is an initial state vector that belongs to the solution curve $\boldsymbol{x}$ and T is the period of the solution. If time t is rescaled to $[0,1]$, Eqs. (23) and (24) become

$$\dot{\boldsymbol{x}} = T \cdot \boldsymbol{f}(\boldsymbol{x}, \Omega), \;\; \boldsymbol{x}(\boldsymbol{\xi_0}, 0, \Omega) = \boldsymbol{x}(\boldsymbol{\xi_0}, 1, \Omega) \tag{25-26}$$

The period T is unknown so an additional equation (phase condition) is required

$$\varphi = \int_0^1 \langle \boldsymbol{x}, \dot{\boldsymbol{x}}_0 \rangle \, dt = 0 \tag{27}$$

where $\langle \boldsymbol{x}, \dot{\boldsymbol{x}}_0 \rangle$ denotes the scalar product and $\dot{\boldsymbol{x}}_0$ is the time derivative of the previous solution. If the pseudo arc length is used as a continuation parameter, then Ω also becomes an unknown and an additional equation is required (pseudo arc length condition),

$$\psi = \int_0^1 \langle \boldsymbol{x} - \boldsymbol{x}_0, \boldsymbol{x}_0' \rangle \, dt + (T - T_0) T' + (\Omega - \Omega_0) \Omega' - \Delta s = 0 \tag{28}$$

where $(\;)'$ denotes the derivative with respect to arc length $d(\cdot)/ds$. Setting $\boldsymbol{u} = (\boldsymbol{x}, T, \Omega)$ and writing Eq. (25) and (26) as $\mathbf{F}(\boldsymbol{u}) = \{\mathbf{0}\}$ the system to solve becomes

$$\mathbf{H}(\boldsymbol{u}) = \begin{bmatrix} \mathbf{F}(\boldsymbol{u}) \\ \varphi(\boldsymbol{x}) \\ \psi(\boldsymbol{u}) \end{bmatrix} = \begin{Bmatrix} \mathbf{0} \\ 0 \\ 0 \end{Bmatrix} \tag{29}$$

and Newton's method for solving (29) is

$$\boldsymbol{u}^{i+1} = \boldsymbol{u}^i - \left[\mathbf{A}(\boldsymbol{u}^i) \right]^{-1} \mathbf{H}(\boldsymbol{u}^i) \tag{30}$$

where

$$\mathbf{A}(\boldsymbol{u}) = \begin{bmatrix} \dfrac{\partial \mathbf{F}}{\partial \boldsymbol{x}} & \dfrac{\partial \mathbf{F}}{\partial T} & \dfrac{\partial \mathbf{F}}{\partial \Omega} \\ \dfrac{\partial \varphi}{\partial \boldsymbol{x}} & 0 & 0 \\ \boldsymbol{x}' & T' & \Omega' \end{bmatrix} \tag{31}$$

[90] D. A. Aruliah, L. van Veen and A. Dubitski, (2012), "A parallel adaptive method for pseudo-arclength continuation", J. Phys.: Conf. Ser. 385 012008

which is iterated until a suitable convergence criterion is satisfied. The arc length derivatives $d\boldsymbol{u}/ds$ can be calculated either by backwards differences or by solving

$$\mathbf{A}\frac{d\boldsymbol{u}}{ds} = \{0 \quad \cdots \quad 0 \quad 1\}^{\mathrm{T}} \tag{32}$$

The final step is to discretize in time and calculate $\mathbf{A}$. To this end the method of orthogonal collocation at Gauss points with piece-wise polynomials was used. An overview of the method applied to nonlinear BVPs with periodicity boundary conditions with unknown period is given below.

The time interval $[0,1]$ is discretized into N sub-intervals. For the i^{th} sub-interval the collocation equations must be assembled at the required time nodes

$$t_{ij} = t_i + h_i\rho_j, \qquad i = 1,2,\ldots,N, \qquad j = 1,2,\ldots,m \tag{33}$$

Where $h_i = t_{i+1} - t_i$ the length of the time sub-interval i and ρ_j are chosen as the zeroes of an m^{th} order Legendre polynomial. At the above time nodes, an initial solution $\boldsymbol{x}_{ij}$ must be provided along with the function evaluation $T\cdot\boldsymbol{f}\left(\boldsymbol{x}_{ij},\Omega\right)$(abbreviated henceforth as $\boldsymbol{f}_{ij}$), Jacobian $\frac{\partial\boldsymbol{f}}{\partial\boldsymbol{x}}\left(\boldsymbol{x}_{ij},\Omega\right)$, and parameter derivative (for the case of pseudo arc length continuation) $\frac{\partial\boldsymbol{f}}{\partial\Omega}\left(\boldsymbol{x}_{ij},\Omega\right)$. Equivalently, the values $\boldsymbol{x}_{ij}$ can be extracted from the solutions at the global time nodes t_i as

$$x_{ij} = x_i + h_i\sum_{l=1}^{m} a_{jl}\,f_{il}, \qquad x_{i+1} = x_i + h_i\sum_{l=1}^{m}\beta\,f_{il} \tag{34-35}$$

Where $a_{j1}, a_{j2},\ldots,a_{jk}$ are the quadrature weights. Then the quasi linearized two point BVP (equivalent to Newton's method) can be written as shown below

$$\Delta\dot{x}_{ij} = T\frac{\partial\boldsymbol{f}}{\partial x}\left(x_{ij},\Omega\right)\Delta x_{ij} + \boldsymbol{f}\left(x_{ij},\Omega\right)\Delta T + T\frac{\partial\boldsymbol{f}}{\partial\Omega}\left(x_{ij},\Omega\right)\Delta\Omega + \boldsymbol{r}_{ij} \tag{36}$$

$$\boldsymbol{x}_{N+1} - \boldsymbol{x}_1 = 0 \tag{37}$$

where $\boldsymbol{r}_{ij} = T\boldsymbol{f}\left(x_{ij},\Omega\right) - \dot{\boldsymbol{x}}_{ij}$. Applying parameter condensation to eliminate the local unknowns x_{ij} at every time interval t_i we can write the derivatives $\boldsymbol{f}_i = \left[\,f_{i1} \quad f_{i2} \quad \cdots \quad f_{im}\,\right]^{\mathrm{T}}$ for the local unknowns as a function of the global unknowns $\boldsymbol{x}_i$. Substituting (34) in (35) yields

$$\boldsymbol{f}_i = \boldsymbol{f}\left(x_i + h_i\sum_{l=1}^{m} a_{jl}\,f_{il}\right) = T\frac{\partial\boldsymbol{f}}{\partial x}\left(x_{ij},\Omega\right)\Delta x_{ij} + T\frac{\partial\boldsymbol{f}}{\partial x}\left(x_{ij},\Omega\right)h_i\sum_{l=1}^{m} a_{jl}\,f_{il} + \boldsymbol{f}\left(x_{ij},\Omega\right)\Delta T + T\frac{\partial\boldsymbol{f}}{\partial\Omega}\left(x_{ij},\Omega\right)\Delta\Omega + \boldsymbol{r}_{ij} \tag{38}$$

The above can be rewritten as

$$\boldsymbol{f}_i = \mathbf{W}_i^{-1}\mathbf{V}_i\Delta x_i + \mathbf{W}_i^{-1}\mathbf{U}_i\Delta T + \mathbf{W}_i^{-1}\mathbf{S}\Delta\Omega + \mathbf{W}_i^{-1}\mathbf{r}_i \tag{39}$$

where

$$\mathbf{W}_i = \mathbf{I} - h_i\begin{bmatrix} a_{11}T\frac{\partial\boldsymbol{f}}{\partial x}\left(\boldsymbol{x}_{i1},\Omega\right) & \cdots & a_{1m}T\frac{\partial\boldsymbol{f}}{\partial x}\left(\boldsymbol{x}_{i1},\Omega\right) \\ \vdots & \ddots & \vdots \\ a_{1m}T\frac{\partial\boldsymbol{f}}{\partial x}\left(\boldsymbol{x}_{im},\Omega\right) & \cdots & a_{mm}T\frac{\partial\boldsymbol{f}}{\partial x}\left(\boldsymbol{x}_{ik},\Omega\right) \end{bmatrix} \tag{40}$$

$$\mathbf{V}_i=\begin{bmatrix} T\dfrac{\partial \boldsymbol{f}}{\partial x}\left(\boldsymbol{x}_{i1},\Omega\right) \\ \vdots \\ T\dfrac{\partial \boldsymbol{f}}{\partial x}\left(\boldsymbol{x}_{im},\Omega\right) \end{bmatrix},\ \mathbf{S}_i=\begin{bmatrix} T\dfrac{\partial \boldsymbol{f}}{\partial \Omega}\left(\boldsymbol{x}_{i1},\Omega\right) \\ \vdots \\ T\dfrac{\partial \boldsymbol{f}}{\partial \Omega}\left(\boldsymbol{x}_{im},\Omega\right) \end{bmatrix},\ \boldsymbol{r}_i=\begin{bmatrix} T\boldsymbol{f}\left(\boldsymbol{x}_{i1},\Omega\right)-\boldsymbol{f}_{i1} \\ \vdots \\ T\boldsymbol{f}\left(\boldsymbol{x}_{i1},\Omega\right)-\boldsymbol{f}_{im} \end{bmatrix} \tag{41}$$

Substituting (39) to (35) yields a set of $n\times N$ linear equations

$$\Delta\boldsymbol{x}_{i+1}=\Delta\boldsymbol{x}+h_i\sum_{l=1}^{m}\beta_l\boldsymbol{f}_{il}=\Delta\boldsymbol{x}+h_i\left[\beta_1\mathbf{I}\quad\cdots\quad\beta_m\mathbf{I}\right]\left[\mathbf{W}_i^{-1}\mathbf{V}_i\Delta\boldsymbol{x}_i+\mathbf{W}_i^{-1}\mathbf{U}_i\Delta T+\mathbf{W}_i^{-1}\mathbf{S}\Delta\Omega+\mathbf{W}_i^{-1}\boldsymbol{r}_i\right] \tag{42}$$

$$\Delta\boldsymbol{x}_{i+1}=\boldsymbol{\Gamma}_i\Delta\boldsymbol{x}_i+\boldsymbol{\Lambda}_i\Delta T+\boldsymbol{\Sigma}_i\Delta\Omega+\boldsymbol{r}_i \tag{43}$$

where

$$\begin{aligned} &\mathbf{D}=\left[\beta_1\mathbf{I}\quad\cdots\quad\beta_m\mathbf{I}\right],\qquad \boldsymbol{\Gamma}_i=\mathbf{I}+h_i\mathbf{D}\mathbf{W}_i^{-1}\mathbf{V}_i, \\ &\boldsymbol{\Lambda}_i=h_i\mathbf{D}\mathbf{W}_i^{-1}\mathbf{U}_i,\quad \boldsymbol{\Sigma}_i=h_i\mathbf{D}\mathbf{W}_i^{-1}\mathbf{S}_i,\quad \boldsymbol{r}_i=h_i\mathbf{D}\mathbf{W}_i^{-1}\boldsymbol{q}_i \end{aligned} \tag{44}$$

The linear algebraic system for the combined collocation-pseudo arc length continuation method is finally expressed in Eq. (45).

$$\begin{bmatrix} -\boldsymbol{\Gamma}_1 & \mathbf{I} & 0 & \dots & 0 & -\boldsymbol{\Lambda}_1 & -\boldsymbol{\Sigma}_1 \\ 0 & -\boldsymbol{\Gamma}_2 & \mathbf{I} & 0 & 0 & -\boldsymbol{\Lambda}_2 & -\boldsymbol{\Sigma}_2 \\ \vdots & \vdots & \ddots & \ddots & \vdots & \vdots & \vdots \\ 0 & 0 & \dots & -\boldsymbol{\Gamma}_N & \mathbf{I} & -\boldsymbol{\Lambda}_N & -\boldsymbol{\Sigma}_N \\ \mathbf{I} & 0 & 0 & \dots & -\mathbf{I} & 0 & 0 \\ h_1\dot{x}_1 & h_2\dot{x}_2 & \dots & h_N\dot{x}_N & 0 & 0 & 0 \\ x_1^{0'} & x_2^{0'} & \dots & x_N^{0'} & 0 & T^{0'} & \Omega^{0'} \end{bmatrix}\begin{Bmatrix} \Delta\boldsymbol{x}_1 \\ \Delta\boldsymbol{x}_2 \\ \vdots \\ \Delta\boldsymbol{x}_N \\ \Delta\boldsymbol{x}_{N+1} \\ \Delta T \\ \Delta\Omega \end{Bmatrix}=\begin{Bmatrix} \boldsymbol{r}_1 \\ \boldsymbol{r}_2 \\ \vdots \\ \boldsymbol{r}_N \\ \boldsymbol{x}_{N+1}-\boldsymbol{x}_1 \\ \sum_{i=1}^{N}\sum_{j=1}^{m}a_{ij}\left\langle \boldsymbol{x}_{ij},\dot{\boldsymbol{x}}_{ij}^{0}\right\rangle \\ \sum_{i=1}^{N}\sum_{j=1}^{m}a_{ij}\left(\boldsymbol{x}_{ij}-\dot{\boldsymbol{x}}_{ij}^{0}\right)\boldsymbol{x}_{ij}'+\left(T-T_0\right)T'+\left(\Omega-\Omega_0\right)\Omega_0'-\Delta s \end{Bmatrix} \tag{45}$$

where a_{ij} are the quadrature weights for the time intervals $\left[t_{i-1}\quad t_i\right]$.

The solution of the linear system can be achieved by various methods. Iterative methods are applied in this work. Floquet multipliers are evaluated as the eigenvalues of the matrix $\boldsymbol{\Gamma}_1\cdot\boldsymbol{\Gamma}_2\cdots\boldsymbol{\Gamma}_N$ when the iterative solution of the $n\times N$ system is achieved (right hand side less than a maximum). Calculating the Floquet multipliers in this way severely reduces the evaluation time compared to other methods (e.g. shooting method). The normal form coefficient is calculated with different method for the different type of bifurcation occurring. For more detailed information, the reader may refer to [84,85,91].

3.3. Poincaré Map

Poincaré map characterizing the intersection of a periodic orbit in the state space of a continuous dynamical systems with a lower-dimensional, and transverse to the flow, subspace called the Poincaré section. The Poincaré map produces a discrete dynamical system with a state space one dimension lower than the original continuous dynamical system. The dynamics on the Poincaré map preserves many of the periodic, quasi-periodic and chaotic orbits of the original system, and due to its dimensionality reduced form, it is often simpler to analyze than the original system.[92]

[91] Gavalas I., Chasalevris A., (2022), "Nonlinear Dynamics of Turbine Generator Shaft Trains: evaluation of bifurcation sets applying numerical continuation", ASME Journal of Engineering for Gas Turbine and Power. Accepted for publication
[92] H. Poincaré, (1899), "Les Methodes Nouvelles de la Méchanique Céleste", Gauthier-Villars, Paris.

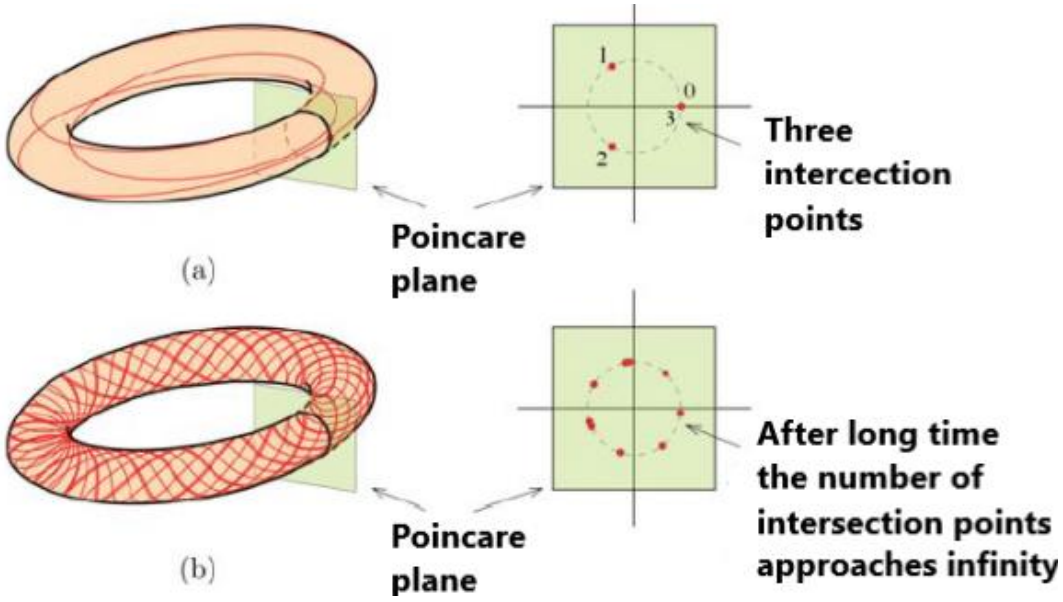

Fig. 1.2.1: Example for (a) periodic and (b) quasi-periodic state [93]

Poincaré maps provide a timescale separation by producing snapshots of the dynamics on the sampling scale of the map period. The Poincaré Map is produced by placing a plane normal to the path of the orbits and collect the points of intersection each time the orbit crosses the plane. The resulting discrete map of discrete points may be used to analyze the dynamics to great effect. The Poincaré maps that are depicted in this project, consider the last 100 periods of the response evaluated for 500 periods applying time intergration.[94]

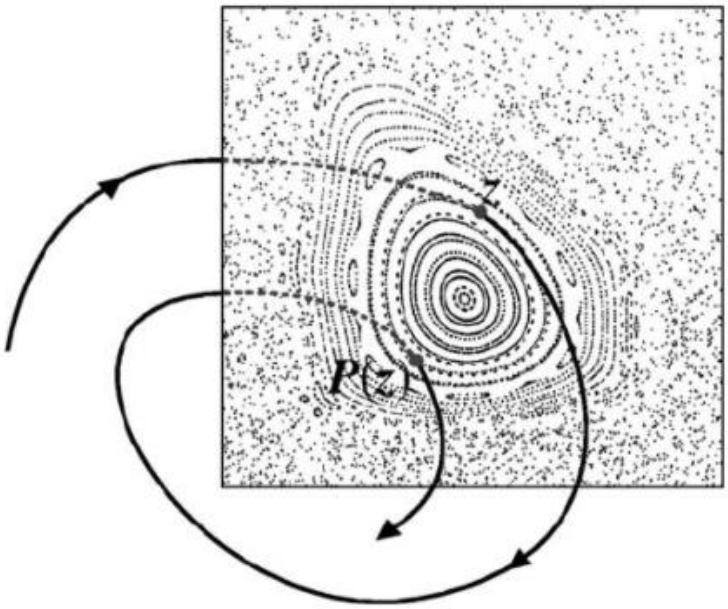

Fig. 1.2.2: Quasi-periodic and chaotic orbits [88]

In fig.1.2.2, the point "z" is mapped to P(z) by following the trajectory's next intersection of the plane. The closed circles represent quasi-periodic orbits on tori within the islands of stable orbits.

[93] P. Stumpf, Z. Sütő, I. Nagy, (2011), "Research in Nonlinear Dynamics Triggered by R&D Experiences", Conference: AACS'11, At: Budapest, Hungary

[94] Martin W. Lo, (2002), "The InterPlanetary Superhighway and the Origins Program", NASA, Conference: Aerospace Conference Proceedings, IEEEVolume: 7

The sea of dots are the chaotic orbits. Such patterns are difficult if not impossible to detect by observing the orbits themselves. [88]

3.4. Fast Fourier Transform

The "Fast Fourier Transform" (FFT) is one of the most useful tools and is widely used in the signal processing. It converts a signal into individual spectral components and thereby provides frequency information about the signal. FFTs are used for fault analysis, quality control, and condition monitoring of machines or systems.

The FFT is an optimized algorithm for the implementation of the "Discrete Fourier Transformation" (DFT). A signal is sampled over a period of time and divided into its frequency components. These components are single sinusoidal oscillations at distinct frequencies each with their own amplitude and phase.

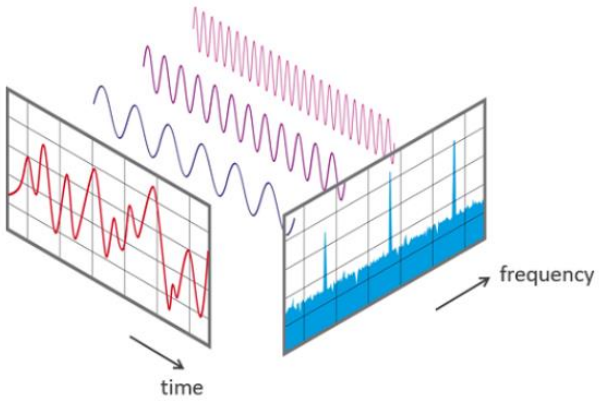

Fig. 3.4.1 View of a signal in the time and frequency domain; [taken from nti-audio.com]

The FFT operates by decomposing an N point time domain signal into N time domain signals each composed of a single point. The second step is to calculate the N frequency spectra corresponding to these N time domain signals. Lastly, the N spectra are synthesized into a single frequency spectrum. [95]

There are Log_2N stages required in this decomposition. The decomposition is nothing more than a reordering of the samples in the signal. The FFT time domain decomposition is usually carried out by a bit reversal sorting algorithm. This involves rearranging the order of the N time domain samples by counting in binary with the bits flipped left-for-right. The next step in the FFT algorithm is to find the frequency spectra of the 1-point time domain signals. The frequency spectrum of a 1-point signal is equal to itself. This means that nothing is required to do this step. Although there is no work involved, it's very important to remember that each of the 1-point signals is now a frequency spectrum, and not a time domain signal. The last step in the FFT is to combine the N frequency spectra in the exact reverse order that the time domain decomposition took place. [89]

In fig.1.4.2, the frequency domain synthesis requires three loops. The outer loop runs through the Log_2N stages. The middle loop moves through each of the individual frequency spectra in the stage being worked on. The innermost loop uses the butterfly to calculate the points in each frequency spectra. The butterfly is the basic computational element of the FFT, transforming two complex points into two other complex points. The overhead boxes determine the beginning and ending indexes for the loops, as well as calculating the sinusoids needed in the butterflies.[89]

[95] Steven W. Smith, Ph.D., (1997), "The Scientist and Engineer's Guide to Digital Signal Processing", Chapter 12: The Fast Fourier Transform

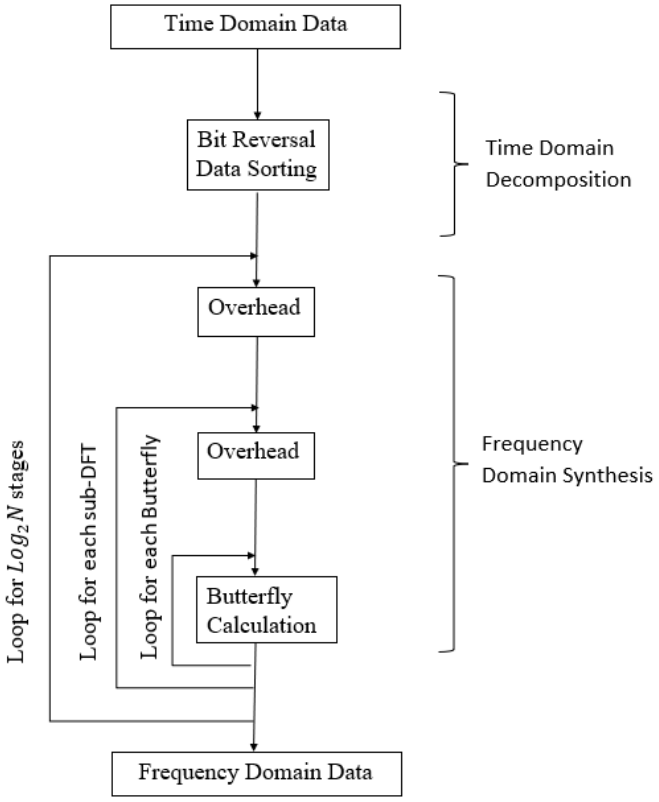

Fig. 3.4.2: Flow diagram of the FFT [11]

3.5. Short Time Fourier Transform

The STFT, also called the windowed Fourier transform or the sliding Fourier transform, partitions the time-domain input signal into several disjointed or overlapped blocks by multiplying the signal with a window function and then applies the discrete Fourier transform to each block. Window functions, also called sliding windows, are functions in which the amplitude tapers gradually and smoothly toward zero at the edges. Because each block occupies different time periods, the resulting STFT indicates the spectral content of the signal at each corresponding time period. When you move the sliding window, you obtain the spectral content of the signal over different time intervals. Therefore, the STFT is a function of time and frequency that indicates how the spectral content of a signal evolves over time. A complex-valued, 2-D array called the STFT coefficients stores the results of windowed Fourier transforms. The magnitudes of the STFT coefficients form a magnitude time-frequency spectrum, and the phases of the STFT coefficients form a phase time-frequency spectrum. The STFT is one of the most straightforward approaches for performing time-frequency analysis. The STFT is computationally efficient because it uses the fast Fourier transform (FFT).[96]

Several parameters must be chosen:

- Block length
- The type of window.
- Amount of overlap between blocks.

[96] LabVIEW 2010 Advanced Signal Processing Toolkit Help, (2010), "Short-Time Fourier Transform"

The STFT workflow for time-frequency distribution is mainly described as follows [91]:

Step 1: Extract samples weighted by a window function centered at a time ti.

Step 2: Compute the Fourier transform of the samples.

Step 3: Shift the window and repeat steps 1–2 until the end of the input waveform.

The window length controls the time and frequency resolution of the STFT. Using a short window length in the computation of STFT yields high time resolution and low frequency resolution whereas a longer window length increases the frequency resolution and decreases the time resolution. This explains the absence of temporal information on the Fourier transform computed over the entire length of the input waveform (amplitude spectrum). Because of the fixed window length, the STFT can only achieve uniform resolution in time and frequency. This drawback limits the ability of STFT to process signals with inconsistent dominant frequencies [97].

The best window length depends on the characteristics of the signal you want to analyze. The window length should be small enough so that the windowed signal block is essentially stationary over the window interval and large enough so that the Fourier transform of the windowed signal block provides a reasonable frequency resolution. If the spectral content of the signal evolves over time slowly, which does not require a fine time resolution, set the window length large. If the spectral content of the signal changes relatively quickly, which requires a fine time resolution, set the window length small [90]. The size of the window that we used in this project is $w = 2^{12}$ and the chosen window is Hamming.

The step size of the sliding window determines if overlap exists. If the step size is smaller than the window length, overlap exists. If the step size is greater than the window length, no overlap exists. Overlap of the sliding window makes the STFT smoother along the time axis. However, overlap requires more computation time and memory. If the signal length is large and the spectral content evolves slowly, it is not necessary to overlap the sliding window. If the signal length is small, overlap the sliding window to obtain a smoother STFT [90]. For making our STFT diagrams, we used overlap. The number of the overlap points in adjoining sections arises from the nearest integer of the following math operation $w - w/10$.

3.6. Design Optimization

Patternsearch [98] finds a sequence of points, $x_0, x_1, x_2, \ldots,$ that approach an optimal point. The value of the objective function either decreases or remains the same from each point in the sequence to the next.

The pattern search begins at the initial point x_0 that you provide.

Iteration 1

At the first iteration, the mesh size is 1 and the Generalized pattern search (GPS) algorithm adds the pattern vectors to the initial point x_0 to compute the following mesh points:

$$[1,0] + x_0 \qquad [0,1] + x_0 \qquad [-1,0] + x_0 \qquad [0,-1] + x_0$$

[97] Jubran Akram, (2020), "Understanding Downhole Microseismic Data Analysis", Springer

[98] The MathWorks, Inc., "How Pattern Search Polling Works", https://www.mathworks.com/help/gads/how-pattern-search-polling-works.html

The algorithm computes the objective function at the mesh points in the order shown above. The algorithm polls the mesh points by computing their objective function values until it finds one whose value is smaller the value at x_0. If it finds that value then, the poll at iteration 1 is successful and the algorithm sets the next point in the sequence equal to x_1.

Iteration 2

After a successful poll, the algorithm multiplies the current mesh size by 2. Because the initial mesh size is 1, at the second iteration the mesh size is 2. The mesh at iteration 2 contains the following points:

$$2\cdot[1,0]+x_1 \qquad 2\cdot[0,1]+x_1 \qquad 2\cdot[-1,0]+x_1 \qquad 2\cdot[0,-1]+x_1$$

The algorithm polls the mesh points until finds one whose value is smaller than the value at x_1. If it finds that value then, the poll at iteration 2 is again successful. The algorithm sets the second point in the sequence equal to x_2.

Because the poll is successful, the algorithm multiplies the current mesh size by 2 to get a mesh size of 4 at the third iteration.

An Unsuccessful Poll

By the fourth iteration, the current point is x_3 and the mesh size is 8, so the mesh consists of the points:

$$8\cdot[1,0]+x_3 \qquad 8\cdot[0,1]+x_3 \qquad 8\cdot[-1,0]+x_3 \qquad 8\cdot[0,-1]+x_3$$

At this iteration, none of the mesh points has a smaller objective function value than the value at x3, so the poll is unsuccessful. In this case, the algorithm does not change the current point at the next iteration. That is $x_4 = x_3$.

At the next iteration, the algorithm multiplies the current mesh size by 0.5, so that the mesh size at the next iteration is 4. The algorithm then polls with a smaller mesh size.

Boundaries

Patternsearch modifies poll points to be feasible at every iteration, meaning to satisfy all bounds and linear constraints. In our project, the boundaries that we used to implement the optimization for the $\bar{\alpha}_f$ and the η **:**

$$5\cdot10^{-3} < \bar{\alpha}_f < 2$$

$$10^{-4} < \eta < 10$$

Stopping Conditions for the Pattern Search

The algorithm stops when any of the following conditions occurs:

- The mesh size is less than the *MeshTolerance* option which was set at 10^{-6}
- The number of iterations performed by the algorithm reaches the value of the *MaxIterations* option which was set at 300.

- The total number of objective function evaluations performed by the algorithm reaches the value of the *MaxFunctionEvaluations* option.
- The time, in seconds, the algorithm runs until it reaches the value of the *MaxTime* option. In our optimization that was free.
- After a successful poll, the distance between the point found in the previous two iterations and the mesh size are both less than the *StepTolerance* option.
- After a successful poll, the change in the objective function in the previous two iterations is less than the *FunctionTolerance* option and the mesh size is less than the *StepTolerance* option.

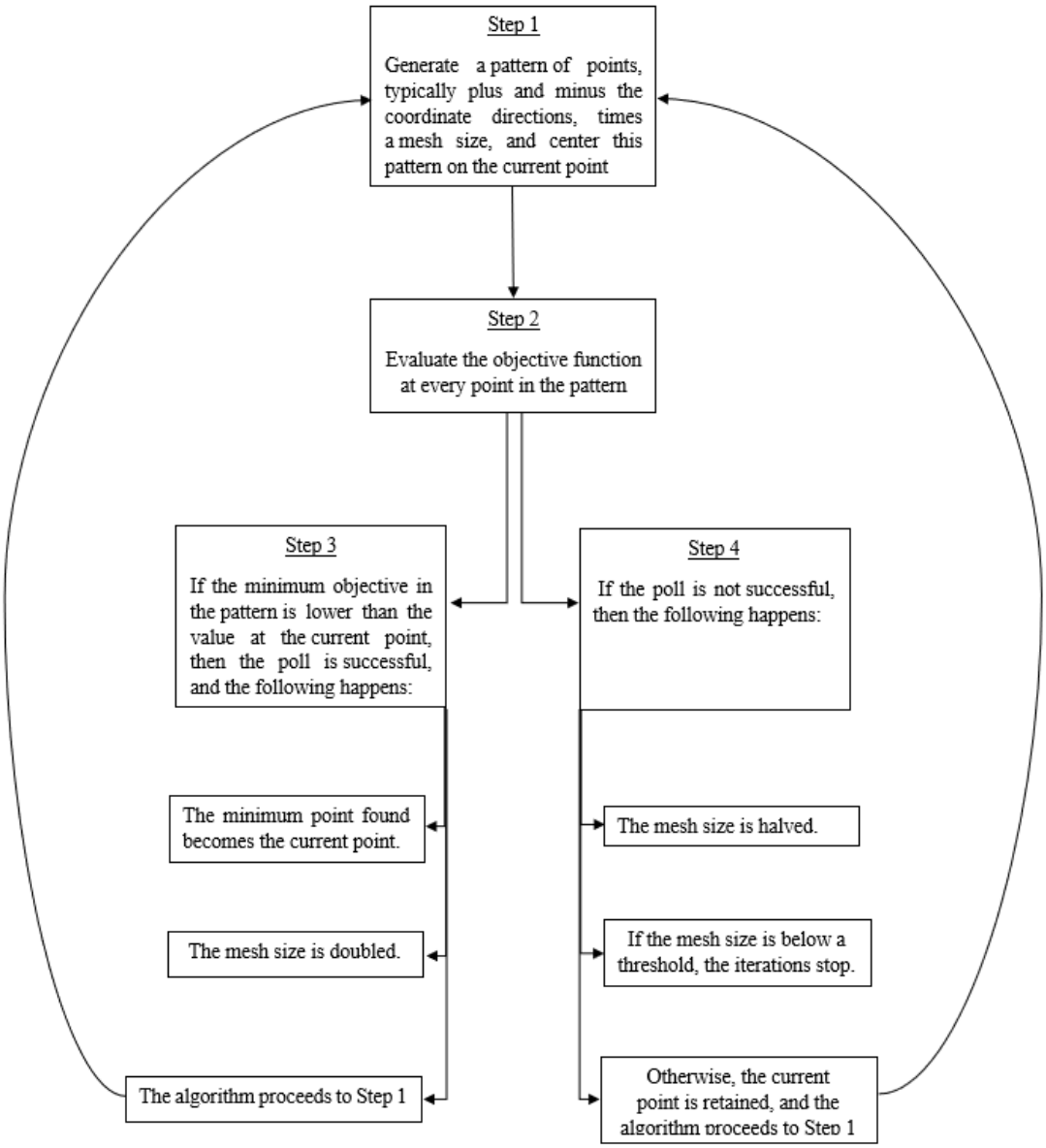

Fig. 1.6.1: Flow diagram of the Patternsearch

4. RESULTS AND DISCUSSION

4.1. Static performance of the gas bearing

The nonlinear feature of gas forces is presented in this Section. The vertical displacement of each journal (equal at both journals due to symmetry) when load $\bar{W}$ is applied vertically at each journal, further to the gravity load, is depicted in Fig. 4.1.1 for low, moderate, and high bump foil compliance, and for different design and operating conditions. In Fig. 4.1.2, the corresponding equilibrium locus of the journal inside the radial clearance is depicted for the various cases mentioned. One may notice that the nonlinear feature of the gas forces becomes strong or weak depending to the design configuration of the bearing and the respective operating speed $\bar{\Omega}$. The gas foil bearings configured for the results in Figs. 4.1.1 and 4.1.2 are of length to diameter ratio equal to 1, while the ratio of the radial clearance to the journal radius differs among the cases $R/c_r = 500, 750, 1000$ to produce different Sommerfeld number S. The dynamic viscosity μ of the gas equals to this of the ambient air at 20^oC, $\mu = 0.018\text{mPa}\cdot\text{s}$, and the ambient pressure is set at $p_0 = 100\text{kPa}$. Radial clearance follows $R/c_r = 500$ in the results produced at all next Sections while all other parameters are retained as defined hereby.

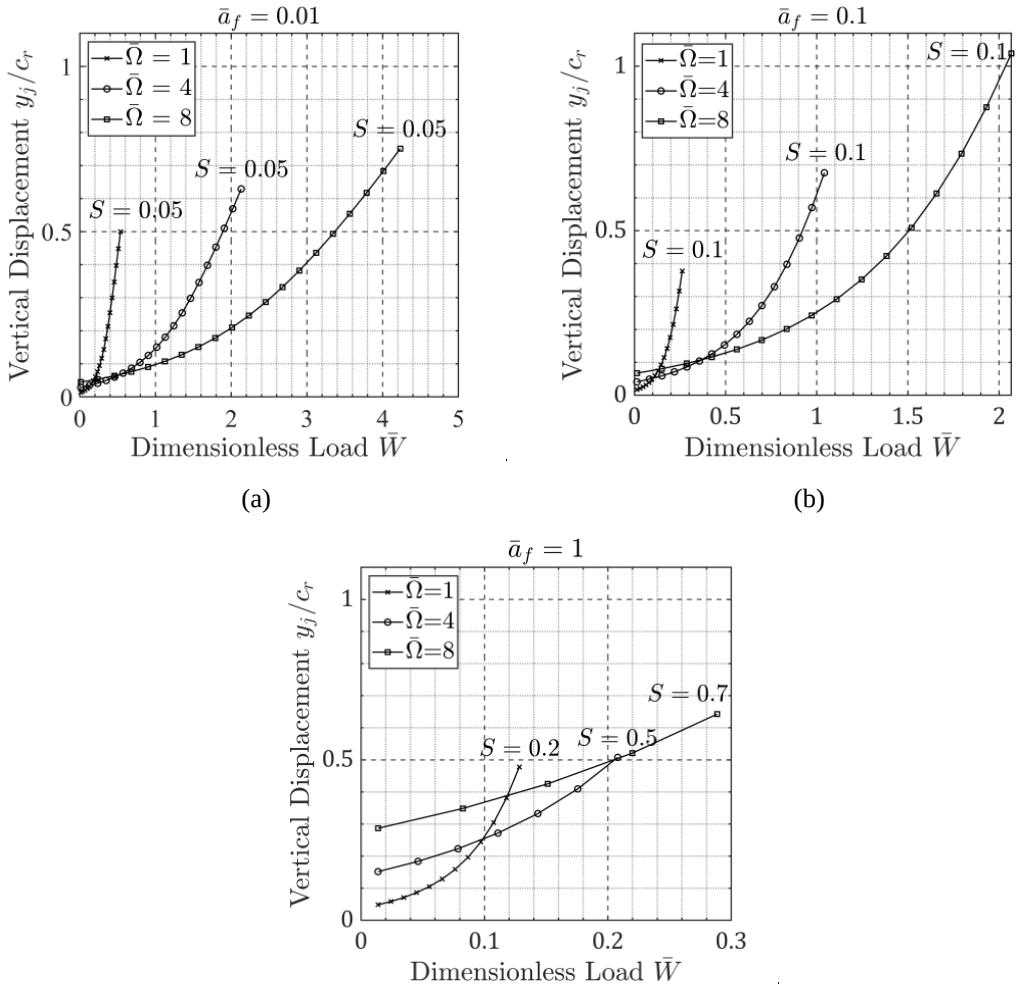

Fig. 2.1: Displacement $\bar{y}_j$ over load; (a) $\bar{\alpha}_f = 0.01$, (b) $\bar{\alpha}_f = 0.1$, (c) $\bar{\alpha}_f = 1$

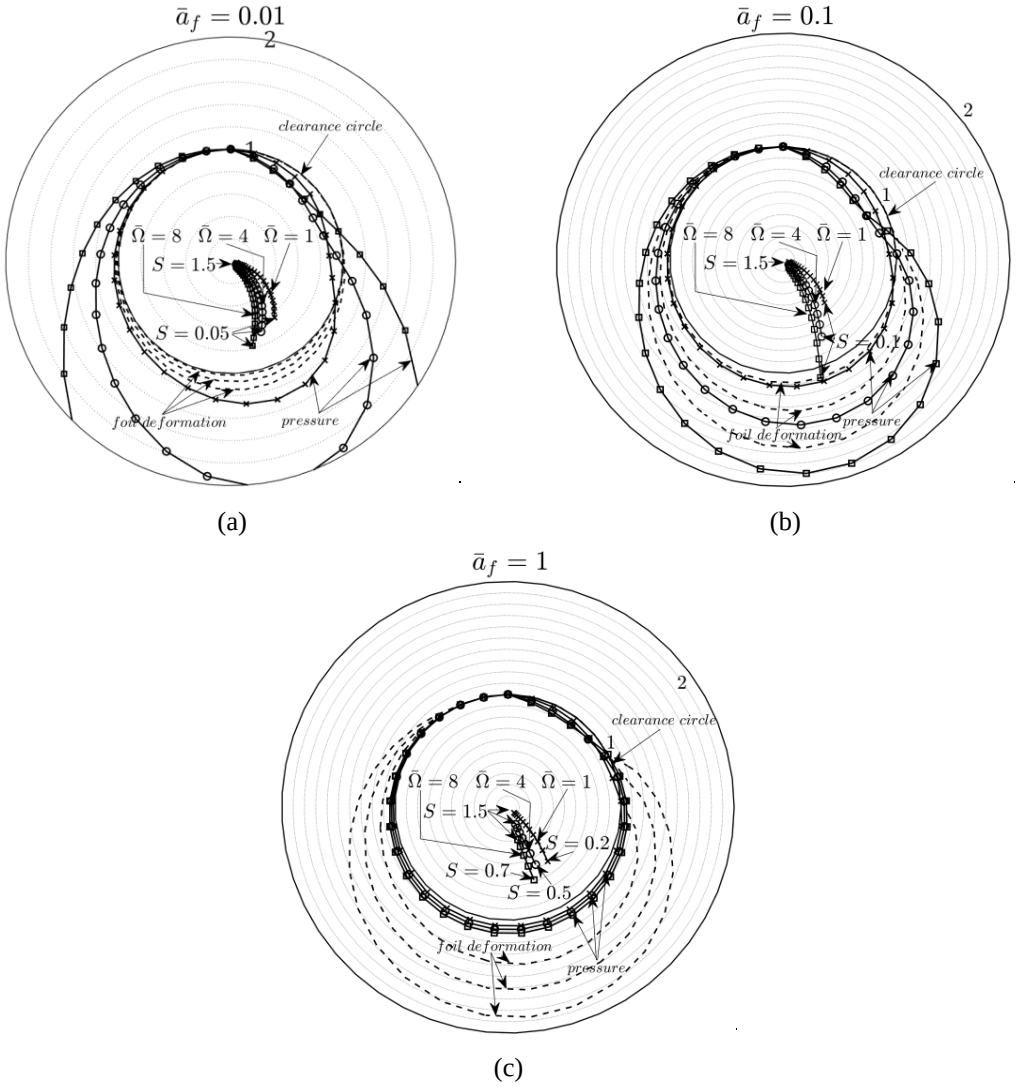

Fig. 2.2: Representation of journal's locus, foil deformation $\bar{\boldsymbol{q}}$ and pressure distribution $\bar{\boldsymbol{p}}$;
(a) $\bar{\alpha}_f = 0.01$, (b) $\bar{\alpha}_f = 0.1$, (c) $\bar{\alpha}_f = 1$

In these figures we use × for $\bar{\boldsymbol{\Omega}} = \mathbf{1}$, □ for $\bar{\boldsymbol{\Omega}} = \mathbf{4}$ and ○ for $\bar{\boldsymbol{\Omega}} = \mathbf{8}$. We also use the thick black line to denote the Clearance circle (**—** Clearance circle), the dashed line for the Foil deformation (--- Foil deformation) and the thin line for the pressure (— Pressure)

4.2. Quality of motion of the dynamic system

The dynamic system defined by Eq. (19) for autonomous and in Eq. (20) for non-autonomous version is investigated on its potential to develop a variety of bifurcation sets with respect to the key design parameters, namely rotor stiffness $\bar{k}_s$, foil compliance $\bar{a}_f$, foil loss factor η, and unbalance magnitude u. In this paper, the key design parameters are defined within specific intervals, composing the case studies which are presented in the following. The design parameters follow a variation of "low", "reference", and "high". This is interpreted to the rotor stiffness values $\bar{k}_s = 0.3,1,3$ (flexible to rigid rotor), foil compliance values $\bar{a}_f = 0.01, 0.1, 1$ (stiff to flexible foil), foil loss factor $\eta = 0.005, 0.05, 0.5$ (low to high foil damping), and unbalance magnitude $u(G1), u(G2.5), u(G6.3)$ (low to high unbalance). Therefore, a reference system is defined with the design parameters $\bar{k}_s = 1$, $\bar{a}_f = 0.1$, $\eta = 0.05$, and $u(G6.3)$.

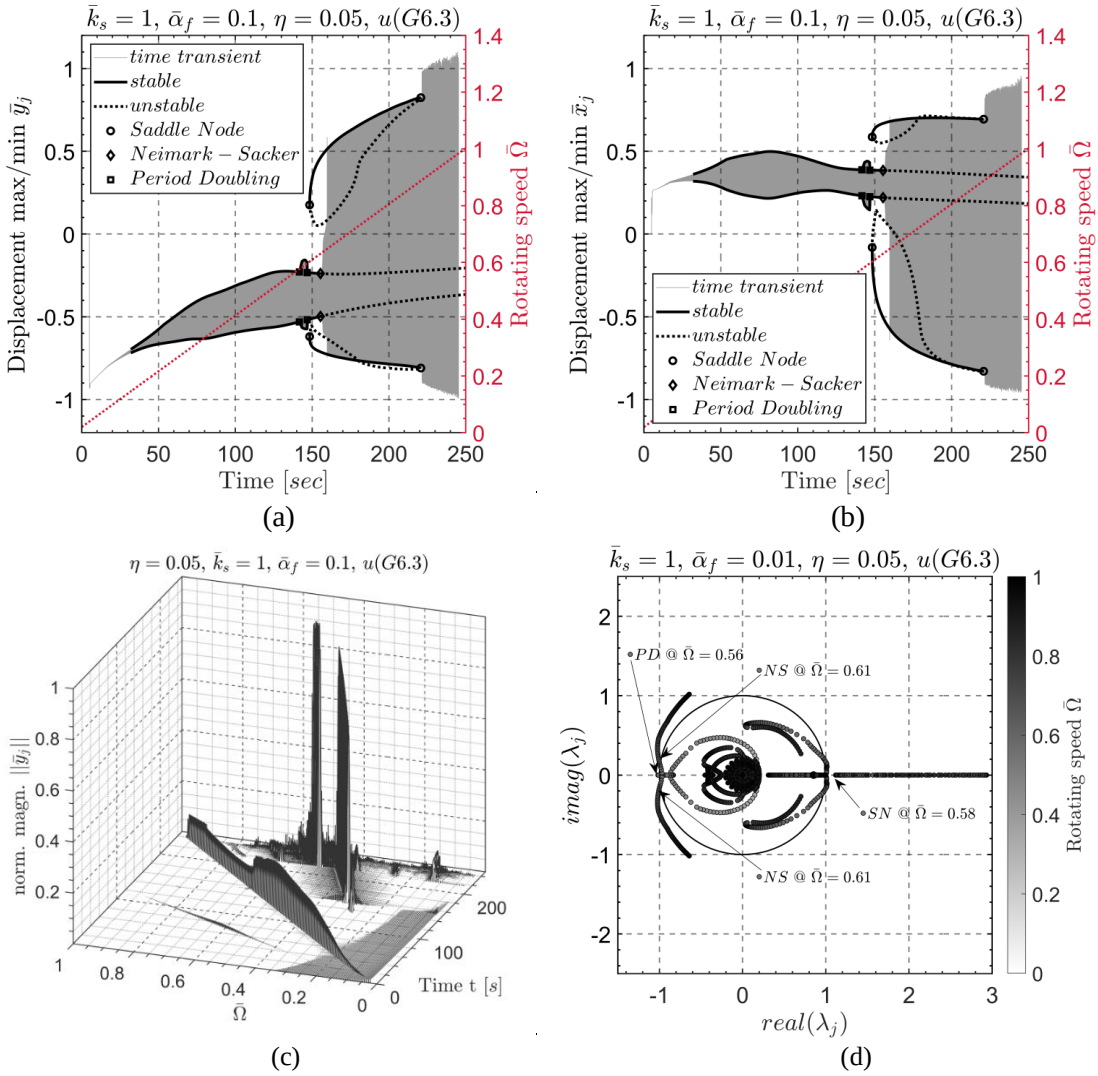

Fig. 4.2.1 Reference system: system of $\bar{k}_s = 1$, $\bar{\alpha}_f = 0.1$, $\eta = 0.05$, and $u(G6.3)$. Transient response and continuation of limit cycles during run-up in a) vertical direction, and b) horizontal direction. c) STFT of the response time history, c) Floquet multipliers of the corresponding limit cycles.

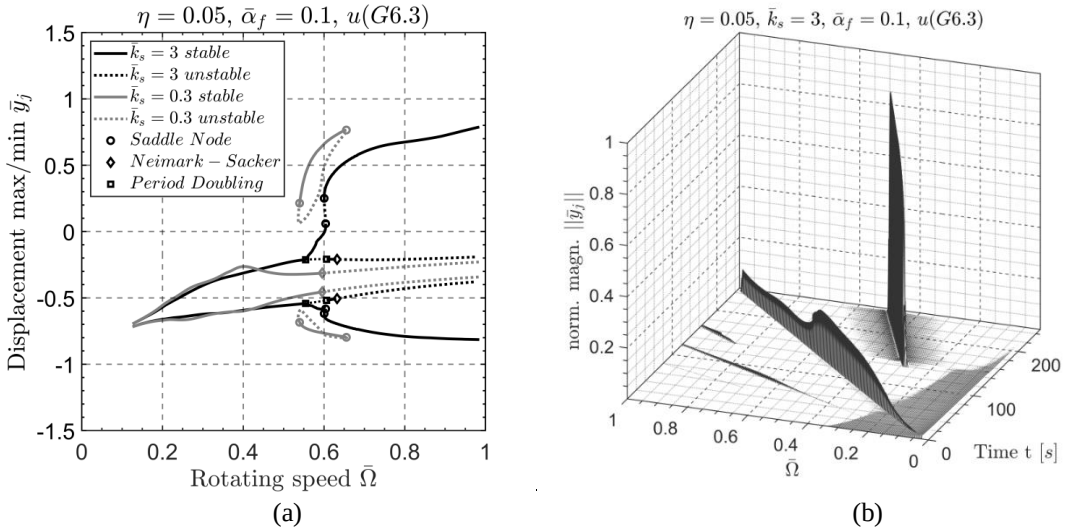

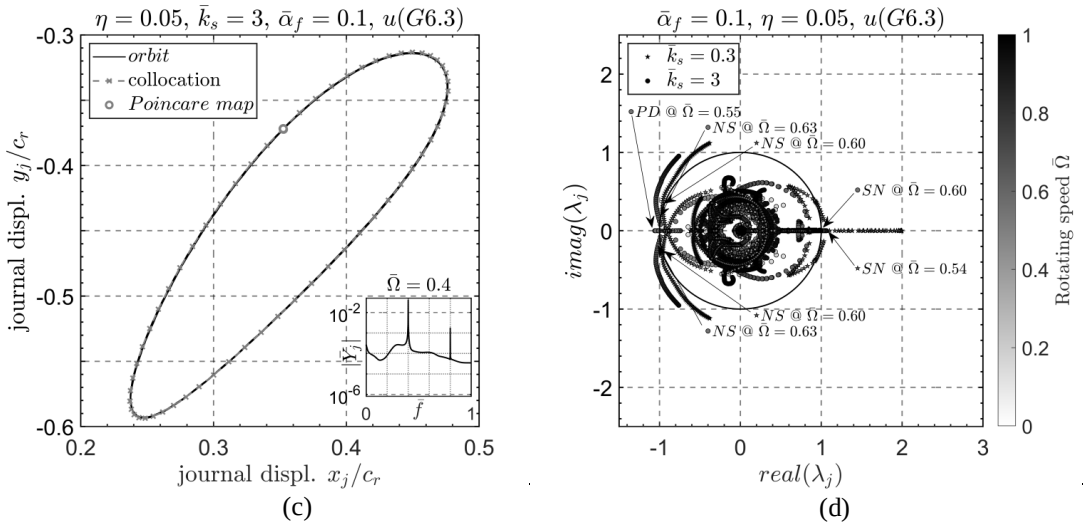

Fig. 4.2.2 System of $\bar{k}_s^-, \bar{k}_s^+$ $\bar{a}_f = 0.1, \eta = 0.05, u(G6.3)$. a) Continuation of limit cycles, b) STFT of the response time history $\bar{k}_s^+$, c) trajectory, Poincare map, and FFT at $\bar{\Omega} = 0.4$, d) Floquet multipliers of the corresponding limit cycles $\bar{k}_s^+$.

The time transient response of the reference system is evaluated applying time integration in Eq. (20) defined for variable rotating speed (run-up) and constant rotating acceleration. The ODE system is subjected to numerical continuation algorithm which evaluates limit cycles at the different rotating speeds (bifurcation parameter). In Fig. 4.2.1.a the time history of the journal motion in the vertical plane is presented together with the maximum and minimum limit cycle points at each rotating speed. It has to be clarified that the rotating speed is retained constant when limit cycles are evaluated, and the unbalance forces are applied with different formulas in the ODE system in the transient run-up and in the ODE system for constant rotating speed, see Eqs. (15a). Thus, slight discrepancies are noticed in the response of the two methods in Fig. 4.2.1.a. A reference bifurcation set is established in Fig. 4.2.1.a with PD, SN, and NS bifurcations to be presented. The frequency content of the time history obtained for the run-up is depicted in Fig. 4.2.1.b where time-frequency decomposition is applied (STFT). The journal trajectory at a selected rotating speed is depicted in Fig. 4.2.1.c together with the respective limit cycles evaluated with the collocation method. The transient response and the Poincaré map depicted also in Fig. 4.2.1.c consider the last 100 periods of the response evaluated for 500 periods applying time integration. The Floquet multipliers in Fig. 4.2.1.d provide information regarding the quality of bifurcations mentioned before at the respective speeds.

In general, periodic, quasi-periodic and chaotic motions are expected to be generated by the system studied in this paper. A drawback of the current continuation scheme programmed by the authors is that only periodic motions can be evaluated by the collocation method. The quasi-periodic motions can only be evaluated by time integration in this paper and depicted as transient response. For quasi-periodic limit cycles, the reader may consider the recent work in [99].

[99] Fiedler, R.: Numerical Analysis of Invariant Manifolds Characterized by Quasi-Periodic Oscillations of Nonlinear Systems. PhD Thesis, Kassel University Press, Germany (2021).

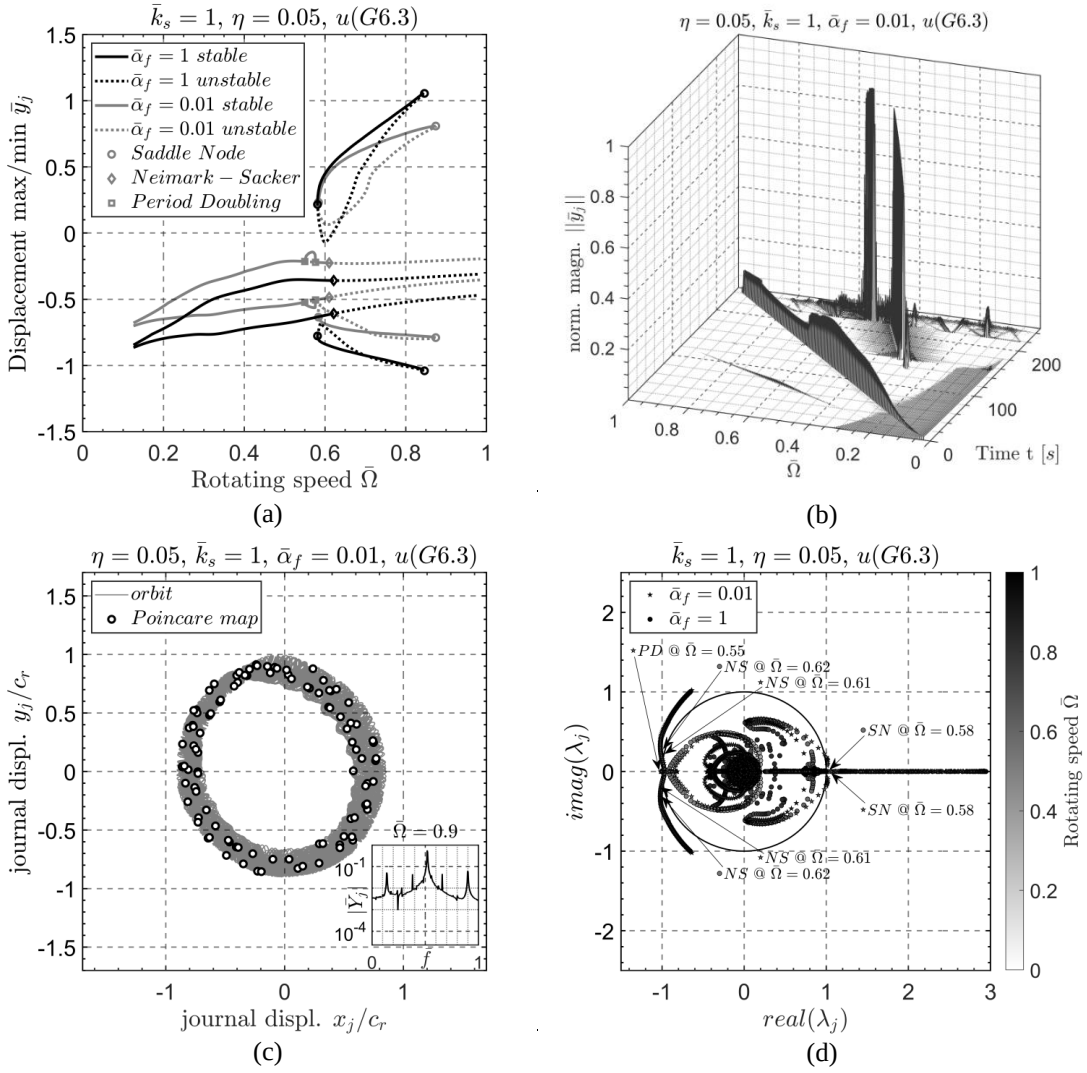

Fig. 4.2.3 System of $\bar{k}_s = 1, \bar{a}_f^-, \bar{a}_f^+,\ \eta = 0.05, u(G6.3)$. a) Continuation of limit cycles, b) STFT of the response time history for $\bar{a}_f^+$, c) trajectory, Poincare map, and FFT at $\bar{\Omega} = 0.9$, d) Floquet multipliers of the corresponding limit cycles for $\bar{a}_f^+$.

Further bifurcation sets for the respective design sets are presented in continue in order to study the system motion for the various combinations of design parameters and to reveal the types of motions and of bifurcations which may occur. These are defined considering one design parameter, changing each time, to the next higher and lower value of the respective design variable. Fig. 4.2.2 considers a system with changed rotor stiffness compared to the reference system, and therefore two cases are presented in Fig. 4.2.2.a and Fig. 4.2.2.d, for $\bar{k}_s^+ = 3$ (rigid rotor) and $\bar{k}_s^- = 0.3$ (flexible rotor). One may notice the different bifurcation sets compared to the reference case. Period doubling bifurcation is not noticed in this case.

In Fig. 4.2.3.a system with different foil compliance is considered, and therefore two cases are presented in Fig. 4.2.3.a and Fig. 4.2.3.d, for $\bar{a}_f^+ = 1$(flexible foil) and $\bar{a}_f^- = 0.01$(rigid foil). One may notice the different bifurcation sets compared to the reference case, and the previous case

(Fig. 4.2.2). The type of bifurcations are same to this at the reference case, but the speed in which they appear is different.

In Fig. 4.2.4 a system with different foil damping is considered, and two cases are presented in Fig. 4.2.4.a and Fig. 4.2.4.d, for $\eta^{+}=0.5$ (high foil damping) and $\eta^{-}=0.005$ (low foil damping). The influence of foil damping in the bifurcation set is not severe, compared to the reference design (Figs. 4.2.1).

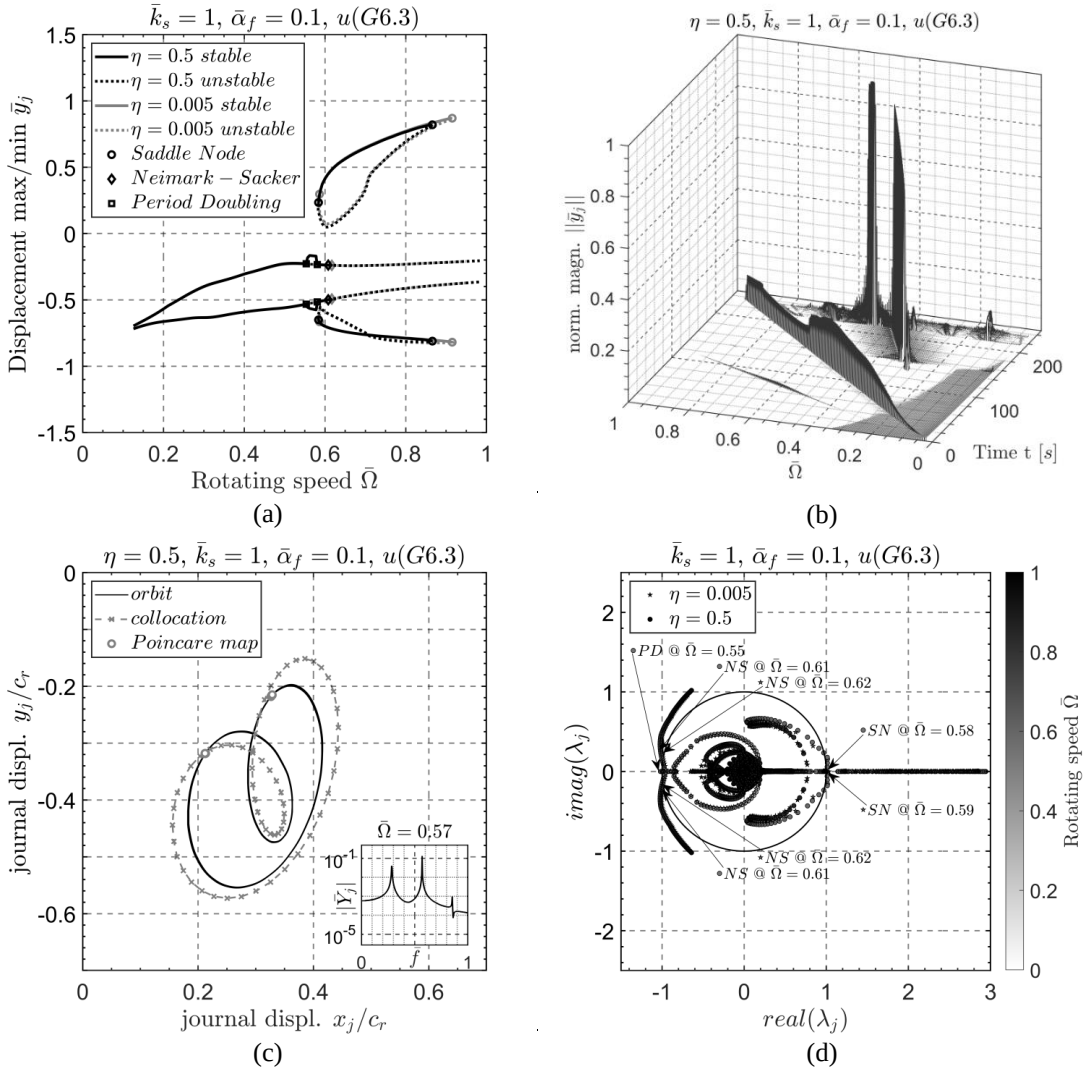

Fig. 4.2.4 System of $\bar{k}_s=1\ \ \bar{a}_f=0.1\ \eta^{-},\eta^{+},u(G6.3)$. a) Continuation of limit cycles, b) STFT of the response time history for η^{+}, c) trajectory, Poincare map, and FFT at $\bar{\Omega}=0.57$, d) Floquet multipliers of the corresponding limit cycles for η^{+}.

In Fig. 4.2.5 systems of different unbalance are considered, and three cases are presented in Fig. 10a, for $u(G0)$ (balanced rotor – autonomous system), $u(G1)$ (low unbalance), and $u(G2.5)$ (medium unbalance). It is worth noticing that the autonomous system of $u(G0)$ loses local stability of fixed point equilibria through an Andronov-Hopf bifurcation, at similar speed where the unbalanced systems lose local stability through secondary Hopf (Neimark-Sacker bifurcations). Further to that, in the unbalanced systems, the higher the unbalance is, the lower the speed of NS

bifurcations is. Stable limit cycles close to radial clearance occur with higher amplitude in the balanced system, than in the unbalanced systems. In the balanced system the limit cycles of amplitude close to radial clearance will lose stability through a NS bifurcation at high speeds.

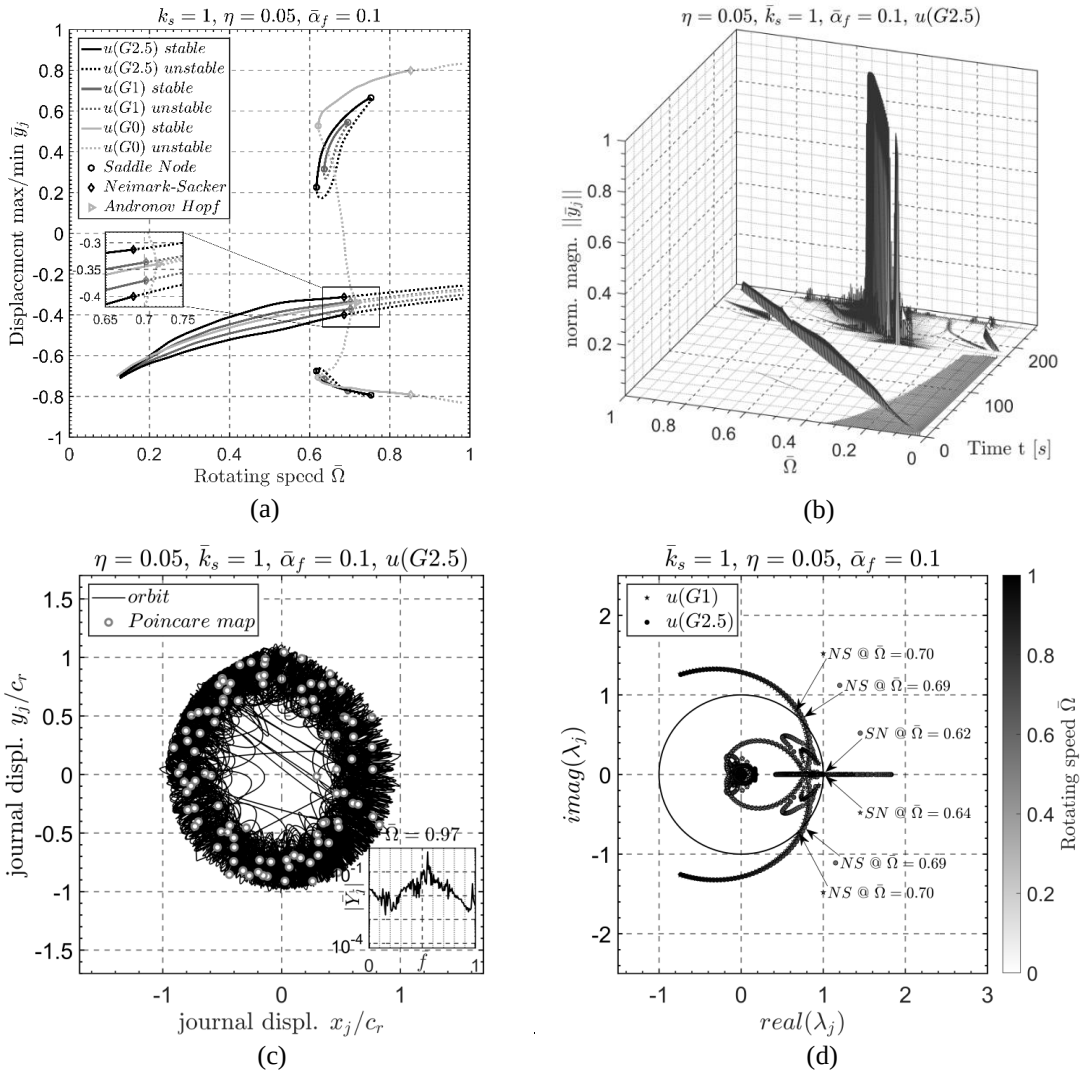

Fig. 4.2.5 System of $\bar{k}_s = 1, \bar{a}_f = 0.1, \eta = 0.05, u(G0), u(G1), u(G2.5)$. a) Continuation of limit cycles, b) STFT of the response time history for $u(G2.5)$, c) trajectory, Poincare map, and FFT at $\bar{\Omega} = 0.97$ for $u(G2.5)$, d) Floquet multipliers of the corresponding limit cycles for $u(G2.5)$.

In the figures above, Poincaré maps are constructed at selected speeds to depict the different quality of motions (periodicity), and the respective frequency content can be considered through the FFT and the STFT in each figure. At lower speeds, the system oscillates periodically with $1T$ period at all cases ($T = 2\pi/\Omega$ is the driving period hereby). This renders one point in Poincaré map, and additional harmonics of integer multiple in the FFT, see Fig. 4.2.2c. This status remains till a periodic doubling occurs at some cases, e.g. Fig. 4.2.4c, and the system oscillates with period $2T$ immediately after; this renders two points in Poincaré map. At the highest speeds investigated, only quasi-periodic or chaotic motions where evaluated, these through time integration. The respective quality and frequency content is depicted in Figs. 4.2.3c and 4.2.5c, where Poincaré map is constructed with several points without forming a shape. The frequency content at such speeds includes higher and lower harmonics of synchronous response without integer multiple.

4.3. Energy flow and optimization for bifurcation elimination

The energy flow among the components of the system is evaluated in this section for each of the limit cycle motions evaluated in the previous Section. Potential energy storage occurs in the stiffness elements in the system, these being the flexible rotor of lateral stiffness k_s, and the flexible bump foil consisting of N_x elements of stiffness k_f. Note that k_f expresses the stiffness coefficient per area. The gas film possesses also an unknown stiffness property and therefore potential energy is considered to be stored in the gas through the work of the conservative part of the gas forces. Kinetic energy storage occurs in the three masses of the system, these being the disc mass m_d and the two journal masses m_j; note that bump foil is considered massless and no inertia effects are considered in the gas flow inside the gas bearings. Dissipation of energy occurs in the gas film forces and in the bump foil damping elements of damping coefficient per area c_f. The system executes planar motions with the energy offered through the work of the unbalance forces. The unbalance force is a result of rotation, and a motor is supposed to retain the rotating speed constant, while the lateral vibrations are uncoupled to the energy offered by the motor.

In a closed trajectory (limit cycle) of the three rotor masses and the bump foil elements, the solution method offers all values of the state vector $\tilde{\tilde{\mathbf{s}}}$ while $\dot{\tilde{\tilde{\mathbf{s}}}}$ can be easily found by Eq. (21a). Let the time intervals during a limit cycle motion be N_t, defining N_t+1 discrete time points. The corresponding gas forces at each discrete time point are evaluated by the state vector $\tilde{\tilde{\mathbf{s}}}$ and its time derivative $\dot{\tilde{\tilde{\mathbf{s}}}}$ using Eq. (7), these being $F_{B,X}(i)$ and $F_{B,Y}(i)$, for $i=1,2,...N_t+1$. Similarly, the bump foil forces are evaluated in the radial direction as $F_{f,j}(i)$ for the j^{th} element of the N_x in total, see Fig. 2.1.2 and Fig. 2.1.3, as $F_{f,j}(i)=k_f q_j(i)+c_f \dot{q}_j(i)$, with $q_j, \dot{q}_j$ to be contained in the known $\tilde{\tilde{\mathbf{s}}}$ and $\dot{\tilde{\tilde{\mathbf{s}}}}$. The unbalance forces are defined as $F_{U,X}(i)$ and $F_{U,Y}(i)$ from Eq. (15a). The work of the bearing forces is evaluated in Eq. (46a), the work of the bump foil forces is evaluated in Eq. (46b), and the work of unbalance forces in evaluated in Eq. (46c).

$$W_B = 2\sum_{i=1}^{N_t}\left(F_{B,X}(i)\cdot\delta x_j(i)+F_{B,Y}(i)\cdot\delta y_j(i)\right)=W_{cb}+W_{kb} \tag{46a}$$

$$W_f = 2\sum_{i=1}^{N_t}\left(\sum_{j=1}^{N_x}F_{f,j}(i)\cdot\delta q_j(i)\right)=W_{cf}+\underbrace{W_{kf}}_{=0} \tag{46b}$$

$$W_{fu} = \sum_{i=1}^{N_t}\left(F_{U,X}(i)\cdot\delta x_d(i)+F_{U,Y}(i)\cdot\delta y_d(i)\right) \tag{46c}$$

In Eq. (46a) the portions W_{cb} and W_{kb} cannot be evaluated separately, but only as sum. However, it is expected that $W_{kb}\approx 0$ as this is the work of the conservative portion of the bearing forces in the closed trajectory. In Eq. (46b) W_{cf} is evaluated as $W_{cf}=W_f$ since it is found that $W_{kf}=0$ as it is the work of conservative forces in a closed trajectory. In a closed trajectory, the kinetic energy T_1 and T_2 of the system at the beginning and at the end of the trajectory respectively must equal the work of the non-conservative forces plus the work offered to the system. Therefore, Eq. (47) holds, with $T_1=T_2$ (periodic motion). [100]

[100] Meirovitch, L.: Methods of Analytical Dynamics. McGraw Hill, NY (1970)

$$T_2 - T_1 + W_{fu} = W_{cf} + W_{cb} \tag{47}$$

Eq. (47) renders W_{cb} as W_{fu} is known by Eq. (46c) and W_{cf} is known by Eq. (46b). The value of W_{cb} is also validated by Eq (46a). The work of the non-conservative forces W_{cb} and W_{cf} is depicted in Fig. 11 for some of the design sets of the previous Section, together with the work of the unbalance force W_{fu}.

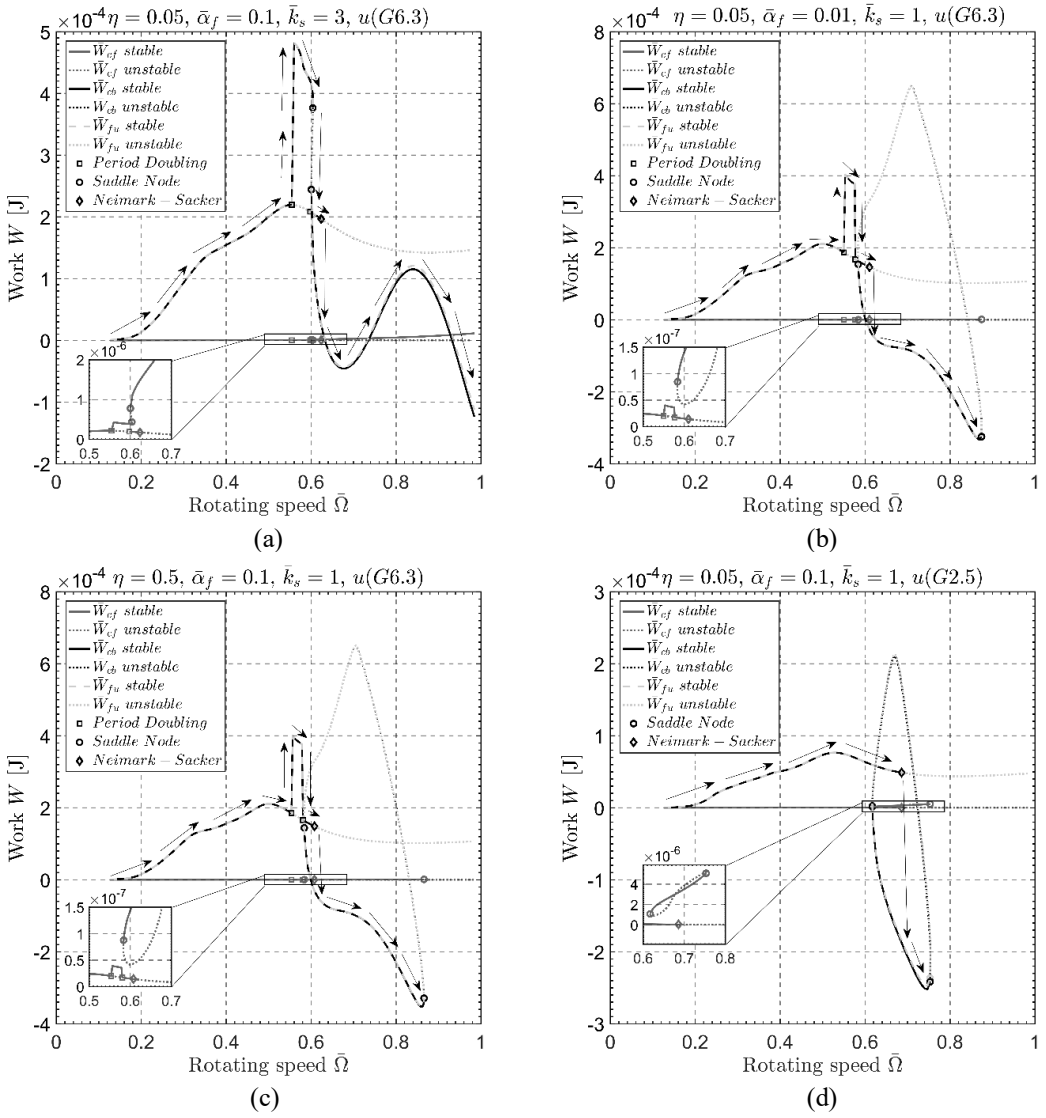

Fig. 4.3.1 Evaluation of energy flow at the respective limit cycles for a) $\bar{k}_s = 3$, $\bar{a}_f = 0.1$, $\eta = 0.05$, $u(G6.3)$, b) $\bar{k}_s = 1$, $\bar{a}_f = 0.01$, $\eta = 0.05$, $u(G6.3)$, c) $\bar{k}_s = 1$, $\bar{a}_f = 0.1$, $\eta = 0.5$, $u(G6.3)$, and d) $\bar{k}_s = 1$, $\bar{a}_f = 0.1$, $\eta = 0.05$, $u(G2.5)$.

In Figs. 4.3.1.a-d, both stable and unstable limit cycles are considered with the respective notation. At all cases, it is found that Neimark-Sacker bifurcations are triggered simultaneously to the reverse (from positive values to negative) of the dissipating work in the gas film W_{cb}, meaning that energy is not dissipated in the gas film (when $W_{cb} < 0$) and self-excitation is triggered. In Figs. 4.3.1.a-d, the arrows depict the path along which the solution is developed during the run-up.

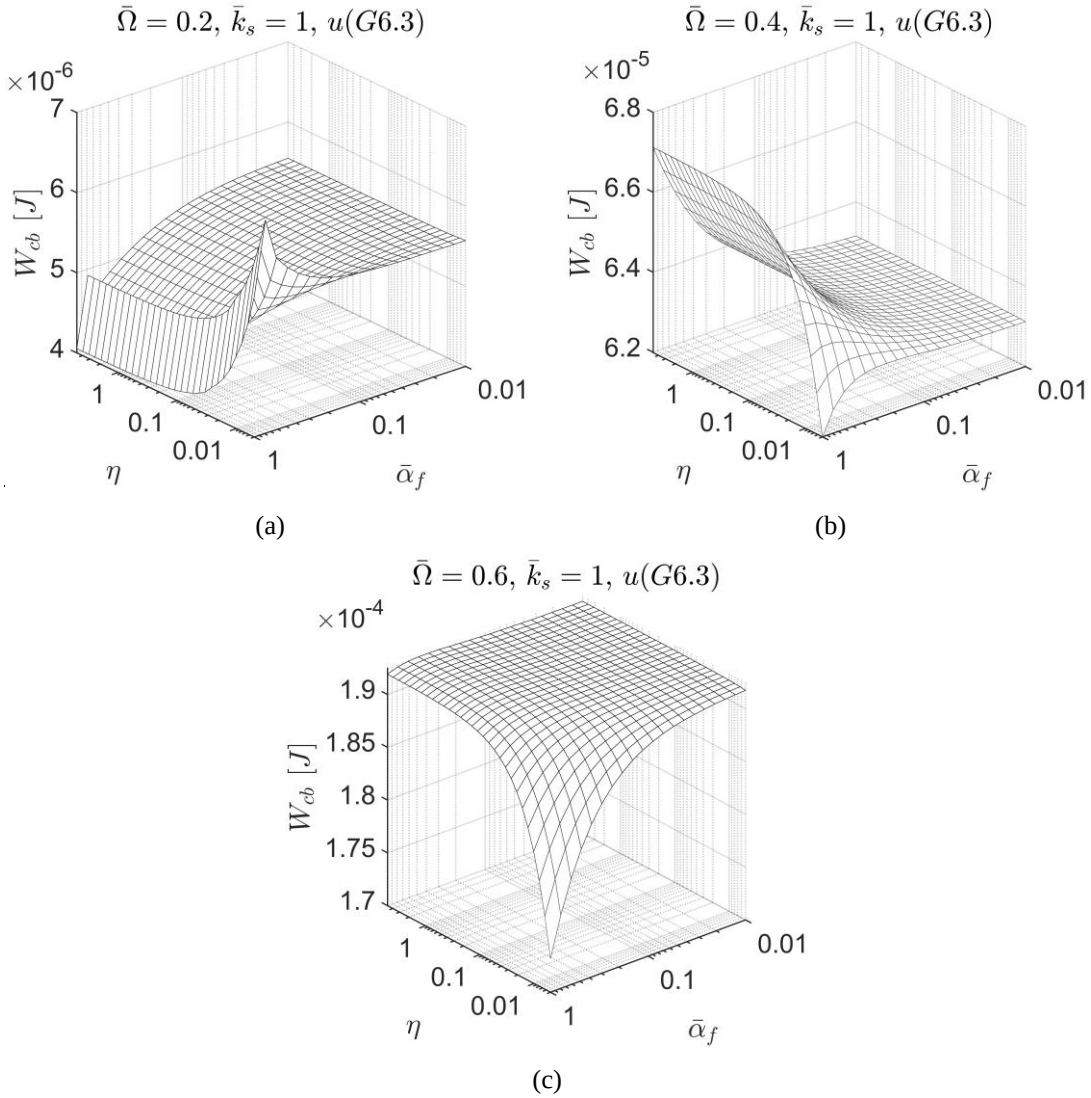

Fig. 4.3.2 Dissipated energy in the gas film in one limit cycle for various values of foil compliance $\bar{a}_f$ and foil loss factor η, at a) $\bar{\Omega} = 0.2$, b) $\bar{\Omega} = 0.4$, c) $\bar{\Omega} = 0.6$.

The work W_{cb} is plotted in Fig. 4.3.2 for the respective cases of bump foil design and for the reference system regarding rotor stiffness and unbalance magnitude. Fig. 4.3.2 depicts the sensitivity of W_{cb} in regards to foil properties. It is worth noticing that at the lowest rotating speed $\bar{\Omega} = 0.2$ the dissipated energy has a maximum for specific value of foil compliance $\bar{a}_f \approx 1$ and for low values of loss factor η. This is not the case at the higher speed $\bar{\Omega} = 0.4$, where W_{cb} has a maximum still for $\bar{a}_f \approx 1$, but for high values of loss factor η, see Fig. 4.3.2b. Increasing the speed further at $\bar{\Omega} = 0.6$, W_{cb} has the highest values for several pairs of $\bar{a}_f$ and η, the former receiving the lower values, and the latter at higher values, see Fig. 4.3.2c. The conclusion made from Fig. 4.3.2 is that the dissipated energy in the gas film has completely different quality of progress (related to the design of the foil) as the rotating speed changes. Therefore, retaining the dissipated energy in the gas film at highest values requires a continuous adaptation of foil properties in regards to the rotating speed. Rotor designs and unbalance magnitudes were checked with relatively similar conclusion on the sensitivity of dissipated energy to design characteristics.

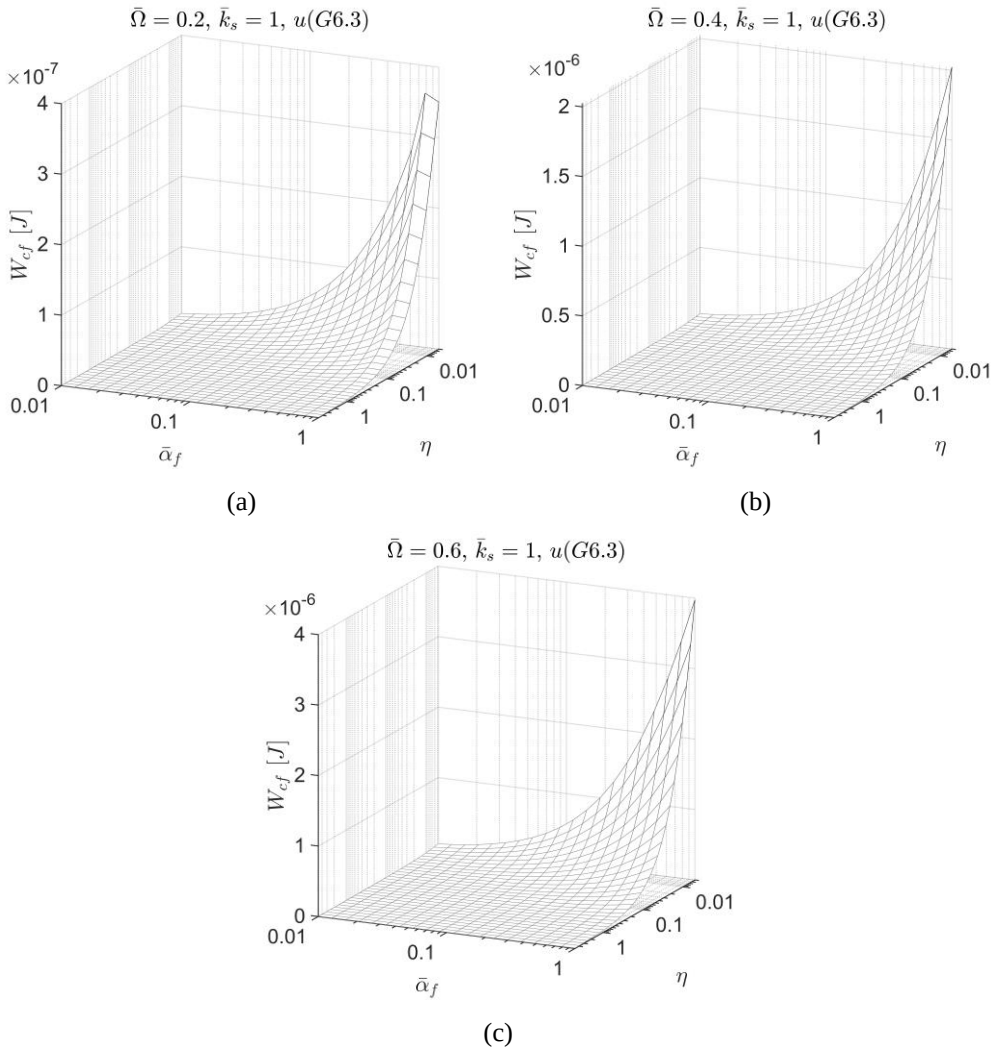

Fig. 4.3.3 Dissipated energy in the bump foil damper for various values of foil compliance $\bar{a}_f$ and foil loss factor η, at a) $\bar{\Omega} = 0.2$, b) $\bar{\Omega} = 0.4$, c) $\bar{\Omega} = 0.6$.

Specific values of bump foil properties which render the highest dissipation energy in the gas film are sought applying the optimization pattern of successive poles. The optimization scheme is implemented in various speeds. The optimization requires the minimization of an objective function OBJ, which is defined as the inverse of dissipated energy in the gas film, $OBJ = 1/W_{cb}$. Starting from random input values for foil compliance $\bar{a}_f$ and foil loss factor η, the optimization pattern renders after some iterations of successive poles the values of $\bar{a}_f$ and η that maximize W_{cb} at every speed $\bar{\Omega}$. The related progress of W_{cb} during optimization is depicted in Fig. 4.3.4 at selected speeds. The optimization pattern works in the following sequence:

a) a low rotating speed $\bar{\Omega}$ (in which local stability is guaranteed) is selected for the system and random foil properties are assigned to the model, as $\overset{0}{\bar{a}}_f$ and $\overset{0}{\eta}$; an initial limit cycle is evaluated as $\overset{0}{\tilde{\mathbf{s}}}$, and the initial dissipation energy $\overset{0}{W}_{cb}$ in the gas film is computed.
b) Successive poles are performed for the input variables as $\overset{1}{\bar{a}}_f$ and $\overset{1}{\eta}$, and the limit cycle $\overset{1}{\tilde{\mathbf{s}}}$ is computed with initial value to be $\overset{0}{\tilde{\mathbf{s}}}$; the respective dissipated work is then obtained as $\overset{1}{W}_{cb}$. This is iteration $i = 1$

c) For each pair of $\bar{a}_f^{\,i}$ and η^{i}, the limit cycle $\tilde{\bar{\mathbf{s}}}^{i}$ is computed given $\tilde{\bar{\mathbf{s}}}^{i-1}$ as initialization.

d) Steps (b) and (c) are repeated till $W_{cb}^{n} > \max\left(W_{cb}^{n-1}, W_{cb}^{n-2}, \ldots W_{cb}^{0}\right)$; $\tilde{\bar{\mathbf{s}}}^{n}$ is achieved. The procedure may require $n = 10 \sim 200$ iterations depending to the feature of *OBJ* at each speed, see Fig. 14.

e) A prediction for the limit cycle at the next speed, say $\bar{\Omega} + \Delta\bar{\Omega}$, is computed by pseudo arc length continuation, given the limit cycle $\tilde{\bar{\mathbf{s}}}^{n}$, $\bar{a}_f^{\,n}$ and η^{n}, as initialization.

f) Steps (b) to (e) are repeated till $\bar{\Omega}$ reaches a desired (high) value.

It has to be clarified that each of the Figs. 14a-c depicts the values W_{cb}^{i}, $\bar{a}_f^{\,i}$ and η^{i} at all *n* iterations, at selected speeds.

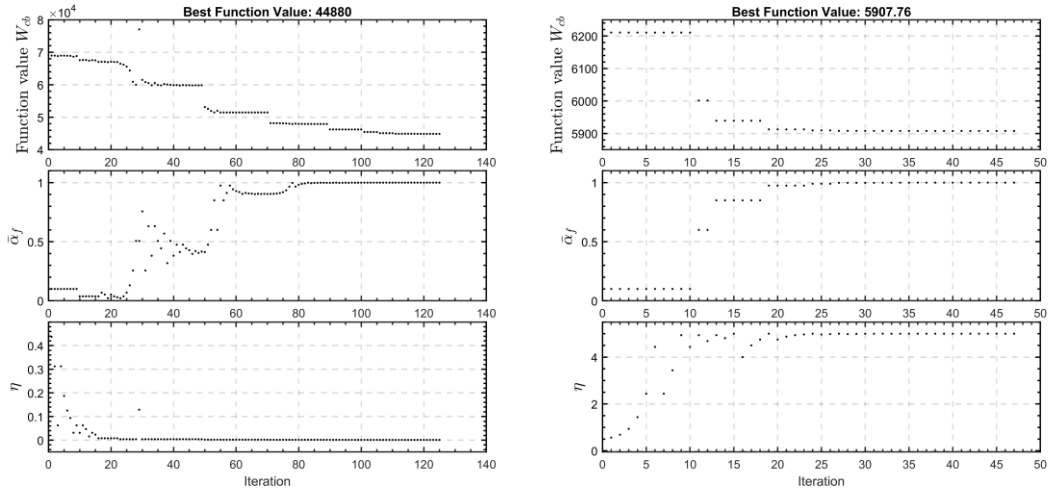

(a) (b)

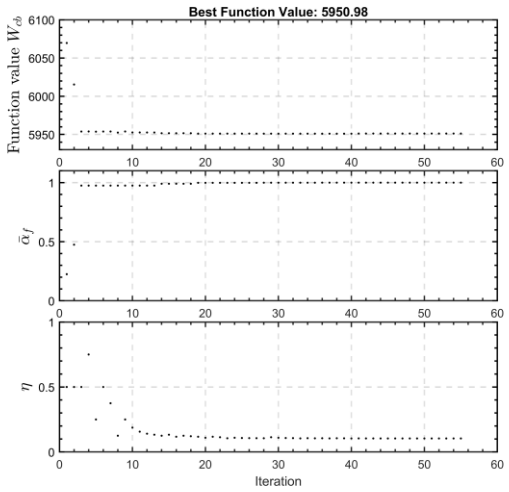

(c)

Fig. 4.3.4 Optimization of the dissipated energy in the gas film of the reference system with $\bar{k}_s = 1$ and $u(G6.3)$ with respect to the foil compliance $\bar{a}_f$ and the foil loss factor η, at a) $\bar{\Omega} = 0.2$, b) $\bar{\Omega} = 0.4$, c) $\bar{\Omega} = 0.6$

The limit cycle $\tilde{\bar{\mathbf{s}}}^{n}$ is plotted in Figs. 15 and 16 with the respective values $\bar{a}_f^{\,n}$ and η^{n} at each speed, for various design cases. Different rotor stiffness is considered in Fig. 4.3.5, and different

unbalance magnitude applies in Fig. 4.3.6; where the efficiency of the methodology to suppress bifurcations at a desired speed range is depicted. The operating speed range is limited by the limit values for the foil compliance $\bar{a}_f$ and the foil loss factor η, here defined as $0.01 \le \bar{a}_f \le 2$ and $0.0005 \le \eta \le 5$. These values may be considered differently according to the design limitations in each application of the rotating system. Considering the bifurcations sets evaluated in Section 4.2 for various designs, Fig. 4.3.5 and Fig. 4.3.6 depict elimination of bifurcations in approximately double speed range. It is also worth noticing that the bifurcation-free speed range is limited by a secondary Hopf (Neimark-Sacker) bifurcation at all cases of design.

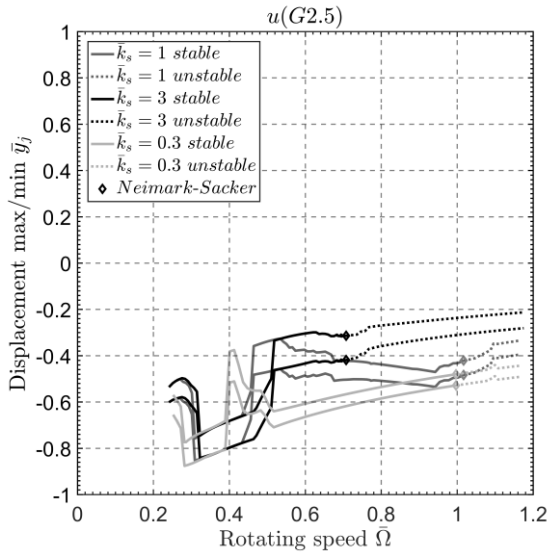

(a)

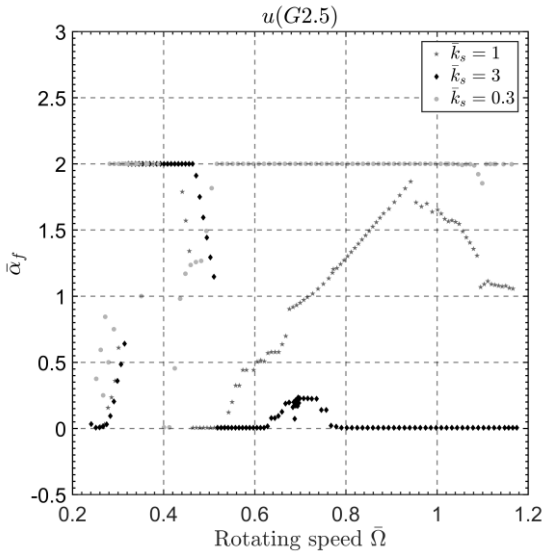

(b)

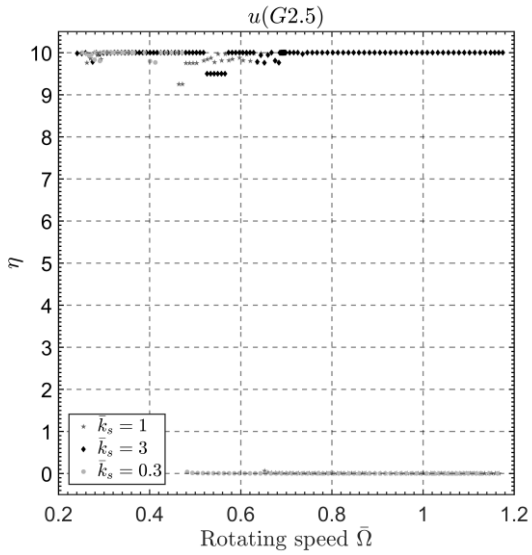

(c)

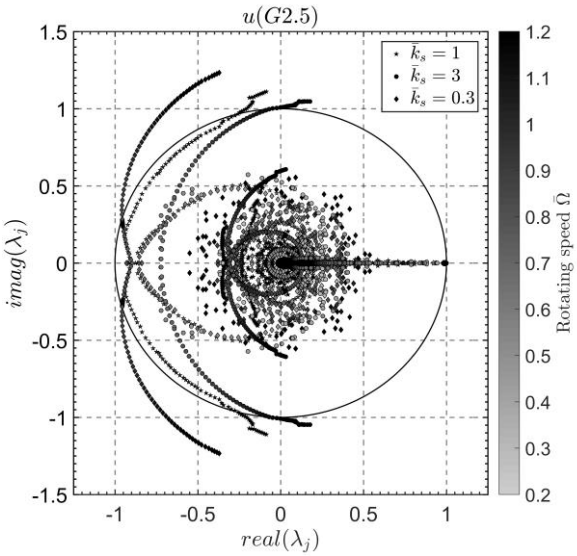

(d)

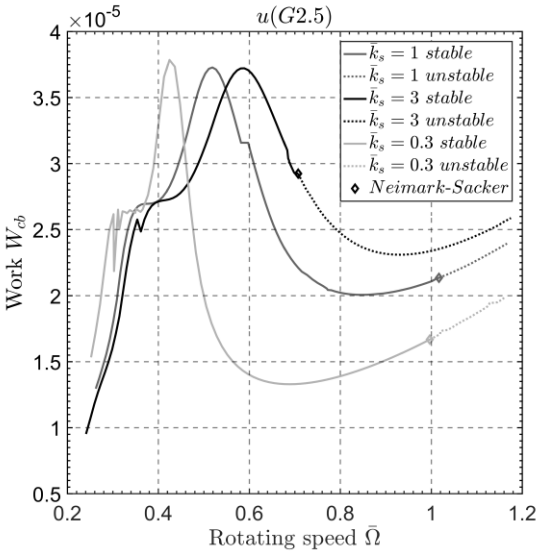

(e)

Fig. 4.3.5 Elimination of bifurcations at a speed range for the system of $u(G2.5)$ and $\bar{k}_s^- = 0.3$, $\bar{k}_s = 1$, $\bar{k}_s^+ = 3$, a) journal motion limit cycles, b) corresponding values of compliance $\bar{a}_f$ c) corresponding values for loss factor η d) Floquet multipliers of the corresponding limit cycles e) Energy flow in the gas film

In Fig. 16 one may notice the expected displacement of the limit cycles in vertical direction (see Fig. 15a) as the foil compliance receives higher and lower values (see Fig. 16b). The Floquet multipliers in Fig. 16d are retained within the unit circle as the rotating speed increases, changing the path of progress as the optimization takes place. The Floquet multipliers tend to cross the unit circle at the points $(-0.9, \pm 0.25)$ but they turn to a new direction continuing along the path of the unity circle, still inside the circle, up to the points $(-0.2, \pm 0.9)$ where the optimization cannot retain their values inside the circle anymore, as the rotating speed increases (resulting in Neimark-Sacker bifurcation).

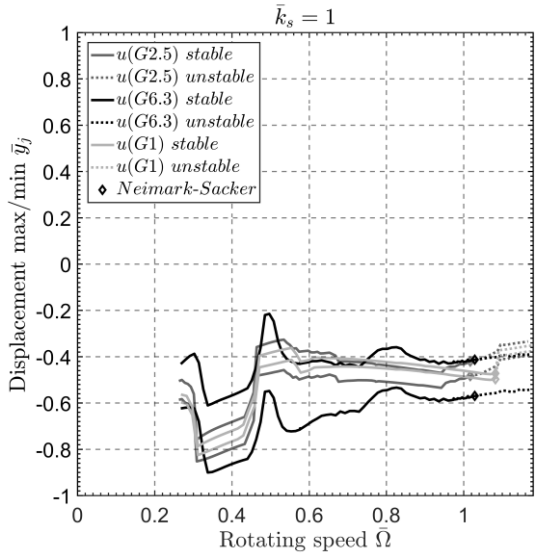

(a)

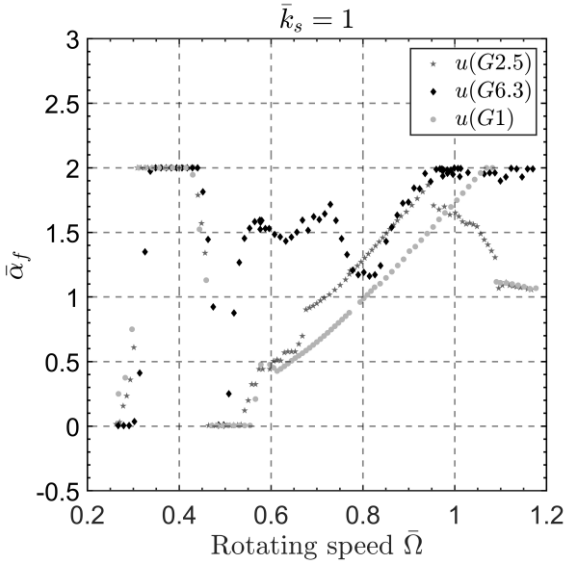

(b)

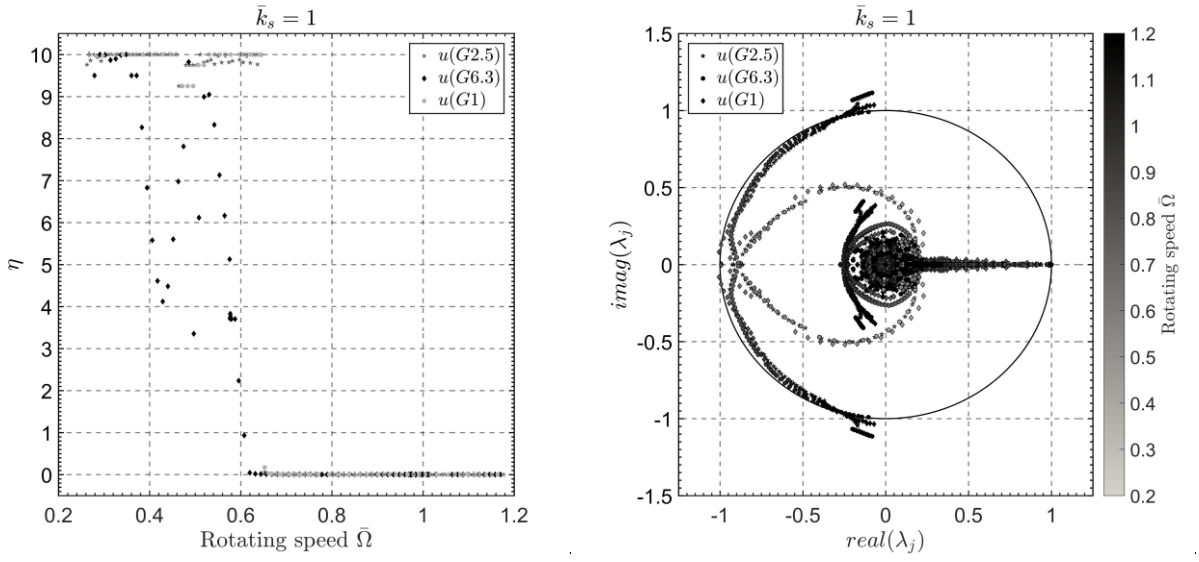

(c) (d)

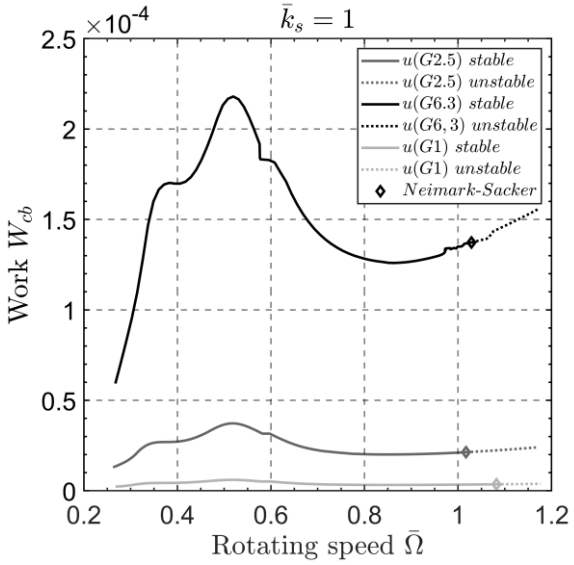

(e)

Fig. 4.3.6 Elimination of bifurcations at a speed range for the system of $\bar{k}_s = 1$ and $u(G1)$, $u(G2.5)$, $u(G6.3)$ a) journal motion limit cycles b) corresponding values for compliance $\bar{a}_f$ c) corresponding values for loss factor η, d) Floquet multipliers of the corresponding limit cycles e) Energy flow in the gas film

5. CONCLUSION

The bifurcation set of a rotating shaft on gas foil bearings is presented in this paper for various design cases of rotor stiffness and gas bearing properties, in a certain range of rotating speed which acts as the bifurcation parameter. The periodic limit cycle motions are evaluated applying a pseudo arc length continuation method with embedded orthogonal collocation. The work of the non-conservative and nonlinear damping force of the gas film is evaluated at each limit cycle motion, even when unstable, as the collocation method allows for this possibility. The dissipative work of the gas film forces is found to be affiliated to the self-exciting mechanism which triggers bifurcations of the solution branches which have been earlier defined by the unbalance force and the elastic rotor properties (stable motion). The loss of this local stability (through Neimark-Sacker bifurcation or Period Doubling bifurcation) occurs simultaneously with the reversal in the energy flow in the gas film, meaning that the dissipative work changes sign when the NS bifurcation takes place. At each limit cycle, an optimization pattern utilizing successive polls is applied to maximize the dissipated work in the gas, defining the values of bump foil stiffness and damping, to avoid bifurcation according to the previous notation. The optimization pattern reveals that bifurcations are avoided when reducing the foil stiffness, doubling (at least) the operating speed range without bifurcations to take place. The procedure is repeated for several design scenarios of rotor stiffness and unbalance magnitude, and similar efficiency is noticed regarding bifurcation elimination. Research on design solutions to implement the change of foil damping and stiffness in a real system belongs to ongoing work.

REFERENCES

[1] T. Leister, C. Baum, W. Seemann (2017) On the Importance of Frictional Energy Dissipation in the Prevention of Undesirable Self-Excited Vibrations in Gas Foil Bearing Rotor Systems. TECHNISCHE MECHANIK, 37, 2-5, (2017), 280 – 290

[2] Heshmat, H.; Walowit, J. A.; Pinkus, O. (1983) Analysis of gas-lubricated foil journal bearings. Journal of Lubrication Technology, 105, 4, 647–655.

[3] Howard, S. A.; Bruckner, R. J.; DellaCorte, C.; Radil, K. C. (2007) Gas foil bearing technology advancements for closed Brayton cycle turbines. Tech. Rep. NASA TM-214470, National Aeronautics and Space Administration, United States of America.

[4] Howard, S. A. (1999) Rotordynamics and design methods of an oil-free turbocharger. Tech. Rep. NASA CR-208689, National Aeronautics and Space Administration, United States of America.

[5] Howard, S. A.; Bruckner, R. J.; Radil, K. C. (2010) Advancements toward oil-free rotorcraft propulsion. Tech. Rep. NASA TM-216094, National Aeronautics and Space Administration, United States of America.

[6] DellaCorte C., Zaldana, A., and Radil, K. (2004) A Systems Approach to the Solid Lubrication of Foil Air Bearings for Oil-Free Turbomachinery. STLE/ASME Joint International Tribology Conference, FL Oct. 2003

[7] Gross, W. A. (1962) Gas Film Lubrication, John Wiley and Sons, Inc.

[8] H. Ming Chen, Roy Howarth, Bernard Geren, Jay C. Theilacker, William M. Soyars, (2001), "Application of foil bearings to helium turbocompressor", Proceedings of the 30th turbomachinery symposioum.

[9] Heshmat, C. A., Heshmat, H., (1995), "An Analysis of Gas-Lubricated, Multileaf Foil Journal Bearings with Backing Springs," J. Tribol., 117, pp. 437-443.

[10] Braun, M. J., Choy, F. K., Dzodzo, M., and Hsu, J., (1996), "Two-Dimensional Dynamic Simulation of a Continuous FoilBearing", Tribol. Intl., 29(1), pp. 61-68.

[11] Heshmat, H., Shapiro, W., and Gray,S, (1982), "Development of Foil Journal Bearings for High Load Capacity and High Speed Whirl Stability", ASME J. Lubr. Technol., 104, pp. 149–156.

[12] DellaCorte, C., and Wood, J. C. (1994), "High Temperature Solid Lubricant Materials for Heavy Duty and Advanced Heat Engines", NASA TM-106570.

[13] Blok H., and van Rossum J. J., (1953) "The Foil Bearing-A New Departure in Hydrodynamic Lubrication", ASLE J. Lubr. Eng., 9, pp. 316–330.

[14] Ma, J. T. S., 1965, ''An Investigation of Self-Acting Foil Bearings,''ASME J. Basic Eng., 87, pp. 837–846.

[15] Barnett, M. A., and Silver, A. (1970) ''Application of Air Bearings to High Speed Turbomachinery'', SAE Paper 700720.

[16] DellaCorte, C., and Valco, M. J. (2000) "Load Capacity Estimation of Foil Air Journal Bearings for Oil-Free Turbomachinery Applications", STLE Tribol. Trans., 43, pp. 795–801.

[17] Krzysztof Nalepa, Paweł Pietkiewicz , Grzegorz Żywica, (2009),"Development of the foil bearing Technology", Technical Siences, Abbrev.: Techn. Sc., No 12, Y 2009

[18] Christopher DellaCorte, Kevin C. Radil, Robert J. Bruckner, S. Adam Howard, (2007), "Design, Fabrication and Performance of Open Source Generation I and II Compliant Hydrodynamic Gas Foil Bearings", NASA/TM—2007-214691

[19] Y. Hou, Z. H Zhu, C. Z. Chen (2004) Comparative test on two kinds of new compliant foil bearing for small cryogenic turbo-expander. *Cryogenics*, 44: 69-72.

[20] Z. Y. Guo, K. Feng, T. Y. Liu (2018) et al. Nonlinear dynamic analysis of rigid rotor supported by gas foil bearings: effects of gas film and foil structure on subsynchronous vibration. Mechanical Systems and Signal Processing, 107: 549-566.

[21] H Heshmat H. (1991) A feasibility study on the use of foil bearings in cryogenic turbopumps. 27th AIAA/SAE/ASME/ASEE Joint Conference, California, USA, June 24-26: AIAA-91-2103.

[22] C. P. Ku, H. Heshmat (1992) Compliant foil bearing structural stiffness analysis: part1-theoretical model including strip and variable bump foil geometry, Journal of Tribology 114 (2): 394–400.

[23] Peng, J.-P.; Carpino, M. (1993) Calculation of stiffness and damping coefficients for elastically supported gas foil bearings. Journal of Tribology, 115, 1, 20–27.

[24] J. P. Peng, M. Carpino (1997) Finite element approach to the prediction of foil bearing rotor dynamic coefficients, Journal of Tribology 119 (1): 85–90.

[25] I. Iordanoff (1997) Analysis of an aerodynamic compliant foil thrust bearing: method for a rapid design. Journal of Tribology 121 (4) 1996 816-822

[26] H. Heshmat., P. Hermel, (1993), Compliant Foil Bearings Technology and Their Application to HighSpeed Turbomachinery, Journal of Tribology 25: 559-575

[27] L. San Andres, T. H. Kim (2007), Improvements to the analysis of gas foil bearings: Integration of top foil 1D and 2D structural models. In: ASME turbo expo 2007: Power for land, sea, and air, pp. 779789. New York: ASME.

[28] T. H. Kim, L. San Andres (2008), Heavily loaded gas foil bearings: a model anchored to test data, Journal Engineering for Gas Turbines and Power 130 (1) 012504–012508.

[29] L. San Andres, T. H. Kim (2008), Forced nonlinear response of gas foil bearing supported rotors, Tribol. Intern. 41 704–715.

[30] D. Kim (2007) Parametric studies on static and dynamic performance of air foil bearings with different top foil geometries and bump stiffness distributions, Journal of Tribology 129 (2) 354–364.

[31] S. Le Lez, M. Arghir, J. Frene (2007) A new bump-type foil bearing structure analytical model, Journal of Engineering for Gas Turbines and Power 129 (4) 1047–1057.

[32] S. Le Lez, M. Arghir, J. Frene (2009) Nonlinear numerical prediction of gas foil bearing stability and unbalanced response, Journal of Engineering for Gas Turbines and Power 131:012503–012512.

[33] Carpino M. and Talmage G. (2006), "Prediction of rotor dynamic coefficients in gas lubricated foil journal bearings with corrugated sub-foils", Tribol. Trans, 49: 400–409.

[34] Carpino M. and Talmage G. (2003), "A fully coupled finite element formulation for elastically supported foil journal bearings", Tribol Trans, 46: 560–565.

[35] Lee Y-B, Park D-J, Kim C-H, et al. Operating characteristics of the bump foil journal bearings with top foil bending phenomenon and correlation among bump foils. Tribol Int 2008; 41: 221–233

[36] K. Feng, S. Kaneko (2010) Analytical model of bump-type foil bearings using a link spring structure and a finite element shell model, Journal of Tribology 132 (2) 1–11.

[37] S. LeLez, M. Arghir, J. Frêne (2009) Nonlinear numerical prediction of gas foil bearing stability and unbalanced response, Journal of Engineering for Gas Turbines and Power 131:012503.

[38] D. Kim (2007) Parametric studies on static and dynamic performance of air foil bearings with different top foil geometries and bump stiffness distributions, Journal of Tribology 129: 354–364.

[39] J. Zhang, W. Kang, Y. Liu (2009) Numerical method and bifurcation analysis of Jeffcott rotor system supported in gas journal bearings, Journal of Computational and Nonlinear Dynamics 4 011007.

[40] P. Bonello, H. M. Pham (2014) The efficient computation of the nonlinear dynamic response of a foil–air bearing rotor system, Journal of Sound and Vibration 333:3459–3478.

[41] H. M. Pham, P. Bonello (2013) Efficient techniques for the computation of the nonlinear dynamics of a foil–air bearing rotor system, ASME TurboExpo2013: Turbine Technical Conference and Exposition, p.7.

[42] J. S. Larsen, I. F. Santos (2014) Efficient solution of the non-linear Reynolds equation for compressible fluid using the finite element method, Journal of the Brazilian Society of Mechanical Sciences and Engineering 1–13.

[43] Baum C., Hetzler H., Schröders S., Leister T., Seemann W. (2020) A computationally efficient nonlinear foil air bearing model for fully coupled, transient rotor dynamic investigations. Tribol. Int. doi: https://doi.org/10.1016/j.triboint.2020.106434

[44] Heshmat, H (1994).: Advancements in the performance of aerodynamic foil journal bearings: High speed and load capability. J. Tribol. 116(2), 287–294

[45] Gu, Y., Ma, Y., Ren, G.: Stability and vibration characteristics of a rotor-gas foil bearings system with high static low dynamic stiffness supports. J. Sound Vib. 397, 152–170 (2017)

[46] Hoffmann, R., Pronobis, T., Liebich, R.: Non-linear stability analysis of a modified gas foil bearing structure, In: Proceedings of the 9th IFToMM International Conference on Rotor Dynamics, Springer, pp. 1259–1276 (2015)

[47] Wang, C.-C., Chen, C.-K.: Bifurcation analysis of selfacting gas journal bearings. J. Trib. 123(4), 755–767 (2001)

[48] Zhang, J., Kang, W., Liu, Y.: Numerical method and bifurcation analysis of Jeffcott rotor system supported in gas journal bearings, J. Comput. Nonlinear Dynam. 4(1)

[49] Yang, P., Zhu, K.Q., Wang, X.L.: On the nonlinear stability of selfacting gas journal bearings. Tribol. Int. 42(1), 71–76 (2009)

[50] Seydel, R.: Practical Bifurcation and Stability Analysis, vol. 5. Springer Science & Business Media, Berlin (2009)

[51] Chasalevris, A.: Stability and Hopf bifurcations in rotor-bearing-foundation systems of turbines and generators. Tribol. Int. 145, 106154 (2020)

[52] Zhang, J., Kang, W., and Liu, Y. (2008). "Numerical Method and Bifurcation Analysis of Jeffcott Rotor System Supported in Gas Journal Bearings." ASME. *J. Comput. Nonlinear Dynam*. 4(1): 011007

[53] A. Nayfeh, B. Balachandran, (1995), "Applied nonlinear dynamics : analytical, computational, and experimental methods"

[54] Li, H., Geng, H. and Lin, H. (2021), "Thermo-elastohydrodynamic analysis of the inhomogeneous foil bearing with misalignment", Industrial Lubrication and Tribology, Vol. 73 No. 6, pp. 891-896.

[55] Bonello, P.; Pham, H. M. (2014) The efficient computation of the nonlinear dynamic response of a foil-air bearing rotor system. Journal of Sound and Vibration, 333, 15, 3459–3478.

[56] Hoffmann, R.; Pronobis, T.; Liebich, R. (2014) Non-linear stability analysis of a modified gas foil bearing structure. In: Proceedings of the 9th IFToMM International Conference on Rotor Dynamics, Milan, Italy.

[57] Baum, C.; Hetzler, H.; Seemann, W. (2015) On the stability of balanced rigid rotors in air foil bearings. In: Proceedings of the SIRM 2015, Magdeburg, Germany(2015a).

[58] Choi, D.H.; Yoon, K.C.: A design method of an automotive wheel-bearing unit with discrete design variables using genetic algorithms. J. Tribol. 123, 181–187 (2001)

[59] Chakraborty, I.; Kumar, V.; Nair, S.B.; Tiwari, R.: Rolling element bearing design through genetic algorithms. Eng. Optim. 35(6), 649–659 (2003)

[60] Rao, B.R.; Tiwari, R.: Optimum design of rolling element bearings using genetic algorithms. Mech. Mach. Theory 42, 233–250 (2007)

[61] Gupta, S.; Tiwari, R.; Nair, S.B.: Multi-objective design optimization of rolling bearings using genetic algorithm. Mech. Mach. Theory 42, 1418–1443 (2007)

[62] Ganesan, H.; Mohankumar, G.: Optimization of machining techniques in CNC turning centre using genetic algorithm. Arab. J. Sci. Eng. 38, 1529–1538 (2013)

[63] Kumar, K.S.; Tiwari, R.; Reddy, R.S.: "Development of an optimum design methodology of cylindrical roller bearings using genetic algorithms. Int. J. Comput. Methods Eng. Sci. Mech. 9(6), 321–341 (2008)

[64] Kumar, K.S.; Tiwari, R.; Prasad, P.V.V.N.: An Optimum design of crowned cylindrical roller bearings using genetic algorithms. J. Mech. Des. 131(5), 051011 (2009)

[65] Wei, Y., Chengzu, R.: Optimal design of high speed angular contact ball bearing using a multi-objective evolution algorithm. In: Paper presented at the International Conference on Computing. Control and Industrial Engineering. IEEE, Wuhan, June 5–6 (2010)

[66] Waghole, V.; Tiwari, R.: Optimization of needle roller bearing design using novel hybrid methods. Mech. Mach. Theory 72, 71–85 (2014)

[67] Tiwari, R.; Waghole, V.: Optimization of spherical roller bearing design using artificial bee colony algorithm and grid search method. Int. J. Comput. Methods Eng. Sci. Mech. 16(4), 221–233 (2015)

[68] Dandagwhal, R.D., Kalyankar, V.D. Design Optimization of Rolling Element Bearings Using Advanced Optimization Technique. *Arab J Sci Eng* 44, 7407–7422 (2019).

[69] Torczon V. (1997), "On the Convergence of Pattern Search Algorithms," SIAM Journal on Optimization Vol.7 No.1, 1–25.

[70] Lewis R.M., Torczon V. (1996), "Rank ordering and positive basis in pattern search algorithms," ICASE NASA Langley Research Center TR 96-71.

[71] Lewis R.M., Torczon V. (1999), "Pattern search algorithms for bound constrained minimization," SIAM Journal on Optimization, Vol.9, 1082-1099.

[72] Lewis R.M., Torczon V. (2000), "Pattern search methods for linearly constrained minimization," SIAM Journal on Optimization, Vol.10 No.3, 917–941.

[73] DellaCorte, C., and Valco, M. J., 2000, "Load Capacity Estimation of Foil Air Journal Bearings for Oil-Free Turbomachinery Applications," NASA/TM—2000- 209782.

[74] Heshmat, H., Walowit, J. A., and Pinkus, O., 1983, "Analysis of Gas-Lubricated Foil Journal Bearings," J. Lubr. Tech., 105, pp. 647-655

[75] San Andrés, L., 1995, "Turbulent Flow Foil Bearings for Cryogenic Applications," J. Tribol., 117, pp. 185-195

[76] H. Heshmat, J.A. Walowit, O. Pinkus (1983) Analysis of gas lubricated compliant thrust bearings, Journal of Lubrication Technology 105: 638–646.

[77] H. Heshmat, J.A. Walowit, O. Pinkus (1983) Analysis of gas-lubricated foil journal bearings, Journal of Lubrication Technology 10: 647–655.

[78] B.J. Hamrock (1994) Fundamentals of Fluid Film Lubrication, McGraw-Hill Series in Mechanical Engineering, McGraw-Hill Inc., NewYork.

[79] Bhore S.P., Darpe A.K. (2013) Nonlinear dynamics of flexible rotor supported on the gas foil journal bearings. J. of Sound and Vib. 332:5135-5150

[80] Shampine, L. F. and M. W. Reichelt, (1997), "The MATLAB ODE Suite," SIAM Journal on Scientific Computing, Vol. 18, pp. 1–22.

[81] Doedel, E.J.: Lecture Notes on Numerical Analysis of Nonlinear Equations, Department of Computer Science, Concordia University, Montreal, Canada

[82] Doedel, E.J., Keller, H.B., Kernevez, J.P. (1991): Numerical analysis and control of bifurcation problems (II): Bifurcation in infinite dimensions. International Journal of Bifurcation and Chaos **1**(3), 745-772.

[83] Ascher, U.M., Mattheij, R.M.M, Russell, R.D., (1995): Numerical Solution of Boundary Value Problems for Ordinary Differential Equations. SIAM Classics in Applied Mathematics ser. 13 1st ed..

[84] Meijer H., Dercole, F., Olderman, B., (2009): Numerical bifurcation analysis. Encyclopedia of Complexity and Systems Science, R. A. Meyers Ed., Springer New York, 6329-6352.

[85] Allgower, E. L., Georg, K., (2003): Introduction to Numerical Continuation Methods. Society for Industrial and Applied Mathematics.

[86] The MathWorks, Inc., "Choose an ODE solver", https://www.mathworks.com/help/matlab/math/choose-an-ode-solver.html

[87] The MathWorks, Inc., “Solve stiff ODEs”, https://www.mathworks.com/help/matlab/math/solve-stiff-odes.html

[88] Shampine, L. F., M. W. Reichelt, and J.A. Kierzenka, (1999), “Solving Index-1 DAEs in MATLAB and Simulink”, SIAM Review, Vol. 41, pp. 538–552.

[89] Matthew S. Lasater, Carl Tim Kelley, Andrew G. Salinger, Dwight L. Woolard, and Peiji Zhao, (2004), "Enhancement of numerical computations of the Wigner-Poisson equations for application to the simulation of THz-frequency RTD oscillators", Proc. SPIE 5584, Chemical and Biological Standoff Detection II

[90] D. A. Aruliah, L. van Veen and A. Dubitski, (2012), “A parallel adaptive method for pseudo-arclength continuation”, J. Phys.: Conf. Ser. 385 012008

[91] Gavalas I., Chasalevris A., (2022), “Nonlinear Dynamics of Turbine Generator Shaft Trains: evaluation of bifurcation sets applying numerical continuation”, ASME Journal of Engineering for Gas Turbine and Power. Accepted for publication

[92] H. Poincaré, (1899), “Les Methodes Nouvelles de la Méchanique Céleste”, Gauthier-Villars, Paris**.**

[93] P. Stumpf, Z. Sütő, I. Nagy, (2011), “Research in Nonlinear Dynamics Triggered by R&D Experiences”, Conference: AACS'11, At: Budapest, Hungary

[94] Martin W. Lo, (2002), “The InterPlanetary Superhighway and the Origins Program”, NASA, Conference: Aerospace Conference Proceedings, IEEEVolume: 7

[95] Steven W. Smith, Ph.D., (1997), “The Scientist and Engineer's Guide to Digital Signal Processing”, Chapter 12: The Fast Fourier Transform

[96] LabVIEW 2010 Advanced Signal Processing Toolkit Help, (2010), “Short-Time Fourier Transform”

[97] Jubran Akram, (2020), “Understanding Downhole Microseismic Data Analysis”, Springer

[98] The MathWorks, Inc., “How Pattern Search Polling Works”, https://www.mathworks.com/help/gads/how-pattern-search-polling-works.html

[99] Fiedler, R.: Numerical Analysis of Invariant Manifolds Characterized by Quasi-Periodic Oscillations of Nonlinear Systems. PhD Thesis, Kassel University Press, Germany (2021).

[100] Meirovitch, L.: Methods of Analytical Dynamics. McGraw Hill, NY (1970)